New constraints on the timing of partial melting and deformation along the Nyalam section (central Himalaya): implication for extrusion models.

Running title: Partial melting and deformation above the MCT.

Philippe Hervé Leloup[1], Xiaobing Liu[1,2,3], Gweltaz Mahéo[1], Jean-Louis Paquette[4], Nicolas Arnaud[5], Alexandre Aubray[1], Xiaohan Liu[2]

1: Laboratoire de Géologie de Lyon, Terre, Planètes, Environnement, CNRS UMR 5276, Université Lyon1 – ENS Lyon, Villeurbanne, France.

2: Key Laboratory of Continental Collision and Plateau Uplift, Institute of Tibetan Plateau Research, Chinese Academy of Sciences, Beijing 100085, China.

3: Research Institute of Petroleum Exploration and development, Petrochina, Beijing 100083, China.

4: Laboratoire Magmas et Volcans, CNRS UMR 6524, Clermont Université, Clermont-Ferrand, France.

5: Géosciences Montpellier, UMR CNRS 5243, Université de Montpellier, Montpellier, France.

Abstract

New structural, U-Th/Pb and Ar/Ar data along the Nyalam section constrain the timing of partial melting, crystallization and deformation in the Greater Himalayan Sequence (GHS). Prograde metamorphism was followed by onset of partial melting at ~30 Ma. In central GHS in situ melts crystallize between 24 and 18 Ma. Subsequent cooling is very fast (~200°C/Ma) and coeval with undeformed dykes emplacement that lasts until ~15 Ma. In the upper GHS fast cooling continues until ~13 Ma. Combined with published P-T and thermochronological data from the Lantang and Dudh-Kosi Valleys these data imply that a) the partial melt zone thinned through time; b) end of melting precede end of motion on the MCT and STD by 6 and 2 Ma respectively; c) the

STD possibly initiated at ~25 Ma probably re-activating a pre-existing thrust; d) the present day topography has been established since less than 6 Ma and focussed erosion on the present-day southern slope of the Himalaya was not active at the time of the GHS exhumation. These observations suggest that the MCT/STD systems are not passive structures induced by focussed erosion as proposed by some lower crustal channel flow models.

1. Introduction

Many consider the > 2500 km long Himalayan belt that contains the 164 highest peaks on Earth as an prototypical continental compressive mountain belt. Because the India / Asia continental collision began after 60 Ma, global plate-kinematic constrains are available, which together with geological and geophysical data can help to decipher the fundamental processes controlling mountain building. However, despite more than a century of research, these processes are still widely debated and various models have been proposed. The models seek to explain the main geological characteristics of the High Himalaya: a zone of high-grade metamorphic rocks dipping to the north (the Greater Himalayan Sequence [GHS]) overthrusting less metamorphosed rocks (the lesser Himalayan series [LHS]) along the Main Central Thrust (MCT), and overlain by less metamorphosed rocks (the Tethyan Sedimentary Series [TSS]) above the South Tibet detachment system (STDS) (Fig. 1c).

For one class of models, building of the Himalaya results from crustal wedging with Indian rocks being underthrust in the lower plate and deeply buried, before to be accreted to the upper plate and then overthrust and exhumed to form the GHS [e.g., Burg et al., 1984; Burchfiel and Royden, 1985; Hodges et al., 1996; Grujic et al., 1996; Grasemann et al., 1999, Mattauer, 1986]. Most of these models assume that exhumation is favoured by the low viscosity and density of partially melted rocks, and by the re-activation of pre-existing structures. Such crustal wedges can be reproduced in sandbox experiments that take into account erosion and sedimentation, but not partial melting [e.g., Malavieille, 2010].

In a second class of models based on numerical experiments, the GHS corresponds to lower crustal rocks flowing from beneath the Tibetan plateau [e.g., Beaumont et al., 2001]. Because the crust is exceptionally thick in Tibet (≥70 km, [e.g., Hirn et al., 1984; Zhang et al., 2007]) and has a high potential energy its lower part melts and move outwards in low-viscosty channel(s) [e.g., Beaumont et al., 2001]. Exhumation is then induced by focused erosion at the front of the Himalaya and accommodated by passive structures located at the top and bottom of the extruding channel.

The Himalaya were built in at least two distinct phases. In the central Himalaya (between 83°E and 92°E), the GHS ceased to be extruded southwards above the MCT and below the STDS since ~9 - 12 Ma (Upper Miocene) [e.g., Leloup et al., 2010]. Since then, the Main Boundary thrust (MBT) and the Main Frontal thrust (MFT) located south of the MCT (Fig. 1b, c) were activated. Motion on these thrusts which likely merge downward as the Main Himalayan thrust (MHT), formed an antiformal stack affecting the overlying LHS and GHS [e.g., Bollinger et al., 2004]. The absence of a flat normal fault at the top of the system during the second phase of Himalaya building is best explained by an accretionary prism model [e.g., Herman et al., 2010]. For the first phase of Himalaya building, arguments in favour of both the accretionary prism [e.g., Kohn, 2008], tectonic wedging [e.g., Webb et al, 2007] and lower channel flow [e.g., Jamieson et al, 2006] models have been presented.

In this study, we present a geological section of the full GHS from the MCT to above the STDS along the Nyalam-Kodari road (or Friendship Highway, between China and Nepal, Fig. 1d) along the Bhote Kosi river at ~86° East. We investigate the ages of the magmatic rocks crystallisation and their relationships with deformation, as well as the age of late faults and gashes. We can thus propose a likely mechanism for the GHS emplacement during the first phase of the Himalaya building.

2. Geological Setting

2.1 Large-scale structure of the Greater Himalayan Sequence

In the central Himalayas, the main litho-tectonic units define strips, nearly parallel to the range, dipping to the north and separated by major tectonic contacts. The central unit, the GHS, is a sliver of gneiss, micaschist, calc-silicates and granites sandwiched between less metamorphosed rocks (Fig. 1b, c). At its base (south) the GHS rests on the phyllites and quartzites of the LHS. To the top (north) the GHS is separated from the weakly metamorphosed TSS by the South Tibetan detachment (STD).

In some area, two distinct units have been distinguished within the GHS: the Lower and Upper Greater Himalayan Sequence (LoGHS and UGHS) [e.g., Kali et al., 2010; Mukherjee & Koyi, 2010a; Mukherjee, 2013a]. The LoGHS is mostly composed of strongly deformed rocks showing top-to-the-south thrusting, whose basal contact is the lower Main Central Thrust (MCTl or MCT-1) (Fig. 1a, b). The UGHS mostly consists of paragneiss, often migmatitic, intruded by Miocene leucogranites [e.g., Borghi et al., 2003]. Locally, the base of the UGHS has been shown to be a thrust zone, as the High Himal Thrust [Goscombe et al., 2006] that is laterally equivalent to the upper MCT (MCTu or MCT-2, Fig. 1a, b). Other discontinuities such as the Mangri and Toijem thrust zones in Dolpo [Montomoli et al., 2013; Carosi et al., 2010] have been described in the UGHS.

The STDS corresponds to a series of north dipping structures accommodating top-to-the-north/normal motion of the Tethyan sedimentary series (TSS) of South Tibet with respect to the GHS (Fig. 1c) [e.g., Burg, 1983; Burg et al., 1984; Burchfiel et al., 1992]. Normal motion occurred on several parallel low dipping structures that from top to bottom are: a) few brittle normal faults in the TSS, b) a detachment at the contact between the slightly metamorphosed TSS and the underlying metamorphic rocks that will be referred here as the STD and c) a ductile shear zone at the top of the GHS, the STD shear zone (STDsz), where gneisses are highly deformed, lineations trend NE and numerous shear criteria indicate a normal motion [e.g., Burg et al., 1984; Burchfiel et al., 1992; Edwards et al., 1996; Searle et al., 1997; Carosi et al., 1998; Mukherjee & Koyi, 2010b; Mukherjee, 2013b]. The TSS spans in age from Ordovician to Eocene and are not metamorphosed, unless for a narrow zone of greenschist metamorphism immediately above the STD and contact aureoles around the North Himalayan (or South Tibetan) Cenozoic plutons, outcropping as a discontinuous belt ~70 km north of the STD (Fig. 1b). Studies of the STDS along several sections, spanning from Zanskar (~76°E) to the Gonto La (~90°E) show that the UGHS is intruded by numerous large leucogranites plutons and sills, which never crosscut the STD except in the Bura-Buri pluton in north-western Nepal [29° 24'N, 82° 30'E; Carosi et al., 2013]. In this later, undeformed dyke and granite gave crystallisation age between 22.8 and 24.8Ma (monazite U/Pb data). Geochronological data show that most of the GHS leucogranites were produced during 24–14 Ma interval [e.g., Harrison et al., 1999; Leech, 2008]. These granites have been interpreted to trigger STDS motion [e.g., Burchfiel et al., 1992], or as a consequence of decompression induced by the STDS motion [e.g., Harris et al., 2004]. In many cases, the ages of the leucogranites have been taken as reflecting motion along the STDS. The presence of top-to-the-south structures at the base of the TSS or within the STD shear zone [e.g., Vannay and Hodges, 1996; Coleman and Hodges, 1998; Godin et al., 2001; Vannay et al., 2004] as been interpreted as the evidence for top-to-the-south thrusting on the STDS prior to the onset of top-to-the-north normal faulting (ibid), or to multiple alternation in shear sense along the STD [e.g., Webb et al., 2007].

2.2 Nyalam cross section of the Himalaya.

The ~N-S Bhote Kosi valley that goes through Nyalam town (~N 86°E) offers a complete section of the GHS from below the MCT to above the STDS with nearly continuous outcrops (Fig. 2). Along that section, Brun et al. [1985]

described the GHS section with, from bottom to top: paragneiss, para and ortho anatexites, augen gneiss and finally metapelites and marbles intruded by lenticular leucogranite plutons. By analogy with other sections of the GHS, the bottom paragneiss and anatexites could possibly be attributed to the LGHS, underthrust below the augen gneiss and metapelites that would correspond to the UGHS (Fig. 1d).

The structural study of Brun et al. [1985] emphasised several south verging thrusts within the LGHS marked by mylonitic zones with ~NNE-SSW lineations. They noted a striking feature of the lineation trajectories: continuous clockwise rotation from N20-30° to E-W when approaching the overlying mylonites, that they interpreted to be due to a top-to-the-west wrenching component contemporaneous with thrusting to the South. Xu et al., [2013] report that the lineations trend ~N110° E along the whole section. However, Wang et al. [2013] report lineations striking N-S to NE-SW in the lower part of the GHS and few lineations in the central GHS. In the upper part of the section, the STD -locally called the Nyalam Detachment (ND) separates the metapelites and leucogranites of the UGHS from slightly metamorphosed Tethyan sediments. The metasediments and leucogranites of the UGHS are strongly foliated, and exhibit a strong NE-SW stretching lineation in the ~300 m thick STD shear zone (STDsz) [Liu et al., 2012; Wang et al., 2013], with top-to-the-NE shear criteria [Burchfiel et al., 1992; Wang et al., 2006; Liu et al., 2012; Wang et al., 2013]. SE of Ruji, foliation in the STDsz trends ~N70, dips ~30° to the N, and lineation strikes ~N35 [Burchfiel et al., 1992; Liu et al., 2012] (Fig. 2a). Above the STD, E-W trending folds affect the TSS, some with a south vergence suggesting that they could be related with top-to-the-south thrusting prior to normal motion on faults sub-parallel to the STD. Several ~N-S east dipping normal faults affect the STD (Fig. 2a) [Burchfiel et al, 1992].

The main paragenesis found in the GHS pelitic shists are Grt+Bt+Sil+Kfs and Grt+Bt+Sil/Ky+Ms suggesting a pre- to syn- deformation upper amphibolite metamorphic facies [Hodges et al., 1993; Wang et al. ,2013]. In more details, Wang et al. [2013] distinguish six metamorphic zones from south (bottom) to north (top): kyanite (Ky), sillimanite + muscovite (Sil-Ms), sillimanite + K-feldspar (Sil-Kf), cordierite, transitional a greenshist subzone at the very top of the GHS, and chlorite just above the STD (Fig. 1d). Applying cationic exchange thermobarometry between garnet rim and surrounding minerals as well as the Gibbs method to garnet composition led Hodges et al., [1993] to propose P-T estimates for 8 samples along the section (ellipses and black arrows in Fig. 3). From THERMOCAL calculations based on garnet and matrix biotite compositions Wang et al. [2013] propose P-T estimates for 13 samples (squares in Fig. 3). In units 3 and 4 P-T these estimates mostly correspond to higher pressures and temperatures than those of Hodges et al., [1993] based on garnet rims. Wang et al. [2013] interpret their estimates as reflecting peak P-T conditions and the pressure difference between sample N-18 on one hand and samples N-26 and N-27 on the other hand (unit 3, Fig. 3c) as due to a post metamorphic structure: the Nyalam thrust (Fig. 2a). Alternatively the samples could have recorded various stages of a continuous P-T path consistent with the garnet composition evolution as proposed by Hodges et al. [1993] (Fig. 3c). In the MCT zone the two studies yield comparable estimates but for two samples (NL-01 and N-31 of Wang et al. [2013]) that show pressures up to ~1250 MPa (~45 km depth) (dashed squares on Fig. 3d). These two samples are located south of the Hodges et al. [1993] samples. Their P-T estimates could either reflect an evolution starting at high pressures for unit 1 (I on Fig. 3d) or,the existence of two distinct units, the lower one coming from deeper than the upper one.

Several generations of leucogranites (Qtz+Kf+Pl+Ms±Bi±Tur) have intruded the GHS with some deformed and other crosscutting the deformation. The late ones are more numerous in the upper part of the section and sometime contain cordierite and/or garnet [Hodges et al., 1993]. One "migmatite granite" from the upper part of the section emplaced at ~16.8 ± 0.6 Ma (XGS121, U/Pb monazite) possibly corresponding to melting around 5-6 kbar and 650°C [Schärer et al., 1986]. Such melting probably occurred by destabilization of muscovite during the decompression linked with STDS deformation [Harris and Massey, 1994]. A late, crosscuting leucogranitic dyke from the upper GHS yields an U/Pb age of 14.1±0.7 Ma (TYC64 zircon), while zircons from a sillimanite bearing migmatitic gneiss in the central part of the section yield ages spanning from ~39.7 to 34 Ma (NY11-1) [Wang et al., 2013], but these two ages have to be considered with caution and will be discussed later (section 7.1).

Later thermal evolution stages have been constrained by Ar/Ar and Fission track (FT) thermochronology (Fig. 1e). Eight biotites Ar/Ar ages from the GHS range between ~14.3 and ~16.1 Ma, and 8 muscovite ages span from ~14.0 to 16.1 Ma suggesting that the whole section was below ~300°C at ~14 Ma [Wang et al., 2006] (NL samples, Fig. 1e). However, [Maluski et al., 1988] report Ar/Ar mica ages down to 4.5 Ma in the southern half of the section (Ti samples, Fig. 1e). Ar/Ar spectra of two K-feldspars (Kf) from mylonites of the STDsz suggest fast cooling at ~15 Ma [Wang et al., 2006]. Apatite fission track (AFT) ages of 9.7 ± 0.7 and 11.7 ± 1.3 Ma in the same samples suggest that the cooling significantly decelerated below ~150°C [Wang et al., 2006, Wang, et al., 2001]. Below the STDsz, ZFT ages north of Nyalam suggest cooling to ~250°C contemporaneous with that in the STDsz but cooling to ~100°C (AFT) delayed until ~4 Ma (Fig. 1e). South of Nyalam the cooling to ~250°C is much younger (~4 Ma) (Fig. 1e) with exhumation rate of ~0.38 mm/yr between 6 and 2 Ma [Wang et al., 2010].

3. Methods

In order to constrain the timing of the main magmatic phases within the GHS and their relationship with the deformation phases we have combined structural geology, U-Th/Pb and Ar/Ar geochronology and geochemistry.

3.1 Structural geology

Detailed structural observations were performed at 45 locations along the cross-section. A special attention was paid to the presence, or not, of stretching lineation and shear criteria, and between the relationships between intrusion and deformation. Foliation and lineation measurements are summarized in stereonet diagrams shown in Figures 2b to 2f, while several relationships between intrusion and deformation are illustrated in Fig. 4.

Several quartz ribbons where taken from below the STD to investigate the quartz crystal crystallographic preferred orientation (CPO). Quartz CPO describes the orientation of the <c>-axis of the quartz grains within the ribbon. The CPO indicates the active glide system(s) during deformation and has long been used to infer the type and the temperature of deformation. This method has already been used to describe the deformation within the STDsz and in the GHS [Law et al., 2004, 2011]. For deformation close to simple shear the activation of the basal plane along the <a> direction, leading to the <c> axis concentrated near the maximum shortening axis (Z axis), is supposed to occur at low temperatures: < 400°C [Gapais and Barbarin, 1986; Stipp et al., 2002; Passchier and Trouw, 2005]. At higher temperatures, the subordinate activation of the rhomb-<a> (or rhomb-<a+c>) slip system develops a girdle in the CPO plots [Menegon et al., 2008; Peternell et al., 2010]. According to Stipp et al. [2002], the transition from combined basal, rhomb, and prism <a> slip to dominantly prism <a> slip (and therefore from a YZ girdle to a dominant single Y maximum in the <c>-axis pole figures) is rather abrupt and occurs at ~ 500°C. The temperature range of dominantly prism-<a> slip is between 500°C and ~600 -650°C. This former temperature is that of the onset of dominant prism-<c> slip [Mainprice et al., 1986].

Quartz CPOs where obtain by the Automatic Ice Texture Analyzer (AITA-G50) [Russell-Head and Wilson, 2001] at Laboratoire de Glaciologie et de Géophysique de l'Environement (Grenoble, France). This analyser is an optical device that detects the orientation of the optical axis for ice and quartz. It is an alternative to Electron Back Scattered Diffraction (EBSD) but allows only <c>-axis orientation measurements. The method described by Peternell et al.

[2010], is based on a stack of eight microphotographs taken with different orientations with respect to the cross-polarized light. The spatial step is 6.8 μm for all samples. The data (colatitudes, azimuth and quality factor) are extracted and are analyzed using the package G50 Investigator (http://www.earthsci.unimelb.edu.au /facilities /analyser /downloads.html). The plots are performed using Stereo32 (http://www.heise.de /download /stereo32-1160507.html) and the stereoplots are drawn for one point per pixel. For each sample, thin section pictures with location of the zones investigated, together with <c> axis orientation maps and one point per pixel stereographic projection are shown in appendixes A33 to A35.

3.2 U-Th/Pb geochronology

3.2.1 Mineral separation and analysis

Monazites and / or zircons were extracted from 19 granite and migmatite samples. Zircon and monazite mineral separation was performed at the Yumeng mineral separation service lab in Langfang (Hebei province, China). Grains larger than 75 μm were mounted in epoxy resin, then abraded to reveal their center part and polished down to 1/4 mm with diamond paste. The mounts were coated with carbon prior to Backscattered Electrons (BSE) and Cathodo-luminescence (CL) analysis performed at the Laboratoire magmas et volcans (Clermont-Ferrand, France). U-Th/Pb isotopic data for the monazites and zircon were obtained by laser ablation inductively coupled plasma spectrometry (LA-ICPMS) in the same laboratory. Analytical techniques and procedures resemble the ones ~~the ones~~ described in recently published articles [Boutonnet et al., 2012; Leloup et al., 2010; Liu et al., 2012]. Detailed analytical techniques are also reported in Paquette and Tiepolo [2007].

3.2.2 Data analysis

For zircons, the analytical results were projected both on $^{206}Pb/^{238}U$ versus $^{237}Pb/^{235}U$ (concordia) diagrams and $^{207}Pb/^{206}Pb$ versus $^{238}U/^{206}Pb$ diagrams [Tera and Wasserburg, 1972]. For monazites, the analytical results are plotted in $^{206}Pb/^{238}U$ versus $^{208}Pb/^{232}Th$ Concordia diagrams. The error ellipses sometimes display a sub-vertical and reversely discordant linear array in these diagrams. In recent mineral, this is generally related to excess ^{206}Pb produced by excess ^{230}Th, resulting from radioactive disequilibria in the decay chain of ^{238}U [Parrish, 1990; Schärer, 1984]. $^{208}Pb/^{232}Th$ dating of young monazites using *in situ* techniques is a well-established geochronological method [Harrison et al., 1995, Stern and Sanborn, 1998] based on the high Th content in monazite crystals, producing a significant amount of the daughter isotope ^{208}Pb in a very short time. Another advantage is the lack of long-lived intermediate daughter in the ^{232}Th-^{208}Pb decay chain [Getty and De Paolo, 1995].

When MSWD>2, concordia ages cannot be calculated and mean $^{206}Pb/^{238}U$ age for zircon and $^{208}Pb/^{232}Th$ age for monazite are reported. Such age scatter may represent the mixing of different ages domains or the complex interactions with fluids. Moreover, the very high U content recorded in most zircon strongly favour the instability of their crystal lattice associated to the disturbance of their U-Pb system. Consequently, these peculiar geochronological results will be considered and discussed with caution, considering a larger uncertainty than the nominal one or a range of ages.

3.2.3 Zircon and monazite systematics

Once age populations are characterized, the key issue is to determine their geological signification. In most cases, the U-Th/Pb system is a geochronometer which meaning that, contrary to thermochronometers, its closure temperature is higher than the temperature of melt crystallization. Consequently, most U-Th/Pb ages of monazite and zircon are attributed to the timing of crystallization from the melt. Nevertheless, it is classical to find single zircons and monazites having preserved several age populations with inherited ages in the core and the youngest age in the rim.

Along a clockwise P-T path similar to that followed by GHS units (Fig.

3) zircons mostly form or overgrow at the onset of partial melting and in the melt at peak temperature and during subsequent cooling and final crystallization [Schiotte et al., 1989; Roberts and Finger, 1997; Schaltegger et al., 1999; Vavra et al., 1999; Rubatto et al., 2001; Kelsey et al., 2008; Hermann and Rubatto, 2003; Imayama et al., 2012]. Low Th/U ratios (≤0.05) of rims that suggest strong Th depletion relatively to U could be related to the (re-)crystallization during later metamorphism or metasomatism [Rubatto et al., 2001], but may also result from melting of a Th-depleted magma source.

Many recent studies demonstrated that Pb diffusion in monazite is very slow and does not affect the U-Th/Pb chronometer even at high temperatures (i.e. Cherniak et al., 2004; Gardès et al., 2006; MacFarlane and Harrison, 2006), making possible the preservation of inherited ages even in molten rocks. However, diffusion-precipitation in the presence of fluids may disturbs or resets the monazite chronometer at lower temperature [Teufel and Heinrich, 1997; Seydoux-Guillaume et al., 2002; Harlov and Hetherington, 2010; Hetherington et al., 2010; Harlov et al., 2011; Williams et al., 2011; Budzyn et al., 2011; Bosse et al., 2009; Didier et al., 2013]. In a geochronological study of monazites of the Lantang valley Kohn et al. [2005] stressed two main stages of monazites formation along the clockwise P-T path followed by the GHS rocks. First prograde monazite grows in subsolidus conditions. These monazites should be dissolved when the rock melts [Spear and Pyle, 2002], but shielding in other minerals (i.e., garnet, biotite) can protect some crystals from dissolution. In any case, a second generation of magmatic monazite may crystallize during cooling close to the solidus temperature. The ages of these two monazite generations bracket the timing of melting [Kohn et al., 2005].

3.3 Argon geochronology

Analyses were performed on the 150–250 μm-size fraction after separation with a Frantz magnetic separator, heavy liquids and finally by hand picking under a binocular microscope, carried out at the LGL-TPE (Lyon, France). We have analyzed 8 fractions of 6 samples in order to further constrain the cooling history of the GHS and the age of late structures along the Nyalam section (Table 1). Ar–Ar ages were obtained at the geochronology laboratory of Geosciences Montpellier (University Montpellier 2, France). Irradiation factor J was determined using duplicates analysis of TCR2 sanidine standard with an age of 28.340 ± 0.099 Ma [Renne et al., 1998]. Analytical details are given in Appendix A31. Ar/Ar data are summarized in Table 3 and detailed in Tables A23 to A30.

All ages are quoted at 2σ. Age plateau given are weighted mean plateaus [Fleck et al., 1977] which error takes into account that on the J factor. The isochron ages are obtained in an inverse isochron diagram of $^{36}Ar/^{40}Ar$ versus $^{39}Ar/^{40}Ar$ [Roddick et al., 1980]. Errors on age and intercept age include individual errors on each point and linear regression by York's method [York, 1969]. The goodness of fit relative to individual errors is measured by the Mean Square Weighted Deviation (MSWD). Once the age of a given mineral is calculated, a fundamental and controversial issue is to determine whether this age corresponds to mineral crystallization, recrystallization, or cooling below a given closure temperature. In order to carry such discussion the closure temperatures are assumed to be 510±50°C for the amphiboles [Harrison, 1982], 390±45°C for the white micas [Hames and Bowring, 1994, Harrison et al., 2009], and 320±40°C for biotites [Harrison et al., 1985].

3.4 Geochemistry

Whole-rock major and some trace elements (Ba, Rb, Sr, Zr, Nb, Y, Pb, V, Ni, Co and Sc) of four tourmaline leucogranites (T11N25, 29, 30, 56), five leucopegmatites (T11N10, 37, 41, 44, 47), five two micas leucogranites (T11N11, 33, 34, 39, 42), three biotite granites (T11N32, 38, 45) and one migmatite (T11N09) were determined by wavelength-dispersive X-ray fluorescence spectrometry (XRF) at the University of Lyon (Table A19). Analytical uncertainties range from 1 to 2% for major elements and from 10 to 15% for trace elements.

4. *Structural and petrographic observations.*

4.1 Main units

Our new field observations are broadly consistent but show several significant variations from the published ones. We distinguish six tectono-stratigraphic units that are from bottom to top: the lesser Himalaya (LH), the MCT zone (unit 1), the migmatitic orthogneiss (unit 2), Ortho and paragneiss (unit 3), the STD zone (unit 4) and the Tethyan sedimentary series.

4.1.1 Main central thrust (MCT) zone (unit 1).

Garnet micaschists and paragneiss from the High Himalayan crystalline outcrop above the weakly metamorphosed Himalayan phyllites of the lesser Himalaya . These rocks show a foliation that constantly trends close to E-W (N100 on average) and dips 20 degree to 55 degree to the North (30 degree on average) (Figs. 1d, 2a,c). In some outcrops, a stretching lineation is present and trends NE-SW to NW-SE (Fig. 2b). Up section, the paragneiss shows more and more evidences for partial melting with the proportion of leucosome increasing. The gneiss shows isoclinal folds suggesting strong deformation. From the LH the grade of metamorphism increases upwards which has led to the description of the Himalayan “inverted metamorphism” and to the interpretation of the High Himalayan crystalline being thrust on top of the lesser Himalaya [e.g., Frank et al., 1973].

4.1.2 Migmatitic orthogneiss (unit 2).

Above the first occurrence of diatexite migmatites (site T162, Fig. 1d) are mostly found orthogneiss, often migmatitic, with foliations dipping steeply to the NNW (50° to 75°, 58° on average) (Fig. 2a, c) that we ascribe to unit 2. These rocks show no stretching lineation. Locally the foliation dips to the SSE (site T168, Fig. 4b). The orthogneiss are crosscut by steep ~N-S leucocratic dykes containing tourmaline (Fig. 2c, Fig. 4a).

4.1.3 Interbedded migmatitic orthogneiss and marbles (unit 3).

North and west of Nyalam outcrop interbedded paragneiss, marbles, thinly laminated migmatites, and orthogneiss with pluri-centimetric feldspar porphyroclasts that show variable foliation dips. This zone has been depicted as an antiform by some authors [e.g., Wang et al., 2006] but the foliation geometry is quite complex (Fig. 1d, Fig. 2a, d). The rocks do not show clear stretching lineation, and are crosscut by undeformed granites and pegmatite as well as leucocratic dykes containing tourmaline trending NNE-SSW and dipping to the ENE (Fig. 2d). At site T181, pegmatitic sills are locally sub-concordant with the foliation that dip ~30° to the SE, but cut the isoclinal folds that affect that foliation (Fig. 4c). This suggests at least two melting events: the first one before or during the folding of the migmatitic foliation and the second one after that folding. At site T182, the orthogneiss are cut by a N10 40 W trending dyke bearing white micas and tourmaline (Fig. 4d). At site T183 marble layers are crosscut by a pegmatite showing pluricentimetric biotites (Fig. 4e).

4.1.4 Paragneiss and marbles with minor evidence for in situ partial melting (Unit 4)

4.1.4.1. General structure

Within unit 4 outcrop paragneiss and marbles intruded by tourmaline-bearing and two micas granites (Fig. 1d). Unit 4 corresponds to the cordierite and transitional zones of Wang et al. [2013] where they report generalized migmatisation. However our field observations suggest that in situ partial melting is limited. East of Ruji, the foliation in the paragneiss and marbles trends monoclinally N45 50NW (Fig. 2e), while it is flatter near Ruji: N70 30N (Fig. 2f). The granites are often intensively deformed appearing as boudinated sills (Fig. 4g, h, i, j), but are sometimes completely undeformed or only affected by few shear zones. Besides these shear zones, stretching lineations are only visible in the ~300m thick upper part of the unit, just below the STD.

Near ZhasongLe, the lineation trends ~N 50 (pitch of ~00° to 10°S), while it trends ~N10 in the shear zones lower within unit 4 (Fig. 2e). Near Ruji, the lineation within the STDsz strikes ~N35 (Fig. 2f). In the STDsz all shear criteria indicate a top-to-the-north motion [Burchfield et al.; 1992; Wang et al., 2006; Liu et al., 2012], corresponding to normal faulting near Ruji and right-lateral shear near ZhasongLe. That strike-slip motion can be interpreted either as a local ramp along the STD or as a late tilting because of the NNW-SSE brittle faults that affect the area and offset the STD and the STDsz (see below). In any case, the strong dip gives the opportunity to observe an exceptionally thick (~3.5 km) continuous section of the GHS below the STD. Immediately below the ND, marked by a level of brecciated limestone, is a series of orange-weathering, highly ductily sheared dolostone that probably corresponds to the Yellow Band Formation of Middle Cambrian age found below the Chomolungma summit [Myrow et al., 2009]. The dolostone rest above green quartzite and dark psamitic schists all strongly deformed. Leucocratic dykes, strongly flattened parallel to the main schistosity, intrude the basal schists. They constitute the upper part of the injection complex that affect the whole underlying GHS series mostly composed of paragneiss interbedded with some marble levels.

4.1.4.2. Deformation in the upper unit 4

The analysis of quartz CPO in four samples of the ZhasongLe section allows discussing in more details the deformation characteristics of the upper part of unit 4. At site T204 ~150m structurally below the STD (Fig. 1d), sample T11N27 is a mylonite that shows thin quartz ribbons parallel to the foliation (Fig. A34). The ribbons show intense GBM recrystalisation and a CPO with a maximum on the Y axis and an oblique girdle (Fig. 5a, Fig. A34). We interpret this as indicative of activation of the <a> prismatic and minor <a> basal glide systems during top-to-the-NE (dextral) simple shear at ~500°C. This shear sense is compatible with all shear criteria seen in the outcrop.

In the same outcrop sample T11N26 contains a large quartz ribbon slightly oblique to the main foliation that has been affected by the top-to-the-NE shear (Fig. A34). The CPO of that sample shows a maximum close to Z and two other maxima close to Y (Fig. 5b). Such maxima could be interpreted as indicative of activation of the <a> basal and <a> prismatic glide systems during sinistral shear at ~500°C This could relate to a first episode of sinistral shear prior to the main phase of dextral shear.

At site T206, ~750m structurally below the STD (Fig. 1d), T11N31 is a quartz ribbon within the shear zone affecting the tourmaline leucogranite. The thin section reveals quartz BLG structures with CPO's diagnostic of activation of the <a> prismatic glide system (Fig. 5c, d; Fig. A34). Crossed girdles suggest that the <a> basal glide was also activated with an important pure shear component under temperature of 400° to 500°C. The predominance of one of the two girdles suggests a component of top-to-the-NE (dextral) shear, compatible with shear planes seen in the thin section.

At site T213, ~2700m structurally below the STD (Fig. 1d), T11N53A is a quartz ribbon parallel to the foliation in a garnet gneiss. The CPO suggest activation of the <a> prismatic glide system, possibly under pure shear, at temperatures around 500°C (Fig. 5e; Fig. A35).

At site T209, ~3500m structurally below the STD (Fig. 2a), T11N40 is a quartz ribbon within the paragneiss (Fig. 2a; Fig. 4j). Two quartz CPO suggests activation of the <a> prismatic glide system (Fig. 5f, g; Fig. A36). However a second maxima suggests the activation of the <c> prismatic glide with a component of top-to-the-south (sinistral) shear at ~650°C.

4.1 Brittle structures

The main ductile structures that characterize the GHS are cut by few brittle structures. The largest ones are ~NNW-SSE faults that offset the STD (Fig. 2a). Near Ruji fault planes along one of these faults trend N130 to N150 and dip steeply to the east or are vertical. The striations show pitches of ~60 SE. In South

Tibet active ~N-S normal faults have a clear signature in the morphology [Armijo et al., 1986]. This is not the case of these faults that do not bound any Quaternary basins nor show typical triangular facets. In unit 3 most brittle faults are sub parallel to the main brittle faults affecting the STD.

In units 1 and 2 steep quartz gashes trending N160 to N010 (sites T158, T162, T167; Fig. 2b, c) are observed. These gashes opened in a stress regime with $\sigma 3$ ~horizontal and trending N70 to N100. At sites T158 and T160 dextral / reverse brittle faults are compatible together with the gashes with a $\sigma 1$ ~horizontal and trending ~N-S.

4.2 Granites and migmatite petrology and chemistry and relationships with deformation.

Migmatites with numerous melt layers along the foliation (e.g. T11N09, Fig. 4a) outcrop at the top of unit 1 (MCT zone) and in unit 2 . Such migmatisation is probably syntectonic with southward thrusting in the MCT zone. Migmatites in unit 3 mostly occur as partially melted levels (leucosomes) within orthogneiss (Fig. 4d). Granites in units 2, 3 and 4 occur as sills, dykes or small plutons either deformed or crosscutting the ductile structures (Fig. 1d, Fig. 4b, c, e, f, g, i). These granites never cut the STD. We did not observed *in situ* migmatisation as reported by Wang et al. [2013]. However, PT estimates suggest that some limited partial melting may have occurred in this unit (Fig. 3b). Based on mineralogy and texture, four main granites types have been recognized (Table 1). (1) leucocratic pegmatites (leucopegmatite) with rare micas, mostly biotite sometime muscovite. Garnet, sillimanite or cordierite are observed in some samples. These melts occurs as sills concordant or sub-concordant with the foliation and deformed (T11N10, Fig. 4b; T11N41, Fig. 4c; T11N37, Fig. 4j), undeformed in the orthogneiss (T11N44, Fig. 4d) or crosscutting marbles (T11N47, Fig. 4e). (2) Biotite granite, observed as dykes crosscutting the foliation (T11N45, Fig. 4d; T11N38, Fig. 4j), or deformed sills (T11N32, Fig. 4h). Kyanite partially retrogressed in sillimanite has been observed in one sample. Many samples present small muscovite inclusions in K-feldspar. (3) Two micas leucogranites, observed as crosscutting dykes (T11N11, Fig. 4b; T11N42, Fig. 4c; T11N33, Fig. 4h; T11N34, Fig. 4g) or larger undeformed bodies (T11N39). Sillimanite and rare tourmaline are present in several samples. (4) Tourmaline leucogranites observed as cross-cutting dykes (T11N08, Fig. 4a), large bodies locally affected by shear zones parallel to the STD (T11N56, Fig. 4f; T11N29; T11N30), or strongly deformed sills (T11N25). Mineralogy includes tourmaline, muscovite and rare garnet, sillimanite, andalusite and biotite. When several granites types are presents on the same outcrop tourmaline leucogranites are always the oldest intrusion.

All the granites can be classified as highly peraluminous (ASI>1.1, with ASI = $Al_2O_3/(CaO+Na_2O+K_2O)$). Samples chemical composition is relatively variable, SiO2 ranges from 64 to 85 wt %, Al2O3 from 8.4 to 20.7%, MgO from 0.03 to 0.96%, CaO from 0.2 to 3.1%, Na2O from 1.3 to 4.1 and K2O from 2.3 to 6.8% (Table A22). The two-micas leucogranites and biotite granites as well as the leucopegmatites share similar geochemical composition. However, the tourmaline leucogranites show higher Rb and Nb contents Rb/Sr, Rb/Ba ratios and lower Ba, Sr, Pb, CaO and Zr contents than the other granites (Fig. 6).

5. U-Th/Pb Geochronology in the Nyalam GHS

Two sets of 5 and 15 samples were dated by zircon and monazite respectively. Examples of locations of spot measurements are shown on Fig. 7. All U-Th/Pb detailed results are given in tables A1 to A21, while a summary is given in table 2, and the plots shown in Fig. 8 (monazites) and Fig. 9 (zircons).

5.1 Timing of migmatisation and late dykes within unit 2.

In order to constrain the age of migmatisation a thinly laminated metatexite has been sampled at site T167 (T11N09) as well as two undeformed dykes that crosscut all ductile structures at sites T167 (T11N08, ~10 cm wide tourmaline leucogranite) and T168 (T11N11, ~10 cm wide two micas leucogranite) (Fig. 4a, b). At site T168 a large leucopegmatitic sill that appears to crosscut the metatexite banding but to be affected by the same fold as the migmatitic banding (Fig. 4b) was also sampled (T11N10).

For sample T11N09, 21 analyses both on rims and cores of 21 different monazite grains, that crystallized together with biotite at quartz and feldspar joint boundaries, yielded a Concordia age of 17.8 ± 0.1 Ma. (MSWD = 1.18) (Fig. 8a, Table A2).

The 20 analyses performed on cores and borders of 20 different monazite crystals from sample T11N08 give concordant to subconcordant data with a mean $^{208}Pb/^{232}Th$ age of 15.8 ± 0.2 Ma (MSWD = 0.9) (Fig. 8b, Table A1).

The age of the undeformed dyke is significantly younger than that of the metatexite it crosscuts. We interpret the monazite ages as corresponding to the time of the end of migmatisation for T11N09 and the time of dyke intrusion for T11N08.

The undeformed dyke at site T168 (T11N11) shows two monazite age populations (Fig. 8c, table A4). The first one corresponds to 18 analyses performed on 17 crystals (both cores and borders) and yields a mean $^{208}Pb/^{232}Th$ age of 16.4 ± 0.1 Ma (MSWD = 1.7). The second one corresponds to two cores with a mean $^{208}Pb/^{232}Th$ age of 20.2 Ma. The main age population most likely corresponds to the crystallisation of the dyke. It is close to that of the other ~N-S trending undeformed dyke found at site T167. The oldest population may correspond to preserved earlier monazite grains.

The folded leucopegmatite dyke T11N10 of site T168 did not contain monazite but only zircons. These latter are euhedral with cores, either homogenous or with convoluted zoning, and overgrowths showing oscillatory zoning characterizing magmatic zircon (Fig. 7b). Overgrowth ages define a population (16 data) with $^{206}Pb/^{238}U$ ages ranging from 18.6 Ma to 20.3 Ma (population 1, Fig. 9a, Table A3). The high MSWD (5.1) could indicates crystallization during ~2 Ma but rather indicates a poor quality of the data related to high U contents and metamictisation. A plot of the 10 youngest points with the lowest U content provides a lower intercept with Concordia at 19.0 ± 0.3 Ma (MSWD = 2.0). Cores systematically yield older concordant age of about 26 Ma (3 data) (Fig. 7b) and 31 Ma (one data). The core may correspond to inherited zircons formed by subsolidus growth at the onset of partial melting during prograde metamorphism and not fully dissolved in the granitic melt. The youngest age at 19.0 ± 0.3 Ma may correspond to the sill crystallisation. In accordance with the structural relationships this age predate that of the late dykes (i.e. T11N11).

5.2 Timing of migmatisation and late dykes within unit 3.

Within unit 3, two late dykes that crosscut the ductile structures have been sampled at sites T181 (few meters wide two micas leucogranite T11N42) (Fig 3c) and T182 (20 cm wide biotite granite T11N45) (Fig 3d). Both dykes trend NNE-SSW and dip ~45° to the west (Fig. 2d).

All 14 monazites analyses in T11N42 yielded sub concordant data with a mean $^{208}Pb/^{232}Th$ age of 16.5 ± 0.1 Ma (MSWD = 1.1) (Table A7, Fig. 8d). All monazites from T11N45 also give sub concordant data, with a mean $^{208}Pb/^{232}Th$ age of 16.8 ± 0.2 Ma (23 data, MSWD = 1.18) (Table A9, Fig. 8e). We interpret these ages as the time of dykes crystallization. These two ages are similar within errors to the ages of the late ~N-S dykes within unit 2.

The biotite- and garnet-bearing leucopegmatite migmatitic pocket T11N44 found within orthogneiss at site T182 (Fig. 4d) yielded monazites. 21 of the 23 analyses performed on 23 different grains give sub-concordant data ranging in $^{208}Pb/^{232}Th$ age between 19.8 and 20.5 Ma (average of 23.4 ± 0.3 Ma population 1, MSWD = 2.2) (Fig. 8f, Table A8). Two monazites, similar on SEM images, give younger concordant ages at ~20 Ma (population 2) which may correspond to a limited crystallisation event. We interpret that the migmatite crystallized at ~23.4 Ma.

The large biotite leucopegmatite T11N47 found at site T183 is undeformed and exhibits biotite crystals several cm long (Fig. 4e). It crosscuts marbles exhibiting an horizontal foliation. 19 monazite data from cores and rims of 17 grains define a single sub-concordant population with $^{208}Pb/^{232}Th$ ages ranging from 21.5 to 23.5 Ma with a large MSWD of 3.8 (Table A10, Fig. 8g). When the four youngest grains are removed, the 15 remaining points yield a mean $^{208}Pb/^{232}Th$ age of 22.8 ± 0.2 Ma (MSWD = 1.9). We interpret this age as corresponding to the timing of pegmatite crystallization.

At site T181, leucopegmatite sills crosscut the isoclinal folds affecting the migmatitic gneiss but are cross-cut by the late N-S dykes (Fig. 4c). T11N41 from a ~20cm wide sill yielded monazites and zircons. 31 monazite data define two main age populations with scattered $^{208}Pb/^{232}Th$ ages between 19.3 Ma and 21.6 Ma for the population 1 (19 data – MSWD=9.7) and between 28.1 Ma and 29.5 Ma for the population 2 (9 data – MSWD=2.5) respectively (Table A5, Fig. 8h). Some of the analyzed monazite grains have recorded both the 20 Ma and 29 Ma events.

T1N41 zircons are euhedral with homogenous or sector zoning core and thin late overgrowth sometime showing oscillatory zoning. High U concentrations may be related to metamictization. From the 23 zircons analyses three age populations have been distinguished (Table A6, Fig. 9b). The youngest and major population (13 analyses – population 1), with a lower intercept age of 20.7 ± 0.3 Ma, (MSWD = 2.3) mostly corresponds to late overgrowth (e.g. zircons 4, 11 and 9 Fig. 7a). When the four oldest data are discarded, population 1 yields an age of 20.5±0.2 (MSWD = 0.6). The oldest population yield a lower intercept age at 29.2 ± 0.3 Ma (7 analyses, MSWD = 1.04, population 2) and corresponds only to cores (e.g. zircons 4, 11 and 9 Fig. 7a). Three intermediate ages (25 to 26.4Ma) where obtained from outer core zones. The intermediate ages may result from mixing of old and young domains.

The zircons and monazite broadly define the same age populations and zircon magmatic overgrowth clearly precise the age of the sill crystallization at 20.5 ± 0.2 Ma. This crystallization age is older than that of the late dykes, in agreement with field relationships. The oldest population at ~29 Ma could correspond to subsolidus zircons and metamorphic monazites that where preserved within the magma.

5.3 Timing of granite emplacement and deformation linked with the STDS in unit 4.

As in units 2 and 3, some undeformed dykes crosscutting all ductile structures are found in unit 4. At site T209, sample T11N38 was sampled in a biotite granite ± muscovite vertical ~30cm wide dyke trending N 130 (Fig. 4i, j). Out of 23 monazites analysis performed on 20 grains, 17 define a population with a mean $^{208}Pb/^{232}Th$ age of 17.2 ± 0.2 Ma (population 1, MSWD = 0.52) (Table A13, Fig. 8i). Two other grains, with 3 analyses in each, range in $^{208}Pb/^{232}Th$ age between 28.6 and 30.2 Ma (population 2, average 29.4 ± 0.7 Ma, MSWD = 3.5). These grains have significantly higher U contents suggesting crystallization from an earlier different melt then inheritance into the dyke emplaced at ~17.2 Ma.

T11N34 is a vertical ~30 m wide aplitic 2 micas granitic dyke trending N160 sampled at site T207 (Fig. 4g). It looks undeformed and crosscuts all other dykes and ductile structures, but shows a faint foliation trending N30, 40N. 23 monazite measurements on 23 different grains define a single population with a mean $^{208}Pb/^{232}Th$ age of 15.3 ± 0.1Ma (MSWD = 0.39) (Table A16, Fig. 8j) that we interpret as the timing of the dyke crystallisation.

T11N39 was sampled in a large undeformed aplitic two micas leucogranite at site T210. 22 monazite measurements from 22 different grains, define a single $^{208}Pb/^{232}Th$ age population at 15.4 ± 0.2Ma (MSWD = 1.00) (Table A14, Fig. 8k). This age is taken as the age of the leucogranite crystallisation.

T11N56 is a tourmaline leucogranite sampled at site T188 ~ 13 km south of the STDS (Fig. 2). The leucogranite is undeformed except for a few very localized zones, and shows large paragneiss rafts (Fig. 4f). However a shear zone trending N102, 35N with a N-S lineation and top to south shear criteria locally affects the leucogranite. This shear zone could be linked with deformation of the STDS. 21 monazite measurements have been performed on 17 grains. 14 grains, 4 of which with data both on rim and core, define a population with a mean $^{208}Pb/^{232}Th$ age of 17.5 ± 0.2Ma (population 1, MSWD = 1.6) (Table A11, Fig. 8l). Three other concordant data give older $^{208}Pb/^{232}Th$ ages of 20.3, 24.3 and 25.4Ma. These older ages may be related with inherited grains from the melted source or the paragneissic rafts.

At site T206, 500 m structurally below the STD, another large tourmaline leucogranite has been sampled. T11N30 corresponds to its undeformed part that did not contain monazite but only zircons. Zircon grains show clear overgrowth, sometime with oscillatory zoning. The 5 most concordant data among 8 measurements, corresponding to the lowest U content within these overgrowths give a mean $^{206}Pb/^{238}U$ age of 18.8 ± 0.3 Ma (MSWD = 0,46) (Table A18, Fig. 9c). The very high U contents suggest that these zircons are metamict and subject to Pb loss, implying that the age is a minimum. 7 other data measured both from cores of the same grains and from core and rims of other grains give much older $^{206}Pb/^{238}U$ ages of about 425-473Ma (4 concordant points), 190Ma (discordant), 172 Ma (discordant) and 100 Ma (discordant) (Table A18, Fig. 9d).

T11N29 corresponds to a deformed zone of the same leucogranite with a foliation trending N40, 40 N and a lineation with an azimuth N50 sub parallel to the STD shear zone. 17 measurements have been performed on 14 different monazite grains (Table A17). 15 data yield $^{208}Pb/^{232}Th$ ages ranging from 20.4 to 21.8 Ma (population 1, average 21.9±0.2, MSWD = 2.9), with one grain at 30.8 Ma (Fig. 8m).

The monazites in the deformed granite are ~2 to 3 Ma older than the zircon overgrowth within the undeformed leucogranite. Given the possible metamict nature of the zircons we prefer to rely on the age of the monazite population 1 to constrain the leucogranite crystallisation age between 20.4 and 21.8 Ma.

At site T209 biotite leucopegmatitic sills are subconcordant to the foliation and show boudinage structures (Fig. 4j). According to Liu et al. [2012], T11N37 from one of these sills yielded two monazite age populations. Most monazite analyses (20), define a population with a mean concordant age of 27.4 ± 0.2 Ma (population 1, MSWD = 0.52). Five other analyses from cores define another population with a mean $^{208}Pb/^{232}Th$ age of 30.1 ± 0.4 Ma (population 2, MSWD = 0.21, Fig. 7c).

Zircons from the same sample are euhedral. Dating of the rims as well as the cores give a lower intercept age of 26.4 ± 0.3 Ma (population 1, 10 analyses, MSWD = 0.7) (Table A12, Fig. 9e). One of the cores yields a sligthly older concordant age of 28.4 ± 0.7 Ma (1.2c, Table A12, Fig. 9d). Four data yield a younger lower intercept age of 22.8 ± 0.3 Ma (population 3, Table A12, Fig. 9d). These data come both from rims and core of zircons (Fig. 7d) that contain several thousand ppm of U. Consequently, owing to the possible metamict behaviour of the zircon lattice, these ages will be considered as minimum estimates.

The age of the main zircon and monazite populations (populations 1) are quite similar. We interpret this to reflect the crystallisation of the sill for which the monazite age of 27.4 ± 0.2Ma seems to be the most reliable. The oldest zircon core and the monazite population 2 give close ages that we interpret as inherited ages. The younger zircon population at ~23 Ma possibly corresponds to Pb-loss related to the very high U content of some grains.

At site T207, two other generations of granite have been sampled beside the late dyke T11N34. T11N32 is a biotite granite showing deformation similar to T11N37 (Fig. 4g, h). According to Liu et al. [2012] 16 monazite measurements yield concordant data and a mean $^{208}Pb/^{232}Th$ age of 22.0 ± 0.3Ma (MSWD = 1.9). We interpret this age as the emplacement of the dyke.

T11N33 is a ~7cm wide tourmaline leucogranite dyke that crosscuts T11N32 (Fig. 4h). It is only sligthly deformed and is cut by T11N34. 24 monazite measurements define a single population with a mean $^{208}Pb/^{232}Th$ age of 15.6 ± 0.1Ma (MSWD = 0.34) (Table A15, Fig. 8n). This dyke emplacement age is consistent with the field relationships: ~0.3 Ma older than T11N34 and ~6.4 Ma younger than T11N32.

No undeformed rocks are found crosscutting the foliation in the STD shear zone nor the STD itself. T11N25 is a tourmaline leucogranite that has been strongly deformed just below the STD. Liu et al., [2012] describe that the zircons show clear oscillatory zoning, sometime surrounding a rounded core. 7 measurements (core and rim) give a lower intercept age of 17.1 ± 0.2Ma (MSWD = 1.4) interpreted at the emplacement age [Liu et al., 2012]. Three outliers, from inherited core, give $^{206}Pb/^{238}U$ age of 2.25 Ga (discordant), 679 Ma (concordant) and 365 Ma (concordant).

6. New Ar/Ar data in the Nyalam GHS

Previous Ar/Ar data [Maluski et al. 1988; Wang et al., 2006] (Fig. 1e) help to constrain the Nyalam section cooling history (Fig. 11). In order to discuss the timing of brittle deformation we sampled micas crystallizing in late structures such as fault planes and tension gashes. We describe the results from the base to the top of the section.

The gas released by the samples show significant amounts of atmospheric argon, leading to amounts of radiogenic ^{40}Ar often below 50% of the total ^{40}Ar released. This translates into large errors for individual steps and thus fairly large overall errors on age plateaus and isochrones. However individual ages of each step involved in the plateaux are close to each others (Fig. 10), suggesting that the calculated propagated error is probably oversestimated. For all samples, the plateau and isochron ages are identical within errors and the $^{40}Ar/^{36}Ar$ ratio deduced from the isochron is not significantly different from the present day atmospheric one (Table 3), yielding to consider only the plateau ages.

Gashes and brittle faults were observed at site T158 within unit 1 (Fig. 1d, Fig. 2). T11N01 was sampled in a quartz gash containing white micas and striking N175, 67W (Fig. 2b). T11N01a corresponds to the gash itself and T11N01b to the surrounding rock. Muscovites from T11N01a give a plateau age of 4.8±0.8 Ma (Table 3, Fig. 10a, Table A23, all ages are quoted at the 2σ level).

Muscovites from T11N01b give a slightly older plateau age of 6.3±0.8 Ma, while the inverse isochron could show a slight excess of trapped argon leading to an isochron age of 5.6±1 Ma (Table 3, Fig. 10b, Table A24). Ages of both samples are thus almost identical within error whilst the gash age is slightly younger (Fig. 1e). We interpret these ages as reflecting opening of the gash at ~5 Ma. Because the age of muscovites of the gash and of the surrounding rock are similar, we interpret this age as reflecting the gash formation at the lowest possible closure temperature for white micas around 300°C.

In the same outcrop, sample T11N03 corresponds to a releasing bend in a fault trending N145, 37 NE and bearing striation with a N178 azimuth. The fault is reverse / dextral and thus could results together with the gash from an ~N-S $\sigma1$ and an ~E-W $\sigma3$. Biotites from T11N03 show a plateau age of 10.9±0.4 Ma (Table 3, Fig. 10c, Table A25). We interpret this age as that of the fault formation at ~300°C.

At site T162 at the base of unit 2 (Fig. 1d), T11N05 was sampled in a late quartz gash trending N10, 70 E (Fig. 2b) and containing white micas. T11N05a corresponds to the gash itself and T11N05b to the surrounding rock. Muscovites from T11N05b gives a plateau age of 17±0.8 Ma (Table 3, Fig. 10e, Table A27). This age is interpreted as a cooling age and is compatible with the cooling history of unit 2 (Fig. 11b). Muscovites from T11N05a give a significantly younger plateau age of 8.8±0.4 Ma (Table 3, Fig. 10d, Table A26). Given the cooling history of unit 2 that age could also be interpreted as a cooling age (Fig. 11b). However the fact that it is significantly younger than that of the surrounding rock yield us to consider that it corresponds to the gash formation, slightly below the closure temperature of white micas (Fig. 11b).

Close to the northern limit of unit 2, other steep brittle quartz gashes trending close to N-S are found at site T167 (Fig. 2c). T11N07 was sampled in one gash containing white micas. These white micas yield a plateau age of 15.2±0.6 Ma (Table 3, Fig. 10f, Table A28) that, as for T11N5a, we interpret as the time of the gash formation.

At site T185 within unit3 (Fig. 1d) a brittle fault trends N 165, 60E with slikensides with a pitch of 65 N. Such fault is probably right lateral / reverse and compatible with a N-S compression. The fault plane bears biotite, chlorite and muscovite. Biotites of sample T11N21 from that fault plane yield a rough age spectra of 17.7±0.8 Ma (Table 3, Fig. 10g, Table A29). This age is close to other biotite Ar/Ar published ages from nearby samples (Ti4 and Ti5, Maluski et al. [1988]) (Fig. 1e), suggesting it is a cooling age that gives a lower bound to that of the fault.

T11N51 was sampled in a gash trending N105, 52 S at site T212 within unit 4 (Fig. 2e). The gash contains quartz, tourmaline and white micas. The white micas show a plateau age of 8.8±0.3 Ma (Table 3, Fig. 10h, Table A30). This age is close to that of a nearby apatite fission track age (T4, Wang et al. [2010]) (Fig. 1e) suggesting that it corresponds to that of the gash formation below the nominal closure temperature of white micas.

7. Discussion.

7.1 Timing constraints on partial melting in the GHS series beneath the Nyalam detachment.

Two main families of leucogranites have been recognized in the GHS: two-micas leucogranites and tourmaline leucogranites (Le Fort et al., 1987). The granites from this study are geochemically undistinguishable from these two families: the biotite granites and the two-micas leucogranites plot in the low Rb/Sr field while the tourmaline leucogranites plot in the high Rb/Sr field (Fig. 6, see Visona & Lombardo, [2002] and Guo and Wilson, [2011] for a review). Granites showing high Rb/Sr ratios are usually associated with vapour-absent muscovite melting while low values suggest biotite destabilization in the source (Inger and Harris, 1993, Visona and Lombardo, 2002). Thus the tourmaline leucogranites may result from muscovite breakdown while the other granites would also involve biotite breakdown (Inger and Harris, 1993, Visona and

Lombardo, 2002). However, Guo and Wilson, [2011] suggest that all Himalayan granites resulted from the melting of a biotite-rich source devoid of muscovite, and that some of their geochemical characteristics result from metasomatism by fluids from the LHS.

Of the twenty samples only three show pre Oligocene inherited ages. These are only found in zircons and monazite cores of leucogranites containing tourmaline of unit 4. The oldest concordant ones being Neo-Proterozoic (679 Ma, T11N25), Lower Devonian (411Ma, T11N32) and Ordovician-Silurian (425-473Ma, T11N30) (Table 2). The small number of samples does not allow further interpretation of these ages.

Most U-Th/Pb ages are Miocene and they all span between ~15 and ~31 Ma. On Fig. 1e they are plotted as a function of the horizontal distance to the Lower MCT. From our data, the crystallization age of 17 rocks can be determined, spanning from ~27 to ~15 Ma (Fig. 1e, Table 2).

All six late dykes (T11N08, T11N11, T11N42, T11N45, T11N38, T11N 34) from units 2, 3 and 4 show crystallisations ages between 15.3±0.1 and 17.2±0.2 Ma. They are all steep and trend N-S to NW-SE but have various mineralogy. This documents a late magmatic period (~17-~17.5 Ma, LD on Fig. 12b) postdating the main ductile deformation at a time when σ3 trended E-W to NE-SW. These dykes do not seal deformation in the STD shear zone (top of unit 4) where no late dyke is found. In that zone, a sill has an emplacement age of 17.1 ± 0.2 Ma (T11N25 zircons). This sill is strongly deformed implying that deformation in the STDsz over-lasted deformation in units 2, 3 and 4 [Liu et al., 2012]. Wang et al. [2013] describe an undeformed cross-cutting leucogranitic dyke (sample TYC-64) for which three SHRIMP weighted mean $^{206}Pb/^{238}U$ ages are proposed, the youngest being 14.1 ± 0.7 Ma. This age is taken as the end of ductile deformation in the STD shear zone. However, according to their cross-section the sample is ~1600m structurally below the STD, thus below the STD shear zone. The age of the dyke, whilst imprecise (MSWD = 3), is close to that of the undeformed dyke T11N34 sampled 1500m below the STD (15.3±0.1

Ma) (Fig 1e) and we consider it belongs to the same late magmatic period. Unit 4 T11N39 undeformed aplitic two micas leucogranite also yields an emplacement age (15.4 ± 0.2 Ma) in the same range as the late magmatic period. This is coherent with field observations showing that several undeformed dykes originate from this granite body. T11N56 tourmaline leucogranite emplaced at 17.5 ± 0.2 Ma near the base of unit 4, and we consider that it also belongs to the late magmatic period. It is affected by shear zones parrallel to the STDsz confirming that deformation related to the STD lasted after 17.5 Ma.

Age of the end of partial melting in units 2 and 3 may be constrained from the crystallization ages of the migmatite and/or pegmatite that have not migrated from their source level. Unit 2 T11N09 migmatite (Fig. 4a) crystallized at 17.8 ± 0.1 Ma. Unit 3 leucopegmatite T11N44 has not migrated from its source zone (Fig. 4d) and crystallized between 22.4 and 24 Ma. This suggests that crustal partial melting lasted until at least ~18 Ma in unit 2 and ~22 Ma in unit 3. Other pegmatitic levels (T11N10, T11N41 and T11N47) give slightly different crystallization ages that suggest that crystallization lasted at least between ~19 and ~18 Ma in unit 2 and between ~24 and ~20 Ma in unit 3. According to Wang et al. [2013] zircons from a sillimanite bearing mignatitic gneiss (sample NY11-2) from zone 3 yield laser-ICPMS U/Pb ages spanning from 39.7±0.3 to 34.0±1.7 Ma that they have interpreted as reflecting an early long-lasting partial melting event. However, the $^{206}Pb/^{238}U$ subconcordant ages span from 64 to 28.4 Ma and a concordia drawn through all data yields an upper intercept at 268±90 Ma and a lower intercept at 36.2±5.1 Ma (MSWD = 1.7). Furthermore, a rim yields a concordant age of 28.4±0.5 Ma. These later ages are within error of our older ages within zircons of unit 2 and 3 (Fig. 1e) and very probably do not date the timing of crystallization in migmatites of these units (see below). Consequently, the conclusions of Wang et al. [2013] on the duration of migmatization may suffer from possible mixing of age populations, and /or inheritance.

Unit 4 is mostly devoid of in-situ partially melted rocks and the numerous dykes and sills probably originated from units 1, 2 and 3. Beside the late dykes, granite crystallization in unit 4 (T11N29, 32, 37) occurred between ~27.5 and ~20.5 Ma (Fig. 1e, granites emplacement on Fig. 12b). There is no relationship between age and granite type suggesting that the granite source did not change between ~ 27.5 and ~15 Ma.

Seven samples (T11N10, 11, 29, 37, 38, 41 and 56) show inherited Tertiary ages (Fig. 1e, Table 2). Attribution of inherited ages to a precise context (prograde or retrograde) is not straightforward. Five of the seven samples have their oldest Tertiary inherited ages between 31 and 29 Ma and no older Tertiary age is present (Fig. 1e), suggesting that a major event occurred at ~30 Ma. All three samples containing zircons show such age in their cores. Along clockwise P-T zircons mostly form or overgrow in these lithologies at the onset of partial melting and in the melt. P-T path deduced from garnet thermobarometry in unit 3 reach the muscovite breakdown at ~700°C and ~7 Kb (700 MPa, B and C on Fig. 3c) [Hodges et al., 1993; Wang at al., 2013]. The simplest interpretation is that the oldest monazite and zircon inherited ages correspond to crystallization during prograde metamorphism at the onset of partial melting. This would suggest that: a) partial melting started at the same time in units 2 and 3 (~30 Ma); b) melts emplaced quickly in the whole overlying pile up to just below the STD (T11N29, 37, 38); c) partial melting lasted ~12 Ma in the top of unit 2 (until ~18 Ma) and possibly stopped ~2 Ma earlier in unit 3 (until ~20 Ma) (Fig. 12b). Such Oligocene prograde metamorphism has classically been called Eohimalyan (M1). It most probably results from burial to at least 30 km depth (8kb, Fig. 3c). Normal motion on the STD at the top of unit 4 cannot explain such burial. However T11N26 CPO and folds in the THS suggest that early top-to-the-SW shear sense (reverse) preceded top-to-the-NE (normal) motion along the STD. Other evidences for early top-to-the south motion have been found in other locations along the Himalayas [e.g., Vannay and Hodges, 1996; Coleman and Hodges, 1998; Godin et al., 2001; Vannay et al., 2004] suggesting that a major South Tibet thrust active prior to 30 Ma, preceded the STD. Whilst the prograde evolution of units 2, 3 and 4 is not well constrained they most probably followed a clockwise P-T path that crossed the water saturated melting curve around ~8kb and ~600°C approximately 30 Ma ago (Fig. 3c). Further melting may have been enhanced by the exhumation yielding the P-T path to reach the muscovite breakdown (B and C on Fig. 3c).

Because they are only found from the top of unit 2 to below the STD, the late dykes probably originate from the base of unit 2 or from the top of unit 1. This would indicate that partial melting lasted until ~15 Ma at this location. Two of these dykes (T11N11 and T11N42) clearly cut the isoclinal folds with ~horizontal axial plane affecting units 2 and 3, and yield crystallisation ages of 16.4 ± 0.1 and 16.5 ± 0.1 Ma. T11N10 folded layer has a crystallization age of 19.0 ± 0.3 Ma. This implies that isoclinal folding ended after ~19 and prior to 16.5 Ma in units 2 and 3.

7.2 Cooling of the GHS along the Nyalam section and timing of brittle deformation.

Because all units of the GHS have reached temperature above 500°C during the Tertiary metamorphism (Fig. 3), analysis of the thermochronological data (Ar/Ar and FT) allows discussing their cooling histories. Together with the analysis of the temperature conditions of deformation and the P-T paths of the country rocks these data allow to describe further the P-T-t-D paths of the main units (Fig. 3).

All muscovite and biotite Ar/Ar ages in units 3 and 4 are comprised between 16.6 and 14 Ma, the only exception being a late gash (T11N51) which is ~9Ma old [Maluski et al., 1988; Wang et al., 2006, this study] (Fig. 1e, Fig. 11a). This suggest cooling below ~ 320°C before 14 Ma in both units. In contrast, biotite and muscovite Ar ages in unit 2 span between ~4 and 15 Ma. The cooling history of unit 2 based on all available ages suggest that fast cooling took place between ~18 and ~16 Ma (Fast cooling FC1, ~200°C/Ma) (Fig. 11b) but was followed by an isothermal period at ~250-350°C for ~10 Ma until fast cooling resumed at ~6Ma at a rate of ~75°C/Ma [Wang et al., 2010] (Fast Cooling FC3, Fig. 11b).

FC1 was coeval in units 2, 3 and 4 (Fig. 11, Fig. 12b). At the top of unit 4, in the STD shear zone, FC1 was immediately followed by another fast cooling episode (fast cooling FC2, ~150°C/Ma) that lasted until ~13 Ma and ~100°C (Fig. 11a) [Wang et al., 2006; Liu et al., 2012]. Since then there was less than 3km exhumation of the STD footwall.

The first cooling episode (FC1) is very fast and partly coeval with the emplacement of the late dykes between ~17.5 and ~15 Ma (Fig. 11b, Fig. 12b). Such rapid cooling most likely results from generalized unroofing of the UGHS. This is not compatible with underthrusting below the South Tibetan Thrust but rather with thrusting above the MCT zone. This would imply that the top-to-the-south trusting in that zone initiated prior to 18 Ma. After 16 Ma the prolongation of FC1 at the top of unit 4 by another, possibly slightly slower, cooling (FC2, ~150°C/Ma) more likely results from continued unroofing associated with down to the north slip on the STD until ~13 Ma [e.g., Wang et al., 2010; Leloup et al., 2010]. This would imply that the STD had a significant dip (≥ 20°) in order to induce vertical motion and thus rapid cooling, This would also imply that the STD initiated before 16 Ma, and was still active ~7Ma, ~5Ma and ~2Ma after partial melting ended in units 3 , 2 and 1 respectively (Fig. 12b).

Steep gashes filled by quartz and trending N160 to N-S are found in units 2 and 3. Their orientation is close to that of the late dykes found in unit 2. Both the dykes and gashes are compatible with an ~E-W trending σ3. The dykes (T11N08 and T11N11) emplaced between 16.4 and 15.8 Ma (Table 2, Fig. 1e) and the gashes (T11N01a, T11N05a, T11N07) span in age between 15.2 and 4.8 Ma (Table 3, Fig. 1e). This confirms that temperature at ~15 Ma was cold enough (≤ 300°C) in unit 2 for the formation of brittle gashes less than 3 Ma after the crystallization of the migmatite (T11N09, 17.8 Ma) and hence the age of the fast cooling 1 (Fig. 11b). The stability of the orientation of the structures through time also suggests that the local direction of σ3 has not significantly changed between 16.4±0.1 and 4.8±0.8 Ma. Two faults compatible with an horizontal ~N-S σ1 yield ages of 10.9±0.4 (T11N03 at the base of unit 2) and ≥17.7±0.8

(T11N03 unit 3) suggesting that the direction of σ1 stayed stable at least between ~11 and ~18 Ma while the rock significantly cooled and exhumed.

The last fast cooling (FC3, 6-0 Ma) observed at the southern end of the Nyalam section has been interpreted as resulting from rapid erosion due to a major climate change [Wang et al., 2010]. However, such cooling may result from other causes and will be discussed in section 7.4.1 at the light of data from the Lantang section.

7.3 Geometry and timing of deformation of the STD system.

7.3.1. Large scale geometry of the STDS.

A major feature of the STDsz, that has been overlooked by most authors, is that the stretching lineations indicating the motion direction are not down-dip, but systematically trend ~N30° between 86 and 89°E (Fig. 1b, Fig. 2f). Pêcher [1991] attributed this direction to a significant dextral component of deformation along the STDS. A cross section of the STDS along the N30 direction (Fig. 8) reveals a geometry that differ from the one that is usually depicted (Fig. 13). From SSW to NNE, the STD dips ~30 degree to the north (X, N on Fig. 13, location on Fig. 1b) before a 50 km long flat (C, R, S on Fig. 13, location on Fig. 1b). North of Rongbuk, the Yellow Band Formation is excised and the STD roots down is a shear zone dipping ~30 degree to the north (D on Fig. 13) as already shown in cross sections by Carosi et al. (1998). In this area, Silurian to Jurassic folded Tethyan sediments outcrop above (north) of the STDsz, suggesting a total offset of the Middle Cambrian Yellow Band Formation on the order of 40km (Fig. 13). Further to the east (Z Fig. 1b), an ~25° north dipping set of reflections along the INDEPTH seismic profile has been interpreted as the STDS trace down to ~27km depth [Hauck et al., 1998]. Below the Yellow Band Formation, intense top-to-the-NE simple shear deformation is concentrated in the 150 to 600 m thick STDsz. Geometry of the STD and STDsz correspond to that of a normal fault duplex. Below the STDsz, distributed pure shear deformation affect a ≥ 4 km thick section of the GHS.

In Nyalam the simplest interpretation of our structural observations at the top of unit 4, below the STD are: 1) stratigraphy and structural relationships in the ZhaSongLe valley resembles those of the Rongbuk valley; 2) Ductile deformation linked to the STDS affected a section at least 3.5 thick, but top-to-the-north simple shear was intense only in the ~300 m thick STDsz below the STD; 4) Below the STD shear zone, pure shear was important and locally evidences for top-to-the-SW shear sense can be found.

7.3.2. Timing of end of motion along the STD.

Near the Chomolangma summit (C Fig.1b) apatite and zircon fission tracks ages from the Yellow Band Formation suggest that the STD was still active at ~14.4 Ma because fast cooling was taking place at that time in the footwall [Sakai et al., 2005]. Further east, in the Saer area (S Fig.1b) U/Pb dating of monazites and zircons in deformed and undeformed leucogranites suggests that ductile deformation lasted until at least ~16 Ma but ended prior to 15 Ma in the STD shear zone ~100 m below the detachment, and Ar/Ar micas ages in the footwall indicating rapid cooling suggest persistence of normal faulting until ~13.6 Ma [Leloup et al., 2011]. In that zone, the N–S trending Dinggye active normal fault, that cut and offsets the STD initiated prior to 11 Ma [Kali et al., 2010]. Leloup et al., [2011] interpreted these data as reflecting 11 km to 22 km of exhumation along the STDS starting prior to 16 Ma and ending between 13.6 and 11 Ma. Using published cooling histories of the STD footwall they further suggested that a 1000 km long stretch of the STDS east of the Gurla Mandata stopped almost synchronously between 13 and 11 Ma ago.

The data presented in this paper are compatible with such timing with the end of STD motion at ~13 Ma in Nyalam. The age of initiation of the STD his much more difficult to constrains. Our data only suggests it started later than ~30 Ma ago time at which the South Tibetan thrust was active, and prior to 16 Ma time of the onset of FC2. If one considers that FC1 is also related to motion on the STD it would imply an initiation at or prior to ~18 Ma.

7.3.3 Vertical migration of deformation below the STD: a possible bound for the onset age of the STD.

It has been suggested that deformation progressively localized upward in the GHS below the STDS [e.g., Leloup et al., 2010; Cottle et al., 2011], but this could not be quantified. Our study documents a diachronous end of pervasive deformation within the unit 4 along the Nyalam section, from prior to ~ 17.2 Ma ~3500 m structurally below the STD to ~13 Ma on the STD itself. Deformation end migrated upward at a rate of 0.8±0.3 mm/yr between sites T207 and T204 (Fig. 14). If this rate is extrapolated downwards, it would imply an end of the deformation at site T209 at ~17.9 Ma, which is compatible with the age of the undeformed dyke T11N38 (17.2 ± 0.2 Ma) (Table 2, Fig. 4).

North of the Chomolongma, in the Rongbuk valley other data suggest a vertical migration of the end of deformation. Three dykes yield essentially the same $^{208}Pb/^{232}Th$ monazite ages: 16.8 ± 0.8 Ma for a crosscutting dyke (~650 m below the STD), 16.4 ± 0.6 Ma for a crosscutting but deflected dyke (~350 m below the STD) and 16.2 ± 0.8 Ma for a mylonitic dyke (~150 m below the STD) [Murphy and Harrison, 1999]. This implies that deformation was over at ~16.8 Ma ~650 m below the STD but was still ongoing after ~16.2 Ma within the STSsz. Deeper in the GHS, ages of deformed leucogranites and undeformed leucogranites in the Kangshung valley (C Fig. 1b), ~2.5 km structurally below the Lohtse detachment, suggest that deformation ended between 20.9 ± 0.4 (KG07 deformed sill) and 16.7 ± 0.4 Ma (KG06 undeformed sill) [Cottle et al., 2009]. In the Dzakaa Chu section (D Fig. 1b), there is no clear brittle STD but a ~600 m thick STDsz. Ages of undeformed dykes at the base of the STDsz, imply that deformation stopped prior to ~20 Ma [Cottle et al., 2007]. Titanites within calsilicates from the same outcrop, and from two other locations above in the STDsz, yield U/Pb ages between 14 ± 0.3 and 12.8 ± 0.6 Ma [Cottle et al., 2011]. If, as suggested by Cottle et al. [2011], these ages are syntectonic they would imply that ductile deformation lasted until ~13 Ma, but would contradict the age of the undeformed dykes. The more likely interpretation is that deformation stopped at ~20Ma at the base of the STDsz and that titanites crystallized during the last fluid circulation episode prior to the stop of the STD at ~13 Ma.

When these timing constraints are reported along a N30 trending section a coherent pattern arises (Fig. 15). Last motion on the STD occurred ~13 Ma ago, but deformation stopped earlier within the GHS. From the available data isochrones for the end of ductile deformation (IED) can be drawn (Fig. 13, Fig. 12). As the STD stopped at ~13 Ma, the 13 Ma IED follows the brittle part of the STD and prolongates in the STDsz at Dzakaa Chu. IED in the GHS are flatter than the STD (Fig. 13). The fact that diffuse deformation stops first at depth could be the result of a progressive localization of deformation combined with a southward / upward propagation of the shear zone. Deformation probably started by distributed vertical flattening in the GHS, before to localize in the STDsz. At a given depth distributed deformation most probably stops when deformation starts to be taken up in a localized way within the shear zone. If this switch in deformation style is true, the age of the end of distributed deformation would constrain the timing of initiation of the STD shear zone: at ~20 Ma in Dzakaa, ~16.5 in Rongbuk and ~15 Ma in Nyalam. Such initiation ages suggest relatively short duration of deformation until the end at ~13 Ma, for example ~3.5 My in Rongbuk. At this location it would corresponds to a fault rate between 7 and 49 mm/yr for the total slip estimates proposed by Law et al. [2011] of between 25 and 170 km; or of 11.4 mm/yr for the estimated Yellow Band offset (40km see above). In this model the STDS propagated from North (bottom) to South (top) at a rate of ~15 mm/yr from Dzakaa to Nyalam. If this rate is extrapolated backwards down to the extremity of the STD seismic trace, i.e. at ~27km depth, it would suggest that motion on the STDsz started at ~25 Ma. Note however that the STD has moved southward and upwards above the MHT prior to reach is present day position. The 27 km depth is thus a minimum and 25 Ma is a lower bound for the STD initiation.

7.4 Deformation within the GHS and timing of motion on the MCT.

Other geochronological data of the GHS have been published along sections ~100 km both to the west and the east of the Nyalam section. These data help to constrain the timing of deformation above the MCT in the central Himalaya (~85°E-~87°E).

7.4.1 Langtang section.

Along the Lantang section (L on Fig. 1b) high-grade metamorphic rocks of the GHS with metamorphic grade increasing upward are thrust upon the Lesser Himalayan series. As in many other sections two thrusts have been identified near the base of the GHS: the Ramgarh thrust (that we interpret following Searle et al. [2008] as the Lower MCT or MCT1) and the MCT (that we interpret as the Upper MCT or MCT2). Within the GHS, Kohn et al., [2004, 2005] distinguish four generations of monazites whose U-Th/Pb ages can be attributed to early prograde, prograde subsolidus, retrograde subsolidus and alteration crystallisation respectively. Above the MCT2 (equivalent to our unit 1b) such ages are interpreted to indicate that prograde metamorphism lasted from ~36 to ~24 Ma, subsolidus crystalization from ~24 to ~16 Ma, partial melting between ~16 and ~15 Ma and crystallisation from ~15 to ~13 Ma (Fig. 12b). Between the MCT1 and the MCT2 (equivalent to our unit 1a) prograde crystallization takes place between ~20 and and ~13 Ma and is followed by retrograde crystallization until ~10Ma (Fig. 12a). Kohn et al., [2004] further interpret these ages as reflecting activity on the MCT2 and the Ramgarh thrust (MCT1) to take place between 16 and 10.5 Ma and 10.5 and 8.9 Ma respectively.

Ar/Ar ages [Macfarlane et al., 1992] further constrain the cooling history (Fig. 12b). Two biotite and nine muscovite ages are comprised between 8 and 4.6 Ma, and the muscovite age on the MCT is only 2.3±0.4 Ma [Macfarlane, 1993] (Fig. 12a). These ages could suggest a last phase of rapid cooling since ~8 Ma, approximately at the same time as FC3 in Nyalam section. Such young ages have been interpreted as linked with circulation of fluids originated from below the MBT and channelled along the MCT [Copeland et al., 1991] or reflecting recent exhumation. The recent exhumation could results from a) out-of-sequence thrusting along the MCT [e.g., Wobus et al., 2005; Mukherjee et al., 2012 for a review], b) underplating and formation of a mid-crustal duplex in the lesser Himalaya since ~10 Ma [Bollinger et al, 2006; Herman et al. 2010] and c) rapid erosion due to a major climate change [Wang et al., 2010]. The absence of clear evidence for brittle deformation along the MCT does not favour the first hypothesis. The second hypothesis will also explain the general structure of the belt with GHS klippen, such as the Kathmandu one, located ~50 km further to the south and it is the one that we favour. In any case whatever is the cause for this late cooling it is important to note that the frontal emergence of the MCT at the time of the major cooling / exhumation of the GHS was located more than 50 km further south than its present exposure in Lantang and Nyalam.

7.4.2 Dudh Khosi – Everest section.

Along the Dudh Kosi river (DK on Fig. 1b), Catlos et al. [2002] published several in situ Th-Pb ion microprobe ages from metamorphic rocks. The average age of monazite from sample 85H20 just above the MCT1 is 11.8±03 Ma for matrix monazites and 16.4±2.3 Ma for monazites included within garnets (Fig. 12c). In the upper part of the MCT zone two samples yield 15.2 ± 0.2 (ET33) and 14.5 ± 0.1 Ma (ET52) for matrix grains and 13.9±0.5 (ET33) and 16.4±2.2 (ET33) for grains in inclusion within garnets. These ages are similar to the ages obtained along the Langtang section in similar units (Fig. 12). Above the MCT2 most ages range between 25.3 ± 0.2 and 20.9 ± 0.3 Ma (7 samples). These Miocene ages are taken as related to metamorphism contemporaneous with motion on the MCT2 [Catlos et al., 2002]. Such ages are similar as those interpreted to be linked with subsolidus prograde crystallization and partial melting in unit 2 of the Lantang and Nyalam valleys. In the same area Viskupik & Hodges [2001] report monazite and xenotime U-Pb ages on a migmatitic orthogneiss (98E5) that suggest that following an early metamorphic event at ~28.4 Ma partial melting occurred from at least 25.4 to 24.8 Ma and was then followed by late metamorphism from 22.1 to 20.3 Ma. A 17.5 Ma U-Pb xenotime age is related to late dyke emplacement [Viskupik & Hodges, 2001].

The Dudh Kosi - Everest section does not show a unit equivalent to our unit 3, but several U-Th/Pb and Ar/Ar ages of deformed and undeformed rocks have been published from the upper part of the section that corresponds to our unit 4. The 6 late dykes and sills (98E6, 00SK8, 00SK10 and 01SK55 [Viskupic and Hodges, 2005]; KG06 [Cottle et al., 2009]; 98-6-21-9 [Murphy and Harrison, 1999]) range in age between 18.28±0.07 Ma and 16.2±0.8 Ma (LD on Fig. 12c). In the Makalu area Streule et al. [2010] recorded multiple partial melting event in a cordierite leucogranite (A19) and a migmatitic gneiss (A81). Youngest monazite and xenotime U-Pb age range from 15.6 Ma to 17.9 Ma and are related with a second partial melting event following an early melting at about 23-19 Ma [Streule et al., 2010]. The Ar/Ar biotite ages suggest emplacement in a relatively cool environment (370°C) [Viskupic and Hodges, 2005] and / or very fast cooling immediately after emplacement. This is similar to what we have described in Nyalam, but with the late dykes emplacement taking place ~2 Myr earlier (Fig. 12). The other U-Th/Pb ages obtained by Viskupic and Hodges, [2005] indicate crystallization between 26 and 20 Ma. Other published crystallization ages confirm leucogranites crystallization in unit 4 between ~26 and ~18 Ma [Catlos et al., 2002; Cottle et al., 2009; Simpson et al., 2000; Jessup et al., 2008; Streule et al., 2010]. Within the STD shear zone all granites are deformed, because deformation last longer [Murphy and Harrison, 1999] (see section 7.3). Other monazite ages from metamorphic rocks suggest that prograde metamorphism took place since at least 29.9±1 Ma (A19, Streule et al. [2010]), 32.2±0.4 Ma (E137, Simpson et al. [2000]) and 34.8 ±0.4 Ma (A45, Streule et al. [2010]). (Fig. 12c) or even 38.9±0.9 Ma (KG10, Cottle et al. [2009]). The end of motion on the STDS occurred soon after ~14.4 Ma [Leloup et al. 2010].

200 – 300 km further west, monazite U/Pb ages suggest that prograde metamorphism and migmatisation took place from 43 to 33 Ma in the Dolpo area [Carosi et al., 2010], and between 41 and 36 Ma in the Kali Gandaki [Carosi et

al., this volume].

7.4.2 Timing of metamorphism, melting, crystallization and motion on the MCT.

Taken all together these data yield a coherent picture of deformation, metamorphism, melting and cooling in the GHS in the central Himalaya (~85°E-87°E). Prograde metamorphism takes place between ~39 and ~28 Ma followed by partial melting in units 2 and 3 that feed granites emplaced in unit 4. The last magmatic period correspond to undeformed dykes that postdates ductile deformation in units 2 and 3 and takes place between ~17.5 and ~15 and Ma in Nyalam and ~18.5 and ~16 Ma in Dudh Kosi – Everest. Similar 17 ± 0.2 Ma Ma dykes are found in the Dolpo area further west [Carosi et al., 2010].

The basal MCT was interpreted to be active until ~9 Ma in Lantang [Kohn et al., 2004], an age in good agreement with data from the Everest area. The upper MCT appear to be active until at least 13 Ma suggesting a propagation of the thrusts towards the foreland (south) through time [see also Corrie and Kohn, 2011 and Montomoli et al., 2013 for area further west]. Motions on the MCT2 and MCT1 over lasted partial melting by ~5 Ma in units 2 and 1 respectively. The end of motion on the STD is approximately coeval to the end of motion on the MCT2 but precede by ~4 Myr the end of motion on the MCT1, whilst no other ~E-W normal faults appears to have been activated since. The late fast cooling observed close to MCT1 (LC3 ≤8Ma) is not due to a late thrusting on the MCT but rather from erosion of 10-15 kilometres (~4kb) of the overlying section since ~6 Ma. This implies that the MCT did emerge at least 50 km further south at the front of the Kathmandu klippe prior to 6 Ma. Consequently location of the High Himalayan summits and of the water divide probably shifted from south to north prior to reach their present location since less than 8 Ma ago. Erosion is thus focused on the southern slope of the High Himalayan since less than 8 Ma. Such focused erosion cannot have helped the exhumation of the whole GHS above the MCT and below the STDS.

7.5 Synthesis of the Miocene evolution of the central Himalaya and implications for extrusion models.

We propose in Figure 16 a conceptual model for the Miocene evolution of the Himalaya that follows the points exposed above. This oversimplified model does not take into account all observations that have been published on the Himalaya but focuses on the Miocene evolution of the GHS. The main point of the model is that focussed erosion cannot have been the driving mechanism for exhumation of the GHS and establishment of an elevated relief in the Miocene. At that time, GHS partial melting was enhanced by decompression above the MCT with an erosion and deformation front located at least ~50 km south of the present day exposure of the MCT in Langtang, Nyalam and Dudh Kosi sections (Fig. 16). Many aspects of this model are not new and have been proposed by various authors, since a very long time for some of them [e.g., Lefort, 1975]. In the absence of a global numerical model to back it up, such wedge models have been disregarded over the years by most authors in favour of the Lower channel flow linked with focussed erosion model based on numerical simulation [e.g., Beaumont et al., 2001]. However, the southward propagation of localized thrust zones, the absence of focussed erosion and the diachronism between MCT, STD and partial melting are barely compatible with this model. We thus think that a realistic thermo-mechanical model for the Miocene evolution of the Himalaya still wait to be performed.

8. Conclusions

The data from the Nyalam section presented in this study together with data from the Langtang and Dudh Kosi sections from the literature allows to constrain the age of melting, cooling and deformation of the Greater Himalayan Sequence (GHS) of the central Himalayas. Above the lesser Himalaya we distinguish four zones within the GHS, the lowest one (1) corresponding to the MCT zone and the top of the upper one (4) corresponding to the STD shear zone.

In the GHS, in situ partial melting following the prograde Eohimalyan metamorphism (M1) mostly occurred in units 1b, 2 and 3. Partial melting started in units 2 and 3 around 30 Ma in Nyalam and at ~25 Ma in Lantang and Dudh Kosi sections. Melts rapidly raised in the upper units feeding the leucogranite dykes and plutons of unit 4 and inducing the Neohimalyan metamorphism (M2).

The partial melt zone thinned through time. In Nyalam mignatite last crystallized at ~20 Ma in unit 3, 18 Ma in unit 2 and probably at ~15 Ma in unit 1. The last melts are undeformed dykes dated between ~17.5 and ~15 and Ma in Nyalam and ~18.5 and ~16 Ma in Dudh Kosi – Everest. These dykes crosscut all ductile deformation unless in the STD shear zone.

GHS rocks experienced three phases of fast cooling (FC1, FC2 and FC3).

The first fast cooling phase (FC1) down to temperatures of ~250-350°C occurred partly coevally with the intrusion of the last dykes, between ~19 Ma and 13 Ma in Nyalam, and between ~21 and ~17 Ma in Dudh Kosi – Everest.

The second fast cooling phase (FC2) immediately follows FC1 but is restricted to the upper part of unit 4 below the STD. It is linked with normal motion on the STD system until ~13 Ma that caused fast footwall unroofing down to temperature of ~100°C. Since then there was less than 3km exhumation of the STD footwall.

The STDsz has a more complex geometry than the straight low-angle normal fault, generally depicted in cross-sections. We propose that it follows a flat and ramp (dip ~30°N) geometry with the eastern outcrops (Dzakaa) corresponding to deeper parts than the western one (Nyalam), and that it roots south of the south Tibetan domes. Ductile vertical flattening pervasive in unit 4 ended when deformation localised in the narrow STD shear zone. The upward migration of the end of ductile flattening at a rate of 0.8±0.3 mm/yr lead us to propose that the STDsz initiated prior to ~25 Ma.

σ1 appears to have been constantly horizontal and ~N-S and σ3 horizontal and ~E-W between 18 et 11 Ma in units 1, 2 and 3.

The geochronological ages are compatible with an end of motion on the MCT2 at ~ 13 Ma and MCT1 at ~9 Ma.

The last fast cooling phase (FC3) is restricted to units 1 and 2. This cooling is most likely due to underplating and formation of a mid-crustal duplex in the lesser Himalaya linked to motion on the MBT and MFT since ~10 Ma inducing warping of the MCT and GHS that is also required to explain the presence of UHC klippen ~50 km south of the high chain.

This chronology implies that a) Motions on the MCT2 and MCT1 over lasted partial melting by ~5 Ma in units 2 and 1 respectively; b) end of motion on the STD is approximately coeval to the end of motion on the MCT2 but precede by ~4Myr the end of motion on the MCT1; c) the MCT was emerging at least 50 km south of its present exposure at the time of exhumation of the GHS.

Both the southward propagation of localized thrust zones, the geometry of the STDS, the absence of focussed erosion and the diachronisms between MCT, STD and partial melting are barely compatible with the channel flow model for the Miocene evolution of the Himalaya as proposed by Beaumont et al [2001].

Acknowledgements

We thank Maurine Montagnat (part of Labex OSUG@2020 and ANR10 LABX56) for access to the fabric analyseur and Emmanuelle Boutonnet for help in performing the CPO. We thank the China Tibet Kailash international travel and Earth's Paradise Treks companies for field work logistics in Tibet and Nepal respectively, and INSU SYSTER program for financial support. Remarks from two anonymous reviewers, S. Mukherjee and R. Carosi helped to clarify the paper.

References

Armijo, R., P. Tapponnier, J. L. Mercier, and T. L. Han (1986), Quaternary Extension in Southern Tibet - Field Observations and Tectonic Implications, *Journal of Geophysical Research-Solid Earth and Planets*, *91*, 13803-13872. DOI: 0148-0227.

Baldwin, S. L., and T. R. Ireland (1995), A tale of two eras: Pliocene-Pleistocene unroofing of Cenozoic and late Archean zircons from active metamorphic core complexes, Solomon Sea, Papua New Guinea, *Geology*, *23*, 1023-1026.

Beaumont, C., R. A. Jamieson, M. H. Nguyen, and B. Lee (2001), Himalayan tectonics explained by extrusion of a low-viscosity crustal channel coupled to focused surface denudation, *Nature*, *414*, 738-742. DOI: 0028-0836.

Bollinger, L., J. P. Avouac, O. Beyssac, E. J. Catlos, T. M. Harrison, M. Grove, B. Goffe, and S. Sapkota (2004), Thermal structure and exhumation history of the Lesser Himalaya in central Nepal, *Tectonics*, *23*, TC5015, DOI:5010.1029/2003TC001564. DOI: 0278-7407.

Bollinger, L., P. Henry, and J. P. Avouac (2006), Mountain building in the Nepal Himalaya: Thermal and kinematic model, *Earth and Planetary Science Letters*, *244*, 58-71.

Borghi, A., D. Castelli, B. Lombardo, and D. Visona (2003), Thermal and baric evolution of garnet granulites from the Kharta region of S Tibet, E Himalaya, *European Journal of Mineralogy*, *15*, 401-418. DOI: 0935-1221.

Bosse, V., P. Boulvais, P. Gautier, M. Tiepolo, G. Ruffet, J. L. Devidal, Z. Cherneva, I. Gerdjikov, and J. L. Paquette (2009), Fluid-induced disturbance of the monazite Th-Pb chronometer: in situ dating and element mapping in pegmatites from the Rhodope (Greece, Bulgaria), *Chemecal Geology*, *261*, 286-302.

Boutonnet, E., P. H. Leloup, N. Arnaud, J. L. Paquette, W. J. Davis, and K. Hattori (2012), Synkinematic magmatism, heterogeneous deformation, and progressive strain localization in a strike-slip shear zone. The case of the right-lateral Karakorum fault, *Tectonics*, *31*.

Brun, J.-P., J.-P. Burg, and C. Ming (1985), Strain trajectories above the Main Central Thrust (Himalaya) in southern Tibet, *Nature*, *313*, 388-390.

Budzyn, B., D. E. Harlov, M. L. Williams, and M. J. Jercinovic (2011), Experimental determination of stability relations between monazite, fluorapatite, allanite, and REE-epidote as a function of pressure, temperature, and fluid composition, *Am Mineral,*, *96*, 1547–1567.

Burchfiel, B. C., and L. H. Royden (1985), North-South Extension within the Convergent Himalayan Region, *Geology*, *13*, 679-682. DOI: 0091-7613.

Burchfiel, B. C., C. Zhilang, K. V. Hodges, L. Yuping, L. H. Royden, D. Changrong, and X. Jiene (1992), *The South Tibetan detachment System, Himalayan Orogen: Extension Contemporaneous with and Parallel to Shortening in a Collisional Mountain Belt.*, 269 pp., Geological Society of America

Burg, J. P. (1983), Carte Géologique du Sud tibet, Ministry of Geology/CNRS, Beijing/Paris.

Burg, J. P., M. Brunel, D. Gapais, G. M. Chen, and G. H. Liu (1984), Deformation of

Leucogranites of the Crystalline Main Central Sheet in Southern Tibet (China), *Journal of Structural Geology*, *6*, 535-542. DOI: 0191-8141.

Cardozo, N., and R. W. Allmendinger (2013), Spherical projections with OSXStereonet, *Computers & Geosciences*, *51*, 193 - 205. DOI: DOI:10.1016/j.cageo.2012.07.021.

Carosi, R., B. Lombardo, G. Molli, G. Musumeci, and P. C. Pertusati (1998), The south Tibetan detachment system in the Rongbuk valley, Everest region. Deformation features and geological implications, *Journal of Asian Earth Sciences*, *16*, 299-311. DOI: 1367-9120.

Carosi, R., C. Montomoli, D. Rubatto, and D. Visonà (2010), Late Oligocene high-temperature shear zones in the core of the Higher Himalayan Crystallines (Lower Dolpo, western Nepal), TECTONICS, 29, TC4029, doi:10.1029/2008TC002400.

Carosi, R., C. Montomoli, Daniela Rubatto and D. Visonà (2013), Leucogranite intruding the South Tibetan Detachment in western Nepal: implications for exhumation models in the Himalayas, *Terra Nova, 25*, 478–489.

Carosi.R., C. Montomoli, A. Langone, A. Turina, B. Cesare, S. Iaccarino, L. Fascioli, D. Visonà, A. Ronchi, S. M. Rai (in press), Eocene partial melting recorded in peritectic garnets from kyanite-gneiss, Greater Himalayan Sequence, central Nepal. In: “Tectonics of Himalayas” (Editors: S. Mukherjie, R. Carosi, B. Mukherjie, P.van Der Beck, D. Robinson), *Geol. Soc. London sp. publication*, 412, doi:10.1144/SP412.19

Catlos, E. J., T. M. Harrison, C. E. Manning, M. Grove, S. M. Rai, M. S. Hubbard, and B. N. Upreti (2002), Records of the evolution of the Himalayan orogen from in situ Th-Pb ion microprobe dating of monazite: Eastern Nepal and western Garhwal, *Journal of Asian Earth Sciences*, *20*, 459-479. DOI: 1367-9120.

Cherniak, D. J., E. B. Watson, M. Grove, and T. M. Harrison (2004), Pb difusion in monazite: a combined RBS/SIMS study, *Geochim Cosmochim Acta*, *68*, 829-840.

Coleman, M. E., and K. V. Hodges (1998), Contrasting Oligocene and Miocene thermal histories from the hanging wall and footwall of the South Tibetan detachment in the central Himalaya from Ar-40/Ar-39 thermochronology, Marsyandi Valley, central Nepal, *Tectonics*, *17*, 726-740. DOI: 0278-7407.

Copeland, P., T. M. Harrison, K. V. Hodges, P. Maruéjol, P. Le Fort, and A. Pecher (1991), An early Plioce thermal disturbance of the Main Central Thrust, Central Nepal: implications for Himalayan tectonics, *Journal of Geophysical Research*, *96*, 8475-8500.

Corrie, S.L. and M.J. Kohn (2011), Metamorphic history of the central Himalaya, Annapurna region, Nepal, and implications for tectonic models, *GSA Bulletin*, *123*,1863–1879; doi: 10.1130/B30376.1.

Cottle, J. M., M. J. Jessup, D. L. Newell, M. P. Searle, R. D. Law, and M. S. A. Horstwood (2007), Structural insights into the early stages of exhumation along an orogen-scale detachment: The South Tibetan Detachment system, Dzakaa Chu section, eastern Himalaya, *Journal of Structural Geology*, *29*, 1781-1797. DOI: 0191-8141.

Cottle, J. M., M. P. Searle, M. A. S. Horstwood, and D. J. Waters (2009), Timing of Midcrustal Metamorphism, Melting, and Deformation in the Mount Everest Region of Southern Tibet Revealed by U(-Th)-Pb Geochronology, *The Journal of Geology*, *117*, 643-664.

Cottle, J. M., D. J. Waters, D. Riley, O. Beyssac, and M. J. Jessup (2011), Metamorphic history of the South Tibetan Detachment System, Mt. Everest region, revealed by RSCM thermometry and phase equilibria modelling: , v., no.5, p. , , *Journal of Metamorphic Geology*, *29*, 561-582. DOI: DOI: 10.1111/j.1525-1314.2011.00930.x.

Dasgupta, S., J. Ganguly, and S. Neogi (2004), Inverted metamorphic sequence in the Sikkim Himalayas: crystallization history, P-T gradient and implications, *Journal of Metamorphic Geology*, *22*, 395-412. DOI: 0263-4929.

DeCelles, P. G., G. E. Gehrels, Y. Najman, A. J. Martin, A. Carter, and E. Garzanti (2004), Detrital geochronology and geochemistry of Cretaceous-Early Miocene strata of Nepal: implications for timing and diachroneity of initial Himalayan orogenesis, *Earth and Planetary Science Letters*, *227*, 313-330. DOI: 0012-821X.

DeCelles, P. G., D. M. Robinson, J. Quade, T. P. Ojha, C. N. Garzione, P. Copeland, and B. N. Upreti (2001), Stratigraphy, structure, and tectonic evolution of the Himalayan fold-thrust belt in western Nepal, *Tectonics*, *20*, 487-509. DOI: 0278-7407.

Dèzes, P. J., J. C. Vannay, A. Steck, F. Bussy, and M. Cosca (1999), Synorogenic extension: Quantitative constraints on the age and displacement of the Zanskar shear zone (northwest Himalaya), *Geological Society of America Bulletin*, *111*, 364-374. DOI: 0016-7606.

Didier, A., V. Bosse, P. Boulvais, J. Bouloton, J.-L. Paquette, J.-M. Montel, and J. L. Devidal (2013), Disturbance vs. preservation of U-Th-Pb ages in monazite during fluid-rock interaction: textural, chemical and isotopic in-situ study in microgranites (Velay Dome, France), *Contribution to Mineralogy and Petrology*, *165*, 1051-1072.

Edwards, M. A., W. S. F. Kidd, J. X. Li, Y. J. Yu, and M. Clark (1996), Multi-stage development of the southern Tibet detachment system near Khula Kangri. New data from Gonto La, *Tectonophysics*, *260*, 1-19. DOI: 0040-1951.

Fleck, R. J. (1977), Interpretation of discordant 40Ar/39Ar age-spectra of mesozoic tholeiites from antarctica, *Geochimica et Cosmochimica Acta*, *41*, 15–32.

Frank, W., G. Hoinkes, C. Miller, F. Purtscheller, W. Richter, and M. Thöni (1973), Relation between metamorphism and orogeny in a typical section of the Indian Himalayas, *Tschermaks mineralogische und petrographische Mitteilungen*, *20*, 303–332.

Gapais, D., and B. Barbarin (1986), Quartz fabric transition in a cooling syntectonic granite (hermitage massif, france), *Tectonophysics*, *125*, 357-370. DOI: DOI: 10.1016/0040-1951(86)90171-X.

Gardés, E., O. Jaoul, J.-M. Montel, A. M. Seydoux-Guillaume, and R. Wirth (2006), Pb diffusion in monazite : An experimental study of Pb2++ Th4+ _ 2Nd3+ interdiffusion, *Geochimica et Cosmochimica Acta*, *70*, 2325-2336.

Gébelin, A., A. Mulch, C. Teyssier, M. J. Jessup, R. D. Law, and M. Brunel (2013), The Miocene elevation of Mount Everest, *Geology*, *41*, 799–802.

Getty, S. R., and D. J. Depaolo (1995), Quaternary geochronology using the U-Th- Pb method, *Geochim Cosmochim Acta*, *59*, 3267–3272.

Godin, L., R. R. Parrish, R. L. Brown, and K. V. Hodges (2001), Crustal thickening leading to exhumation of the Himalayan Metamorphic core of central Nepal: Insight from U-Pb Geochronology and Ar-40/Ar-39 Thermochronology, *Tectonics*, *20*, 729-747. DOI: 0278-7407.

Goscombe, B., D. Gray, and M. Hand (2006), Crustal architecture of the Himalayan metamorphic front in eastern Nepal, *Gondwana Research*, *10*, 232-255. DOI: 1342-937X.

Grasemann, B., H. Fritz, and J. C. Vannay (1999), Quantitative kinematic flow analysis from the Main Central Thrust Zone (NW-Himalaya, India): implications for a decelerating strain path and the extrusion of orogenic wedges, *Journal of Structural Geology*, *21*, 837-853. DOI: 0191-8141.

Grujic, D., M. Casey, C. Davidson, L. S. Hollister, R. Kundig, T. Pavlis, and S. Schmid (1996), Ductile extrusion of the Higher Himalayan Crystalline in Bhutan: Evidence from quartz microfabrics, *Tectonophysics*, *260*, 21-43. DOI: 0040-1951.

Guo, Z., and M. Wilson (2012), The Himalayan leucogranites: Constraints on the nature of their crustal source region and geodynamic setting, *Gondwana Research*, *22*, 360–376.

Hames, W. E., and S. A. Bowring (1994), An empirical evaluation of the argon diffusion geometry in muscovite, *Earth and planetary science letter*, *124*, 161-169.

Harlov, D. E., and C. J. Hetherington (2010), Partial high-grade alteration of monazite using alkali-bearing fluids: experiment and nature, *Am Mineral,*, *95*, 1105–1108.

Harlov, D. E., R. Wirth, and C. J. Hetherington (2011), Fluid-mediated partial alteration in monazite: the role of coupled dissolution-reprecipitation in element redistribution and mass transfer, *Contrib Mineral Petrol*, *162*, 329–348.

Harris, N., and J. Massey (1994), Decompression and anatexis of Himalayan metapelites, *13*, 1537–1546. DOI: DOI: 10.1029/94TC01611.

Harris, N. B. W., M. Caddick, J. Kosler, S. Goswami, D. Vance, and A. G. Tindle (2004), The pressure-temperature-time path of migmatites from the Sikkim Himalaya, *Journal of Metamorphic Geology*, *22*, 249-264. DOI: 0263-4929.

Harrison, T. M. (1982), Diffusion of 40Ar in hornblende, *Contributions to Mineralogy and Petrology*, *78*, 324-331.

Harrison, T. M., J. Célérier, A. B. Aikman, J. Hermann, and M. T. Heitzler (2009), Diffusion of 40Ar in muscovite, *Geochimica Et Cosmochimica Acta*, *73*, 1039-1051.

Harrison, T. M., I. Duncan, and I. Mc Dougall (1985), Diffusion of 40Zr in biotite: temperature, pressure and compositional effect, *Geochimica Cosmichimica Acta*, *49*, 2461-2468.

Harrison, T. M., M. Grove, K. D. McKeegan, C. D. Coath, O. M. Lovera, and P. Le Fort (1999), Origin and episodic emplacement of the Manaslu intrusive complex, central Himalaya, *Journal of Petrology*, *40*, 3-19. DOI: 0022-3530.

Harrison, T. M., K. D. Mckeegan, and P. Lefort (1995), Detection of inherited monazite in the Manaslu leucogranite by 208Pb/232Th ion microprobe dating-crystallization age and tectonic implications, *Earth Planet Sci Lett*, *133*, 271–282.

Hauck, M. L., K. D. Nelson, L. D. Brown, W. J. Zhao, and A. R. Ross (1998), Crustal structure of the Himalayan orogen at similar to 90 degrees east longitude from Project INDEPTH deep reflection profiles, *Tectonics*, *17*, 481-500. DOI: 0278-7407.

Hemingway, B., S., R. A. Robie, H. T. Evans, and D. Kerrrick (1991), Heat capacities and entropies of sikkimanite, fibrolite, andalusite, kyanite and quartz in the Al2SiO5 phase diagram, *Am Mineral,*, *76*, 1597-1613.

Hermann, J. and D. Runatto, Relating zircon and monazite domains to garnet growth zones: age and duration of granulite facies metamorphism in the Val Malenco lower crust

(2003), *J. metamorphic Geol., 21*, 833–852. doi:10.1046/j.1525-1314.2003.00484.x

Herman, F., P. Copeland, J. P. Avouac, L. Bollinger, G. Mahéo, P. Le Fort, S. Rai, D. Foster, A. Pêcher, K. Stuwe, and P. Henry (2010), Exhumation, crustal deformation, and thermal structure of the Nepal Himalaya derived from the inversion of thermochronological and thermobarometric data and modeling of the topography, *Journal of Geophysical Research*, *115*. DOI: DOI:10.1029/2008JB006126.

Hetherington, C. J., D. E. Harlov, and B. Budzyn (2010), Experimental metasomatism of monazite and xenotime: mineral stability, REE mobility and fluid composition, *Mineral Petrol*, *99*, 165–184.

Hirn, A., J.-C. Lepine, G. Jobert, M. Sapin, G. Wittlinger, X. Z. Xin, G. E. Yuan, W. X. Jing, T. J. Wen, X. Shao Bai, M. R. Pandey, and J. M. Tater (1984), Crustal structure and variability of the Himalayan border of Tibet, *Nature*, *307*, 23 - 25. DOI: DOI:10.1038/307023a0.

Hodges, K. V., B. C. Burchfiel, L. H. Royden, Z. Chen, and Y. Liu (1993), The metamorphic signature of contemporaneous extension and shortening in the central Himalayan orogen: data from the Nyalam transect, southern Tibet, *Journal of metamorphic geology*, *11*, 721-737.

Hodges, K. V., R. R. Parrish, and M. P. Searle (1996), Tectonic evolution of the central Annapurna Range, Nepalese Himalayas, *Tectonics*, *15*, 1264-1291. DOI: 0278-7407.

Imayama, T., T. Takeshita, K. Yi , D.-L. Cho, K. Kitajima, Y. Tsutsumi, M. Kayama, H. Nishido, T. Okumura, K. Yagi, T. Itaya, Y. Sano (2012), Two-stage partial melting and contrasting cooling history within the Higher Himalayan Crystalline Sequence in the far-eastern Nepal Himalaya,*Lithos, 134-135*, 1–22. doi:10.1016/j.lithos.2011.12.004

Inger, S., and N. B. W. Harris (1992), Tectonothermal evolution of the High Himalayan crystalline sequence, Langtang Valley, northern Nepal, *Journal of Metamorphic Geology*, *10*, 439–452.

Jackson, S. E., N. J. Pearson, W. L. Griffin, and E. A. Belousova (2004), The application of laser ablation-inductively coupled plasma-mass spectrometry to in situ U-Pb zircon geochronology, *Chem Geol*, *211*, 47–69.

Jamieson, R. A., C. Beaumont, M. H. Nguyen, and D. Grujic (2006), Provenance of the Greater Himalayan Sequence and associated rocks: predictions of channel flow models, in *Channel Flow, Ductile Extrusion and Exhumation in Continental Collision Zones*, edited, pp. 165-182.

Jessup, M. J., J. M. Cottle, M. P. Searle, R. D. Law, D. L. Newell, R. J. Tracy, and D. J. Waters (2008), P-T-t-D paths of Everest Series schist, Nepal, *Journal of Metamorphic Geology*, *26*, 717-739. DOI: 0263-4929.

Kali, E., P. H. Leloup, N. Arnaud, G. Mahéo, D. Liu, E. Boutonnet, J. VanderWoerd, L. Xiaohan, J. Liu-Zeng, and L. Haibing (2010), Exhumation history of the deepest central Himalayan rocks (Ama Drime range): key P-T-D-t constraints on orogenic models., *Tectonics*, *29*. DOI: DOI:10.1029/2009TC002551.

Kellett, D. A., D. Grujic, and S. Erdmann (2009), Miocene structural reorganization of the South Tibetan detachment, eastern Himalaya: Implications for continental collision, *Lithosphere*, *1*, 259-281.

Kelsey, D. E., C. Clark, and M. Hand (2008), Thermobarometric modelling of zircon and monazite growth in melt-bearing systems: examples using model metapelitic and metapsammitic granulites, *Journal of Metamorphic Geology*, *26*, 199-212. DOI: 0263-4929.

Kohn, M. J. (2008), P–T–t data from central Nepal support critical taper and repudiate large-scale channel flow of the Greater Himalayan Sequence, *Geol. Soc. Am. Bull.*, *120*, 259–273.

Kohn, M. J., M. S. Wieland, C. D. Parkinson, and B. N. Upreti (2004), Miocene faulting at plate tectonic velocity in the Himalaya of central Nepal, *Earth and Planetary Science Letters*, *228*, 299-310. DOI: 0012-821X.

Kohn, M. J., M. S. Wieland, C. D. Parkinson, and B. N. Upreti (2005), Five generations of monazite in Langtang gneisses: implications for chronology of the Himalayan metamorphic core, *Journal of Metamorphic Geology*, *23*, 399-406. DOI: 0263-4929.

Law, R. D., M. J. Jessup, M. P. Searle, M. K. Francsis, D. J. Waters, and J. M. Cottle (2011), Telescoping of isotherms beneath the South Tibetan Detachment System, Mount Everest Massif, *Journal of Structural Geology*, *33*, 1569-1594.

Law, R. D., M. P. Searle, and R. L. Simpson (2004), Strain, deformation temperatures and vorticity of flow at the top of the Greater Himalayan Slab, Everest Massif, Tibet, *Journal of the Geological Society*, *161*, 305-320. DOI: 0016-7649.

Le Breton, N., and A. Thompson (1988), Fluid-absent (dehydration) melting of biotite in metapelites in the early stages of crustal anatexis., *Contrib Mineral Petrol*, *99*, 226–237.

Lee, J., and M. J. Whitehouse (2006), Onset of mid-crustal extensional flow in southern Tibet: Evidence from U/Pb zircon ages, *geology*, *35*, 45-48. DOI: DOI: 10.1130/G22842A.1.

Leech, M.L., 2008. Does the Karakoram fault interrupt mid-crustal channel flow in the westernHimalaya? Earth Planet. Sci. Lett. 276, 314–322. doi:10.1016/j.epsl.2008.10.006.

Le Fort, P. (1975), Himalaya: the collided range, *Am J Sci*, *275*, 1-44.

Le Fort P., C. Cuney,C. Deniel et al (1987). Crustal generation of the Himalayan Leucogranites, *Tectonophysics*, 134, 39-57.

Leloup, P. H., N. O. Arnaud, G. Mahéo, J. L. Paquette, S. Guillot, F. Valli, H. Li, Z. Xu, R. Lacassin, and P. Tapponnier (2012), Successive deformation episodes along the Lungmu Co zone, west-central Tibet, *Gondwana Research*, *21*, 37–52.

Leloup, P. H., G. Mahéo, N. Arnaud, E. Kali, E. Boutonnet, D. Liu, L. Xiaohan, and L. Haibing (2010), The South Tibet detachment shear zone in the Dinggye area. Time constraints on extrusion models of the Himalayas, *Earth and Planetary Science Letters*, *292*, 1–16.

Liu, X., L. XiaoHan, P. H. Leloup, G. Mahéo, J.-L. Paquette, X. Zhang, and X. Zhou (2012), Ductile deformation within Upper Himalaya Crystalline Sequence and geological implications, in Nyalam area, Southern Tibet, *Chinese Science Bulletin*, *57*, 3469−3481. DOI: DOI: 10.1007/s11434-012-5228-6.

Macfarlane, A. M. (1993), Chronology of Tectonic Events in the Crystalline Core of the Himalaya, Langtang-National-Park, Central Nepal, *Tectonics*, *12*, 1004-1025. DOI: 0278-7407.

Macfarlane, A. M., K. V. Hodges, and D. Lux (1992), A structural analysis of the Main Central Thrust zone, Lantang National Park, central Nepal Himalaya, *Geol. Soc. Am.*

Bull., *104*, 1389-1402.

Macfarlane, C. R. M., and T. M. Harrison (2006), Pb-diffusion in monazite: Constraints from a high-T contact aureole setting, *Earth and Planetary Science Letters*, *250*, 376–384. DOI: DOI: 10.1016/j.epsl.2006.06.050.

Mainprice, D., J. L. Bouchez, P. Blumenfeld, and J. M. Tubia (1986), Dominant c-slip in naturally deformed quartz: implications for dramatic plastic softening at high temperature, *Geology*, *14*, 819-822.

Malavieille, J. (2010), Impact of erosion, sedimentation, and structural heritage on the structure and kinematics of orogenic wedges: Analog models and case studies, *GSA Today*, *20*. DOI: DOI: 10.1130/GSATG48A.1.

Maluski, H., P. Matte, M. Brunel, and X. S. Xiao (1988), Argon-39-Argon-40 Dating of Metamorphic and Plutonic Events in the North and High Himalaya Belts (Southern Tibet - China), *Tectonics*, *7*, 299-326. DOI: 0278-7407.

Mattauer, M. (1986), Intracontinental subduction, crust-mantle decollement and crustal-stacking wedge in the Himalayas and other collision belts, *Geological Society, London, Special Publications*, *19*, 37-50. DOI: DOI: 10.1144/GSL.SP.1986.019.01.02.

Menegon, L., G. Pennacchioni, R. Heilbronner, and L. Pittarello (2008), Evolution of quartz microstructure and c-axis crystallographic preferred orientation within ductilely deformed granitoids (arolla unit, western alps), *Journal of Structural Geology*, *30*, 1332-1347. DOI: DOI:10.1016/j.jsg.2008.07.007.

Montomoli C., S. Iaccarino, R. Carosi , A. Langone, D. Visonà (2013), Tectonometamorphic discontinuities within the Greater Himalayan Sequence in Western Nepal (Central Himalaya): Insights on the exhumation of crystalline rocks, Tectonophysics, 608, 1349–1370

Mukherjee M. H. A. Koyi, and C. J. Talbot (2012), Implications of channel flow analogue models for extrusion of the Higher Himalayan Shear Zone with special reference to the out-of-sequence thrusting, *International Journal of Earth Sciences, 101,* 53-272.

Mukherjee M. and H. A. Koyi (2010a), Higher Himalayan Shear Zone, Sutlej section: structural geology and extrusion mechanism by various combinations of simple shear, pure shear and channel flow in shifting modes, *International Journal of Earth Sciences, 99*, 1267-1303.

Mukherjee M. and H. A. Koyi (2010b), Higher Himalayan Shear Zone, Zanskar Indian Himalaya: microstructural studies and extrusion mechanism by a combination of simple shear and channel flow, *International Journal of Earth Sciences,* 99, p1083-1110.

Mukherjee S. (2013a), Channel flow extrusion model to constrain dynamic viscosity and Prandtl number of the Higher Himalayan Shear Zone, *International Journal of Earth Sciences, 102*, 1811-1835.

Mukherjee S. (2013b), Higher Himalaya in the Bhagirathi section (NW Himalaya, India): its structures, backthrusts and extrusion mechanism by both channel flow and critical taper mechanisms, *International Journal of Earth Sciences, 102,* 1851-1870.

Murphy, M. A., and T. M. Harrison (1999), Relationship between leucogranites and the Qomolangma detachment in the Rongbuk Valley, south Tibet, *Geology*, *27*, 831-834. DOI: 0091-7613.

Myrow, P. M., Hughes N. C., Searle M. P., C.M. Fanning, Peng S.-C., Parcha S. K. (2009), Stratigraphic correlation of Cambrian–Ordovician deposits along the Himalaya: Implications for the age and nature of rocks in the Mount Everest region, *Geological Society of America Bulletin*, *121*, 323-332. DOI: DOI: 10.1130/B26384.1.

Paquette, J.-L., and M. Tiepolo (2007), High resolution (5 microns) U-Th-Pb isotope dating of monazite with excimer laser ablation (ELA)-ICPMS, *Chem Geol*, *240*, 222–237.

Parrish, R. R. (1990), U-Pb Dating of Monazite and Its Application to Geological Problems, *Canadian Journal of Earth Sciences*, *27*, 1431-1450. DOI: 0008-4077.

Passchier, C. W., and R. A. J. Trouw (2005), *Microtectonics*, Springer Verlag. second edition. 366 p.

Pêcher, A. (1991), The Contact between the Higher Himalaya Crystallines and the Tibetan Sedimentary Series - Miocene Large-Scale Dextral Shearing, *Tectonics*, *10*, 587-598.

Peternell, M., P. Hasalova, C. Wilson, S. Piazolo, and K. Schulmann (2010), Evaluating quartz crystallographic preferred orientations and the role of deformation partitioning using EBSD and fabric analyser techniques, *Journal of Structural Geology*, *32*, 803-817.

Pradhananga, U. B., and A. K. Duvadi (2006), A guide book on geological section along Arniko highway (Kathmandu - Kodari road), central Nepal, Government of Nepal, Ministry of Industry commerce and supplies, Depatment of mines and geology, Kathmandu, Nepal.

Renne, P. R., C. C. Swisher, A. L. Deino, D. B. Karner, T. L. Owens, and D. J. DePaolo (1998), Intercalibration of standards, absolute ages and uncertainties in Ar-40/Ar-39 dating, *Chemical Geology*, *145*, 117-152. doi: 0009-2541.

Roberts, M. P., and F. Finger (1997), Do U-Pb zircon ages from granulites reflect peak metamorphic conditions?, *Geology*, *25*, 319-322. DOI: 0091-7613.

Roddick, J. C., R. A. Cliff, and D. C. Rex (1980), The Evolution of Excess Argon in Alpine Biotites - a Ar-40-Ar-39 Analysis, *Earth and Planetary Science Letters*, *48*, 185-208. DOI: 0012-821X.

Rubatto, D., I. S. Williams, and I. S. Buick (2001), Zircon and monazite response to prograde metamorphism in the Reynolds Range, central Australia, *Contributions to Mineralogy and Petrology*, *140*, 458-468. DOI: 0010-7999.

Russell-Head, D. S., and C. J. L. Wilson (2001), Automated fabric analyser system for quartz and ice, *J. Glaciol.*, *10*, 117–130.

Scaillet, B., M. Pichavant, and J. Roux (1995), Experimental crystallization of leucogranite magmas, *J Petrol*, 663–705.

Schaltegger, U., C. M. Fanning, D. Gunther, J. C. Maurin, K. Schulmann, and D. Gebauer (1999), Growth, annealing and recrystallization of zircon and preservation of monazite in high-grade metamorphism: conventional and in-situ U-Pb isotope, cathodoluminescence and microchemical evidence, *Contributions to Mineralogy and Petrology*, *134*, 186-201. DOI: 0010-7999.

Schärer, U. (1984), The Effect of Initial Th-230 Disequilibrium on Young U-Pb Ages - the Makalu Case, Himalaya, *Earth and Planetary Science Letters*, *67*, 191-204. DOI: 0012-821X.

Schärer, U., R. H. Xu, and C. J. Allegre (1986), U-(Th)-Pb systematics and ages of Himalayan leucogranites, South Tibet., *Earth Planet Sci Lett*, *77*, 35–48.

Schelling, D. (1992), The Tectonostratigraphy and Structure of the Eastern Nepal Himalaya, *Tectonics*, *11*, 925-943. DOI: 0278-7407.

Schiotte, L., W. Compston, and D. Bridgwater (1989), Ion Probe U-Th-Pb Zircon Dating of Polymetamorphic Orthogneisses from Northern Labrador, Canada, *Canadian Journal of Earth Sciences*, *26*, 1533-1556. DOI: 0008-4077.

Searle, M. P., and L. Godin (2003), The South Tibetan Detachment and the Manaslu Leucogranite: A structural reinterpretation and restoration of the Annapurna-Manaslu Himalaya, Nepal, *Journal of Geology*, *111*, 505-523. DOI: 0022-1376.

Searle, M. P., R. R. Parrish, K. V. Hodges, A. Hurford, M. W. Ayres, and M. J. Whitehouse (1997), Shisha Pangma leucogranite, south Tibetan Himalaya: Field relations, geochemistry, age, origin, and emplacement, *Journal of Geology*, *105*, 295-317. DOI: 0022-1376.

Searle, M. P., R. D. Law, L. Godin, K. P. Larson, M. J., Streule, J. M. Cottle, and M. J. Jessup (2008), Defining the Himalayan Main Central Thrust in Nepal, *J. Geol. Soc., London*, *165*, 523–534.

Seydoux-Guillaume, A. M., J.-L. Paquette, M. Wiedenbeck, J. M. Montel, and W. Heinrich (2002), Experimental resetting in the U-Th-Pb system in monazite, *Chem Geol*, *191*, 165-181.

Simpson, R. L., R. R. Parrish, M. P. Searle, and D. J. Waters (2000), Two episodes of monazite crystallization during metamorphism and crustal melting in the Everest region of the Nepalese Himalaya, *Geology*, *28*, 403-406. DOI: 0091-7613.

Spear, F. S., and J. M. Pyle (2002), Apatite, monazite and xenotime inmetamorphic rocks, *reviews inmineralogy*, *48*, 293-335.

Stern, R. A., and N. Sanborn (1998), Monazite U-Pb and Th-Ph geochronology by high-resolution secondary ion mass spectrometry, in *Radiogenic Age and Isotopic Studies. Curr Res Geol Surv Canada*, edited, pp. 1–18., Ottawa.

Stipp, M., Stünitz, H., R. Heilbronner, and S. M. Schmid (2002), Dynamic recrystallization of quartz, correlation between natural and experimental conditions, edited by D. De Meer, Drury, M.R., De Bresser, J.H.P., Pennock, G.M., pp. 170-190.

Streule, M. J., M. P. Searle, D. J. Waters, and M. S. A. Horstwood (2010), Metamorphism, melting, and channel flow in the Greater Himalayan Sequence and Makalu leucogranite: Constraints from thermobarometry, metamorphic modeling, and U-Pb geochronology, tectonics, 29, TC5011, doi:10.1029/2009TC002533

Tera, F., and G. J. Wasserburg (1972), U-Th-Pb Systematics in 3 Apollo 14 Basalts and Problem of Initial Pb in Lunar Rocks, *Earth and Planetary Science Letters*, *14*, 281-304. DOI: 0012-821X.

Teufel, S., and W. W. Heinrich (1997), Partial resetting of the U–Pb isotope system in monazite through hydrothermal experiments: an SEM and U–Pb isotope study, *Chem Geol*, *137*, 273–281.

Thompson, A. B. (1982), Dehydration melting of pelitic rocks and the generation of H 2 O-undersaturated granitic liquids, *Am J Sci*, *282*, 1567-1595.

Vannay, J. C., B. Grasemann, M. Rahn, W. Frank, A. Carter, V. Baudraz, and M. Cosca (2004), Miocene to Holocene exhumation of metamorphic crustal wedges in the NW Himalaya: Evidence for tectonic extrusion coupled to fluvial erosion, *Tectonics*, *23*, DOI: 10.1029/2002TC001429 DOI: 0278-7407.

Vannay, J. C., and K. V. Hodges (1996), Tectonometamorphic evolution of the Himalayan metamorphic core between the Annapurna and Dhaulagiri, central Nepal, *Journal of Metamorphic Geology*, *14*, 635-656. DOI: 0263-4929.

Vavra, G., R. Schmid, and D. Gebauer (1999), Internal morphology, habit and U-Th-Pb microanalysis of amphibolite-to-granulite facies zircons: geochronology of the Ivrea Zone (Southern Alps), *Contributions to Mineralogy and Petrology*, *134*, 380-404. DOI: 0010-7999.

Vielzeuf, D., and J. R. Holloway (1988), Experimental-Determination of the Fluid-Absent Melting Relations in the Pelitic System - Consequences for Crustal Differentiation, *Contributions to Mineralogy and Petrology*, *98*, 257-276. DOI: 0010-7999.

Viskupic, K., K. V. Hodges, and S. A. Bowring (2005), Timescales of melt generation and the thermal evolution of the Himalayan metamorphic core, Everest region, eastern Nepal, *Contrib Mineral Petrol*, *149*, 1–21.

Viskupic, K., and K. V. Hodges (2001), Monazite-xenotime thermochronometry: methodology and an example from the nepalese Himalaya, *Contrib. Mineral. Petrol., 141*, 233-247.

Visona, D., and B. Lombardo (2002), Two-mica and tourmaline leucogranites from the Everest-Makalu region (Nepal-Tibet). Himalayan leucogranite genesis by isobaric heating?, *Lithos*, *62*, 125-150. DOI: 0024-4937.

Wang, A., J. I. Garver, G. Wang, J. A. Smith, and K. Zhang (2010), Episodic exhumation of the Greater Himalayan Sequence since the Miocene constrained by fission track thermochronology in Nyalam, central Himalaya, *Tectonophysics 495*, 315–323.

Wang, Y., Q. Li, and G. S. Qu (2006), Ar-40/Ar-39 thermochronological constraints on the cooling and exhumation history of the South Tibetan Detachment System, Nyalam area, southern Tibet, in *Channel Flow, Ductile Extrusion and Exhumation in Continental Collision Zones*, edited by R. D. Law, et al., pp. 327-354, Geological Society of London Special Publication, London.

Wang, Y., J. L. Wan, D. M. Li, Q. Li, and G. S. Qu (2001), Thermochronological evidence of tectonic uplift in Nyalam, South Tibetan Detachment System, *Bulletin of mineralogy, petrology and geochemistry*, *20*, 292-294 (in Chinese with english abstract).

Wang, J . M., J . J . Zhang and X. X. Wang (2013), Structural kinematics, metamorphic P–T profiles and zircon geochronology across the Greater Himalayan Crystalline Complex in south-central Tibet: implication for a revised channel flow, *J. metamorphic Geol., 31,* 607–628

Webb, A. A. G., A. Yin, T. M. Harrison, J. Celerier, and W. P. Burgess (2007), The leading edge of the Greater Himalayan Crystalline complex revealed in the NW Indian Himalaya: Implications for the evolution of the Himalayan orogen, *Geology*, *35*, 955-958. DOI: 0091-7613.

Williams, M. L., M. Jercinovic, D. E. Harlov, B. Budzı`n, and C. J. Hetherington (2011), Resetting monazite ages during fluid-related alteration, *Chem Geol*, *283*, 218–225.

Wobus, C., A. M. Heimsath, K. X. Whipple, and K. V. Hodges (2005), Active out of sequence thrust faulting in the central Nepalese Himalaya, *Nature*, *434*, 1008–1011. DOI: DOI:10.1038/nature03499.

Xu, Z., Q. Wang, A. Pêcher, F. Liang, X. Qi, Z. Cai, H. Li, L. Zeng, and H. Cao (2013), Orogen-parallel ductile extension and extrusion of the Greater Himalaya in the late Oligocene and Miocene, *Tectonics*, *32*, 191–215. DOI: DOI:10.1002/tect.20021.

Yang, X., J. Zhang, G. Qi, D. Wang, L. Guo, P. Li, and J. Li (2009), Structure and deformation around the Gyirong basin, north Himalaya, and onset of the south Tibetan detachment system, *Science in China Series D: Earth Sciences*, *52*, 1046-1058.

York, D. (1969), Least Squares Fitting of a Straight Line with Correlated Errors, *Earth and Planetary Science Letters*, *5*, 320-324. DOI: 0012-821X.

Zhang, J., M. Santosh, X. Wang, L. Guo, X. Yang, and **B.** Zhang (2012), Tectonics of the northern Himalaya since the India–Asia collision, *Gondwana Research*, *21*, 939–960.

Zhang, X., R. Sun, and J. Teng (2007), Study on crustal, lithospheric and asthenospheric thickness beneath the Qinghai-Tibet Plateau and its adjacent areas, *Chinese Science Bulletin*, *52*, 797-804.

Zhu, T. X., G. F. Zou, J. Z. Li, and e. al. (2002), Report of Regional Geological Survey of Nielam County (1/250 000) (in Chinese), Beijing.

Table 1. Sample Locations and Rock types[a]

Unit	General Location	GPS Outcrop	UTM Coordinates (Zone 45R Easting	Northing	Altitude (m)	Sample	lithology	mineralogy	structure	Figure(s)	method(s)	Reference
1	North of ZhangMu	T158	399466	3098636	2546	T11N01	(b) surrounding rock	Q+Pl+Kfs+Bi+Ms+Grt			Ar/Ar	this study
							(a) gashe	Q+Ms	N175, 67 W		Ar/Ar	this study
						T11N03	Fault surface	Q+Bi+Ms	N145 37 NE striation Az N178 dextral / reverse		Ar/Ar	this study
		T162	401252	3103703	2664	T11N05	(b) surronding rock	Q+Pl+Kfs+Ms+Bi+(Grt,Chl)			Ar/Ar	this study
							(a) gashe	Q+Ms	N10, 70 E		Ar/Ar	this study
2	KangShan Bridge	T167	400928	3110679	3532	T11N07	Gashe	Q+Ms	N160, 65W		Ar/Ar	this study
						T11N08	Tourmaline leucogranite	Q+Pl+Kfs+Ms+Tur+(Sil,Bi)	Undeformed dyke trending N05 70W	2d, 3a	U-Th/Pb (Mz) Petrology	this study this study
						T11N09	Metatexite	Q+Pl+Kfs+Bi+Ms+(Grt,Sil)	Foliation trending N70 40 N	3a	U-Th/Pb (Mz) Petrology chemistry	this study this study this study
	Nyalam South	T168	399036	3112850	3725	T11N10	Muscovite bearing leucopegmatite	Q+Pl+Kfs+Ms+(Tur)	Folded sill	3b	U-Th/Pb (Zr) Petrology chemistry	this study this study this study
						T11N11	Two micas leucogranite	Q+Pl+Kfs+Bi+Ms+(Chl)	Undeformed dyke	3b	U-Th/Pb (Mz) Petrology chemistry	this study this study this study
3	Nyalam North	T181	400219	3117086	3779	T11N41	Biotite bearing leucopegmatite	Q+Pl+Kfs+Bi+(Chl,Ms,Sil,Crd)	sill	3c	U-Th/Pb (Mz, Zr) Petrology chemistry	this study this study this study
						T11N42	Two micas leucogranite	Q+Pl+Kfs+Bi+Ms+(Tur,Chl)	Undeformed dyke trending N05 42W	2e, 3c	U-Th/Pb (Mz) Petrology chemistry	this study this study this study
		T182	400142	3117642	3817	T11N44	Leucopegmatite	Q+Pl+Kfs+(Ms,Bi, Grt, Cd)	Melted pocket	3d	U-Th/Pb (Mz) Petrology chemistry	this study this study this study
						T11N45	Biotite granite	Q+Pl+Kfs+Bi+(Ms,Sil,Ky)	Undeformed dyke trending N10 40W	2e, 3c	U-Th/Pb (Mz) Petrology chemistry	this study this study this study
		T183	400352	3118886	3807	T11N47	Biotite leucopegmatite	Q+Kfs+(Ms,Chl)	Undeformed	3e	U-Th/Pb (Mz) Petrology chemistry	this study this study this study
		T185				T11N21	Fault surface	Q+Ms+Chl	N165, 60 N, stiation Pitch 65N		Ar/Ar	this study
4	ZhaXiGang	T188	402857	3126898	4151	T11N56	Tourmaline leucogranite	Q+Pl+Kfs+Ms+Tur+(Bi)	Undeformed	3f	U-Th/Pb (Mz) Petrology chemistry	this study this study this study
		T212	404318	3129661	4094	T11N51	Gashe	Q	N105, 52S		Ar/Ar	this study
	ZhaSongLe Valley	T210	407734	3136869	4232	T11N39	Aplitic two micas leucogranite	Q+Pl+Kfs+Bi+Ms+(Sil)	Undeformed		U-Th/Pb (Mz)	this study
		T209	407970	3137256	4240	T11N37	Biotite leucopegmatite	Q+Pl+Kfs+Bi+Sil+(Ms)	Deformed sill	3j	U-Th/Pb (Mz, Zr) Petrology chemistry	Liu et al. [2012] this study this study
						T11N38	Biotite granite	Q+Pl+Kfs+Bi+(Ms)	Undeformed dyke trending N130 90	3j	U-Th/Pb (Mz)	Liu et al. [2012]
						T11N40	quartz ribbon	Q	Fo N45 47 N	14	quartz CPO	this study
		T213	407481	3137842	4246	T11N53A	garnet gneiss	Q+Pl+Bi+Grt+(Ms)	Fo N47 45 N	14	quartz CPO	this study
		T207	404775	3138142	4305	T11N32	Biotite granite	Q+Pl+Kfs+Bi+(Ms,Chl, Tur)	Deformed sill	3h	U-Th/Pb (Mz) Petrology chemistry	Liu et al. [2012] this study this study
						T11N33	Aplitic two micas leucogranite	Q+Pl+Kfs+Bi+Ms+(Tur)	slightly deformed dyke	3h	U-Th/Pb (Mz) chemistry	this study
						T11N34	Aplitic two micas leucogranite	Q+Pl+Kfs+Bi+Ms+(Tur,Chl)	Undeformed dyke trending N160 90	3g	U-Th/Pb (Mz) Petrology chemistry	this study this study this study
	ZhaSongLe	T206	403211	3138843	4372	T11N29	Tourmaline leucogranite	Q+Pl+Kfs+Ms+Tur+(Grt, And)	Deformed with foliation N40 40N and lineation AZ N50		U-Th/Pb (Mz) Petrology chemistry	this study this study this study
						T11N31	quartz ribbon	Q	Fo N40, 40 li az N50	14	quartz CPO	this study
						T11N30	Tourmaline leucogranite	Q+Pl+Kfs+Tur+(Ms)	Undeformed		U-Th/Pb (Zr) Petrology chemistry	this study this study this study
		T204	403092	3139009	4385	T11N26	mylonite	Q	Fo N42 45 N	14	quartz CPO	this study
						T11N27	mylonite	Q	Fo N 50 45N li p10S	14	quartz CPO	this study
						T11N25	Tourmaline leucogranite	Q+Pl+Kfs+Ms+Tur+(Grt, And)	Deformed dyke		U-Th/Pb (Zr) Petrology chemistry	Liu et al. [2012] this study this study

[a]All samples used in this study are listed. For map location see Figure 2a. For section location see Fig. 1d

Table 2. U-Th/Pb data Summary

GPS site	Samples: Number	Samples: Mineral Type	Population[a]	Age[b] (Ma)	MSWD	Number of spots used in age calculation / total	Spots[c]	Age Type[d]	Interpretation[e]	figure	detailed table
T167	T11N08	Monazite	1	15.8 ± 0.2	0.9	20 / 20	2c. 3b. 4b. 5c. 6c. 7c. 8c. 11c. 12c. 13c. 14c. 15c. 16b. 17c. 18c. 20c. 21b. 22c. 23c. 24b	MM	MC	8b	A1
	T11N09	Monazite	1	17.8 ± 0.1	1.18	21 / 21	1c. 2c. 3b. 4b. 5c. 6c. 7c. 8c. 9b. 10b. 11c. 12c. 15c. 16c. 17b. 18b. 19c. 20b. 21c. 22c. 23c	CM	MC	8a	A2
T168	T11N10	Zircon	1	19.0 ± 0.3	2.0	10 / 20	1b. 2b. 4.1b. 7b. 8b. 9b. 10b. 11b. 13.1b. 14b. 15.1b	LZ	MC	7a	A3
			2	ca. 26		3 / 20	4.2c. 13.2c. 15.2c	MZ	I		
			3	ca. 31		1 / 20	18.2c	MZ	I		
	T11N11	Monazite	1	16.4 ± 0.1	1.7	18 / 20	1c. 2b. 3.2b. 4c. 5c. 6c. 8.2b. 9c. 10c. 11c. 12c. 13c. 15c. 16c. 18.1c. 18.2b. 20b. 21c	MM	MC	8c	A4
			2	ca. 20		2 / 20	7c. 17c	MM	I		
T181	T11N41	Monazite	*1*	20.3 ± 0.3 [19.3 - 21.6]	9.7	19 / 31	3c. 6b. 7b. 8b. 9b. 11b. 12b. 13b. 14.2c. 15b. 16b. 17b. 18b. 19c. 20b. 21.2b. 22b. 23b. 24b	MM	MC	8h	A5
			2	28.8 ± 0.4 [28.1 - 29.5]	2.5	10 / 31	2.1c. 2.2b. 4.1c. 5.1b. 5.2c. 10.1b1. 10.2c. 10.3b2. 14.1b. 21.1c	MM	I		
			3	ca. 26		2 / 31	4.2c. 4.3b2	MM			
		Zircon	1	20.5 ± 0.2	0.6	9 / 23	1.1b. 1.2c. 2b. 3b. 4.1b. 7b. 11.1b. 12.1b1. 13.1b.	LZ	MC	7b	A6
			2	29.2±0.3	1.04	7 / 23	4.3c1. 8c. 9.3c. 10.2c. 11.2c. 12.2cb. 12.3c	LZ	I		
			3	ca. 25.5		3 / 23	5b. 9.2c-b. 13.2c	MZ	I		
	T11N42	Monazite	1	16.5 ± 0.1	1.1	14 / 14	2b. 3b. 6b. 8c. 9b. 10b. 12b.13b. 14c. 15c. 17b. 18b. 21b. 22b	MM	MC	8d	A7
T182	T11N44	Monazite	1	23.4 ± 0.3 [22.4 -24.0]	2.2	21 / 23	1b. 2c. 3b. 4c. 6.1c. 6.2b. 7c. 8.1c. 8.3b. 9c. 10c. 11c. 12b. 13b. 14c. 15b. 16c. 17b. 18c. 19c. 21c	MM	MC	8f	A8
			2	ca. 20		2 / 23	5b. 20c	MM	LR		
	T11N45	Monazite	1	16.8 ± 0.2	1.18	23 / 23	1c. 2c. 3c. 4c. 6c. 8b. 9c. 10c. 11c. 12c. 13c. 14c. 15c. 16c. 17c. 18c. 19c. 20c. 23b. 24c. 25c	MM	MC	8e	A9
T183	T11N47	Monazite	1	22.8 ± 0.2	1.9	15 / 19	2b. 4b. 5b. 6c. 7b. 8b. 9b. 10b. 12c. 14b. 15b. 17.1c. 17.2b. 18c. 19b. 20b. 21c. 22.1c. 22.2b	MM	MC	8g	A10
T188	T11N56	Monazite	1	17.5 ± 0.2	1.6	18 / 21	2c. 3c. 7b. 8c. 9c. 12c. 13.1c. 13.2b. 14.1c. 14.2b. 15c. 16c. 17.1c. 17.2b. 18.1c. 18.2b. 19c. 20b	MM	MC	8l	A11
			2	*ca. 20*		1/21	11c	CM	I		
			3	*ca. 24*		1/21	10c-b	CM	I		
			4	ca. 25		1/21	1c	CM	I		
T209	T11N37	Monazite	1	27.4 ± 0.2	0.52	20/ 25	1.2b. 2.2b. 3c. 4.2b. 5.1c. 5.2b. 6.1c. 6.2b. 7c. 8.1c. 8.2b. 9.1c. 9.2b. 10.1c. 10.2b. 11b. 12b. 13.1c. 13.2b. 15.2b	MM	MC	Liu et al. 2012. Fig. 8e	A21 S3 in Liu et al. . 2012
			2	30.1±0.4	0.21	5 / 25	1.1c. 2.1c. 4.1c. 14.1c. 15.1c	MM	I	Liu et al. 2012. Fig. 8d	
		Zircon	*3*	22.8 ± 0.3	0.07	4 / 15	4b. 5.2b3. 5.4c. 13.1b	LZ	L	7e	A12
			1	26.4 ± 0.3	0.7	10 / 15	1.1b. 6.1b2. 6.2b1. 6.3c. 7b. 8b. 10b. 12.1b. 13.2c. 14b	LZ	MC		
			2	28.4±0.7		1 / 15	1.2c		I		
	T11N38	Monazite	1	17.2 ± 0.2	0.98	17 / 23	2c. 3c. 4c. 5c. 6c. 8b. 9c. 10c. 11c. 14b. 15c. 16c. 17b. 18c. 20c. 21c. 22c	MM	MC	8i	A13
			2	29.4 ± 0.7 [28.6 - 30.2]	3.5	6 / 23	12.1b. 12.2b. 12.3b. 19.1b. 19.2b. 19.3b	MM	I		
T210	T11N39	Monazite	1	15.4 ± 0.2	1	22 / 22	1b. 2b. 3c. 4c. 5c. 6c. 7c. 8c. 9c. 10c. 11c. 12c. 13.2b. 14c. 16b. 17b. 18b. 19c. 20c. 21c. 22b. 23b	MM	MC	8k	A14
T207	T11N32	Monazite	1	22.0 ± 0.3	1.9	16 / 17	1c. 3c. 5cb. 6c. 7c. 8c. 10cb. 11.1b. 12c. 14c. 16.1cb. 17.1cb. 19.1b. 19.2cb. 20c. 17.2c. 16.2c	MM	MC	Liu et al. 2012. Fig. 8c	A20 S2 in Liu et al. . 2012
			2	411±12		1 / 17	7c		I		
	T11N33	Monazite	1	15.6 ± 0.1	0.34	24 / 24	1cb. 2c. 3c. 4c. 5cb. 6c. 7cb. 8cb. 9c. 10cb. 11cb. 12c. 13cb. 14cb. 15cb. 16cb. 17c. 18c. 19cb. 20cb. 21cb. 22c. 23cb. 24c	MM	MC	8n	A15
	T11N34	Monazite	1	15.3 ± 0.1	0.39	23 / 23	1c. 2b. 3c. 4c. 5c. 6c. 7c. 8c. 9c. 10c. 11c. 12c. 13b. 15c. 16c. 17b. 18b. 19b. 20c. 21c. 22c. 23c. 24c	MM	MC	8j	A16
T206	T11N29	Monazite	1	21.9 ± 0.2 [20.4 - 21.8]	2.9	15 /17	1c. 2.1c. 2.2b. 5c. 7b. 9.1c. 9.2b. 10c. 11c. 12.1b. 12.2b. 13c. 14b. 15c. 17c	MM	MC	8m	A17
			2	ca. 31		1 / 17	3b	MM	I		
	T11N30	Zircon	*1*	18.8 ± 0.3	0.46	5 / 15	2b. 5b. 11b. 14b. 15b.	MZ	MC	7c	A18
			2	[425 - 473]		4/15	4.1b. 4.2b. 16.3b3. 16.4c	CZ	I	7d	
				[100-190]		3/15	1.2c. 10b1. 16.2b2	MZ	I		
T204	T11N25	Zircon	1	17.1 ± 0.2	1.4	7 / 10	14b. 18b. 21b. 22b. 26b. 12c. 13c	LZ	MC	Liu et al. 2012 Fig. 8a & b	A19 S1 in Liu et al. . 2012
				> 300		3/10	1b. 7c. 11c		I		

a: Not ploted one Fig. 1 when italicized

b: ^{208}Pb/^{232}Th age for Monazite and ^{206}Pb/^{238}U age for Zircon, age range in brakets when MSWD>2

c : crystal n° and spot location; b. border; c. core

d : MM. Mean ^{208}Pb/^{232}Th age for monazite; CM. Concordia age for monazite; MZ. Mean ^{206}Pb/^{238}U for zircon; LZ. lower Intercept age for zircon

e: MC. melt crytallization; I. inherited; L. Pb loss; LC late recrystallization

Table 3 : Ar/Ar ages

Rock Type	Sample Number	Mineral type	Age/ Plateau age			Inverse Isochron Age			Integrated Age	Table	Figure
			Type	*Age, Ma (±2σ)*	*%^{39}Ar in plateau*	*Age, Ma (±2σ)*	*^{40}Ar/ ^{36}Ar (298.6 in present day atmosphere)*	*MSWD*	*Age, Ma*		
Gashe	**T11N01a**	Muscovite	WPA	**4.8±0.8**	89	4.8±1.3	296±63	0,12	4.9±0.9	A23	11a
Surrounding gneiss	**T11N01b**	Muscovite	WPA	**6.3±0.8**	88	5.6±1.0	322±24	0,45	7.2±1.1	A24	11b
Fault plane	**T11N03**	Biotite	WPA	**10.9±0.4**	78	10.7±0.5	306±18	0,57	11.6±0.8	A25	11c
Gashe	**T11N05a**	Muscovite	WPA	**8.8±0.4**	91	8.9±0.7	292±24	1,03	8.9±0.6	A26	11d
Surrounding gneiss	**T11N05b**	Muscovite	WPA	**17.1±0.7**	100	17.5±3.5	290±92	0,17	16.9±0.8	A27	11e
Gashe	**T11N07**	Muscovite	WPA	**15.2±0.6**	100	15.1±2.7	294±37	0,14	15.2±0.7	A28	11f
Fault plane	**T11N21**	Biotite	WPA	**17.7±0.8**	100	17.3±1.2	327±76	0,05	18.3±1.1	A29	11g
Gashe	**T11N51**	Muscovite	WPA	**8.8±0.3**	86	8.6±0.4	311±22	0,67	9.2±0.7	A30	11h

WPA: weighted plateau age

Figure Captions

Figure 1. The Nyalam cross-section in the frame of the Himalayan belt.

(**a**) Simplified geological frame of the India-Asia continental collision. (**b-c**) Himalayas simplified structural map and cross-section. Modified from Leloup et al. [2010]. (**b**) Simplified structural map of the Himalayan range between 76° and 92°E. Red frame corresponds to Fig. 2a and grey trace to Fig. 1c. Bold letters refer to locations. An upper and a lower MCT have been distinguished. The trace of the main structures are drawn from local studies (from east to west) by Kellett et al. [2009], Dasgupta et al. [2004], Goscombe et al. [2006], Kali et al. [2010], Searle et al. [1997], Searle and Godin [2003], DeCelles et al. [2004], Vannay et al. [2004], and Dèzes et al. [1999]. (**c**) NNE–SSW simplified cross section of the central Himalaya (~86°E). Main geological units as in Fig. 1b, and main structures geometry from Bollinger et al. [2004]. The black line corresponds to the upper relief (i.e., Chomolangma) and the blue line to the lower relief (i.e., Arun valley), no vertical exaggeration. GCT, Great Counter Thrust; GT, Gangdese Thrust; YTS, Yarlung-Tsangpo suture zone. **(d)** Geological cross-section along the Bhote Kosi river and friendship Highway. Drawn from field observations (see text and Fig. 4)**.** A-B-C-D are located on Fig. 2a. Metamorphic zones from Wang et al. [2013]. (**e**) Available ages plotted as a function of the distance from the MCT along the cross-section. Symbols colour / shapes refer to the geochronological / mineral systems and the type of rock. Samples names reported when appearing in the text. U/Pb data from units 2, 3 and 4 are from this study (N standing for T11N samples) unless NY11-1 and TYC-64 from Wang et al. [2013]. Ar/Ar data are from Maluski et al. [1988] (Ti samples), Wang et al. [2006] (N-L samples), and this study (N standing for T11N samples). Zircon fission track data from Wang et al. [2010]. Apatite fission track data from Wang et al. [2001] (NL) and Wang et al. [2010] (T).

Figure 2. Structural frame of the study area, and samples location.

(a) Simplified structural map of the Himalaya in Nyalam area corresponding to the frame in Fig. 1b. Drawn from previous works [Liu et al., 2012; Zhu et al., 2002], satellite image interpretation and fieldwork. Projection is UTM45. Structures at each observation site are reported. **(c-g)** Stereographic projections of main structures. Lower hemisphere Schmidt projection drawn with stereonet software [Cardozo and Allmendinger, 2013]. **(c)** Unit 1 (sites N282, N284, T158 to T161). **(d)** Unit 2 (sites T163, T165 - T170). **(e)** Unit 3 (sites T179 - T186, T211). (**f**) Western part of unit 3 (ZhaXiGang - ZhaSongLe , sites T188 - T189, T197 - T206, T209 - T210). **(g)** Eastern par of unit 4 (Ruji) and Tethyan sedimentary series (sites T190 - T191, T196, T218 - T223).

Figure 3. P-T-t-D paths of the GHS along Nyalam section.

Numbers are timing in Ma. M1 and M2 refer to the Eohimalayan and Neohymalayan metamorphism respectively. Unlabelled thin curves bound aluminium silicates stability fields [Hemingway et al., 1991], labelled curves are (A) the water saturated solidus [Thompson, 1982], (B) Ms + Ab + Qtz = Kfs + As + Melt [Le Breton & Thompson, 1988], (C) Ms + An + Qtz = Kfs + Ab + Melt [Le Breton & Thompson, 1988], (D) Bt + Als + Pl + Qtz = Grt + Kfs + Melt [Le Breton & Thompson, 1988], (E) magmatite cordierite upper pressure stability in peraluminous melts [Vielzeuf et Holloway, 1988]. Grey ellipses are garnet rims P-T estimates (intersection of GARB and GASP thermobarometry) while black arrow is P-T path from the Gibb's method within garnet of sample N23 [Hodges et al., 1993]. The square areas are P-T estimates from Wang et al. [2013]. The bold grey line represent the assumed P-T path, dashed when inferred. FC1, 2 and 3 refer to the three episodes of fast cooling (see Fig. 11 and text for details). (**a, b, c)** Time constrains from Fig. 1e and Fig. 11a. (**d**) Dashed boxes correspond to samples south of Zhangmu that may correspond to another unit, with I and II indicating the inferred P-T paths for the lower and upper units respectively. Time constrains from Fig. 12a (Lantang valley, 100km to the west).

Figure 4. Deformation characters of migmatites and granites along the Nyalam section.

Field pictures with interpretative colour overlays in order to highlight the various rocks generations. For the same figure without overlays see Fig. A32. Crystallization ages are reported (see table 2).

Figure 5. Quartz <C> axis CPOs.

Samples along a cross-section from immediately below the STD (top – site T204) to 3500 m structurally bellow (bottom – site T209) (Fig. 2a). For each sample, one point per pixel stereoplot (lower hemisphere – equal angle) on the left with density colour scale on the right, and corresponding interpretation on the far right (top). Far right (bottom): stereoplot of the orientation of the corresponding sample (Schmidt projection, lower hemisphere). Thin sections pictures with location of the zones investigated, together with crystals maps are shown in appendix A33 to A35.

Figure 6. Zr (left) and Ba (right) contents as a function of the Rb/Sr ratio for the Nyalam granites and migmatites compared with other himalayan Miocene granites.

Figure 7. Examples **of** SEM images of monazites and cathodoluminesence images of zircons showing multiple age populations.

(**a – c**) zircons with ^{206}Pb/^{238}U ages (**d –e**) monazites with ^{208}Pb/^{232}Th ages.

Figure 8. Monazite U-Th/Pb data from Nyalam section.

Corresponding data are summarized in Table 2 and detailed in Table A1-A18. Samples located on Fig. 2a. Age range in parenthesis when MSWD > 2. (**a to m**) ^{206}Pb/^{238}U versus ^{208}Pb/^{232}Th diagrams. White ellipses are not taken into account in the calculations.

Figure 9. Zircon U-Th/Pb data from Nyalam section.
Corresponding data are summarized in Table 2 and detailed in Table A1-A18 and samples located on Fig. 2a (**a to c and e**) Tera – Wasserburg plots (**d**) $^{206}Pb/^{238}U$ versus $^{237}Pb/^{235}U$ (concordia) plot. White ellipses are not taken into account in the calculations.

Figure 11. Ar/Ar dating. Results are summarized in Table 3 and detailed in tables A22 to A30. The age spectra are shown with the steps taken into account for the plateau age calculation designated by a double arrow.

Figure 11. Cooling histories of the GHS along the Nyalam section.
Same data as for Fig. 1e. Data are reported with their nominal closure temperature (see section 3.3). Dashed bold grey lines are the proposed T-t paths. FC stands for fast cooling. **(a)** STD shear zone (upper part of unit 4). Modified from Liu et al. [2012]. **(b)** Unit 2.

Figure 12. Interpretation of the geochronologic data across the GHS.
Distance from MCT1 are only valid for The Nyalam section. Data from other sections are plotted according to their structural positions. The colour symbols correspond to data, with same legend as Fig. 1e. Grey area are interpretations **a)** Lantang section. Data from Kohn et al. [2004] and Macfarlane et al. [1992]. **b)** Nyalam section. See Fig.1e for the data set. **c)** Dudh Kosi –Everest section. Data from Catlos et al., [2002]; Cottle et al., [2009]; Jessup et al., [2008]; Murphy and Harrison, [1999]; Simpson et al., [2000]; Streule et al., [2010]; Viskupic and Hodges, [2001], [2005].

Figure 13. Schematic section of the STDS along a N30 direction.
Section parallel to the motion direction on the STDS. Abbreviations as for Fig. 1b. Dashed bold grey lines indicate the isochrones along which deformation stopped at the same time (IED). The width of the STDsz and of the Yellow band

formation are exaggerated but the dips are respected.

Figure 14. Upward migration of end of deformation below the STD in the ZhaSongLe valley.

Plot of crystalization ages versus the structural distance below the STD. The timing of the end of ductile deformation, bracketed by the ages of the deformed and undeformed dikes, young upward. See text for details.

Figure 15. Constraints on the timing of deformation in the GHS and the STDS plotted along the N30 direction (see Fig. 13). Because dips are not parallel to section and data are projected from as far away as 80 km, the depth beneath the STD is taken as a reference. To insure readability, the vertical scale is magnified 10 times and the dips are not respected. Constraints for deformation timing of each age is given by abbreviations. The iso-age delineates the line along which ductile deformation stopped at a given time.

Figure 16. Oversimplified conceptual model for the Miocene evolution of the Himalaya in between ~85°E and 87°E. Cross-section striking ~N30. Motions on the MCT1 and MCT2 have not been distinguished.

Table Captions

Table 1. Sample Locations and Rock types

Listing of all samples used for all methods

Table 2. U-Th-Pb data Summary

Table 3. Ar-Ar data Summary

Appendixes caption

Table A1-A21

Detailed U/Pb results

Table A22

Geochemistry

Table A23-A30

Detailed Ar/Ar results. Signal values are given in volts along with ages calculated for each step (which error excludes that on J factor on individual steps). $^{40}Ar(r)$ and $^{39}Ar(k)$ respectively shows the percentage of radiogenic argon (corrected from atmospheric input) over the total ^{40}Ar released, and the percentage of ^{39}Ar resulting from ^{39}K transmutation only over the total ^{39}Ar released. Dashed inputs correspond to negative signal value after blanc corrections, which was often the case for ^{37}Ar whose amount was almost null in muscovites.

Appendix A31

Ar/Ar analytical procedure

Figure A32. Field pictures.

Same as Fig. 4 but without interpretative overlays.

Figure A33. T11N26 and T11N27 (site T204) quartz <C> axis CPOs.

Far left: field picture with sample location (Red frame). Left: thin section picture under polarized – analysed light. The red frame corresponds to the zone mapped by the Fabric analyzer. Center: quartz <C> axis orientation map (6.8 μm spatial step) with associated orientation colour wheel. Right: one point per pixel stereographic projection (lower hemisphere – equal angle) with density contours and colour scale for density. Far right: interpretation.

Figure A34 To A36. T11N31 and T11N53A and T11N40 quartz <C> axis CPOs.

Left: thin section picture under polarized – analysed light. The red frame corresponds to the zone mapped by the Fabric analyzer. Center: quartz <C> axis orientation map (6.8 μm spatial step) with associated orientation colour wheel. Right: one point per pixel stereographic projection (lower hemisphere – equal angle) with density contours and colour scale for density. Far right: interpretation

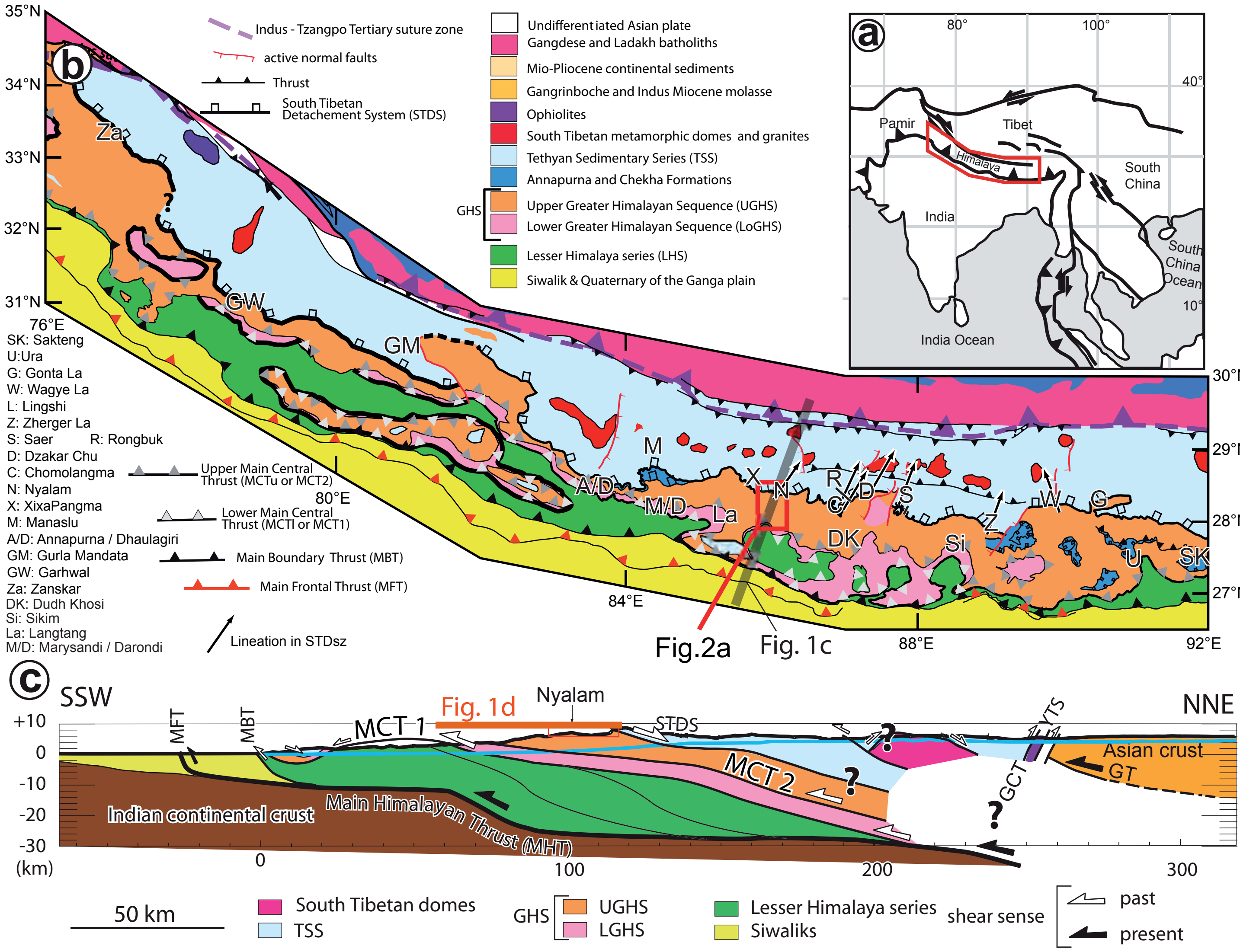

b
a
c
35°N
34°N
33°N
32°N
31°N
30°N
29°N
28°N
27°N
76°E
80°E
84°E
88°E
92°E
Indus - Tzangpo Tertiary suture zone
active normal faults
Thrust
South Tibetan Detachement System (STDS)
Undifferentiated Asian plate
Gangdese and Ladakh batholiths
Mio-Pliocene continental sediments
Gangrinboche and Indus Miocene molasse
Ophiolites
South Tibetan metamorphic domes and granites
Tethyan Sedimentary Series (TSS)
Annapurna and Chekha Formations
GHS
Upper Greater Himalayan Sequence (UGHS)
Lower Greater Himalayan Sequence (LoGHS)
Lesser Himalaya series (LHS)
Siwalik & Quaternary of the Ganga plain
80°
100°
40°
10°
Pamir
Tibet
Himalaya
South China
India
South China Ocean
India Ocean
SK: Sakteng
U: Ura
G: Gonta La
W: Wagye La
L: Lingshi
Z: Zherger La
S: Saer
R: Rongbuk
D: Dzakar Chu
C: Chomolangma
N: Nyalam
X: XixaPangma
M: Manaslu
A/D: Annapurna / Dhaulagiri
GM: Gurla Mandata
GW: Garhwal
Za: Zanskar
DK: Dudh Khosi
Si: Sikim
La: Langtang
M/D: Marysandi / Darondi
Upper Main Central Thrust (MCTu or MCT2)
Lower Main Central Thrust (MCTl or MCT1)
Main Boundary Thrust (MBT)
Main Frontal Thrust (MFT)
Lineation in STDsz
Za
GW
GM
M
A/D
M/D
La
X
N
R
C
D
S
DK
Si
Z
W
G
U
SK
Fig.2a
Fig. 1c
SSW
NNE
Fig. 1d
Nyalam
MFT
MBT
MCT 1
STDS
YTS
GCT
MCT 2
Asian crust
GT
Indian continental crust
Main Himalayan Thrust (MHT)
+10
0
-10
-20
-30
(km)
0
100
200
300
50 km
South Tibetan domes
TSS
GHS
UGHS
LGHS
Lesser Himalaya series
Siwaliks
shear sense
past
present

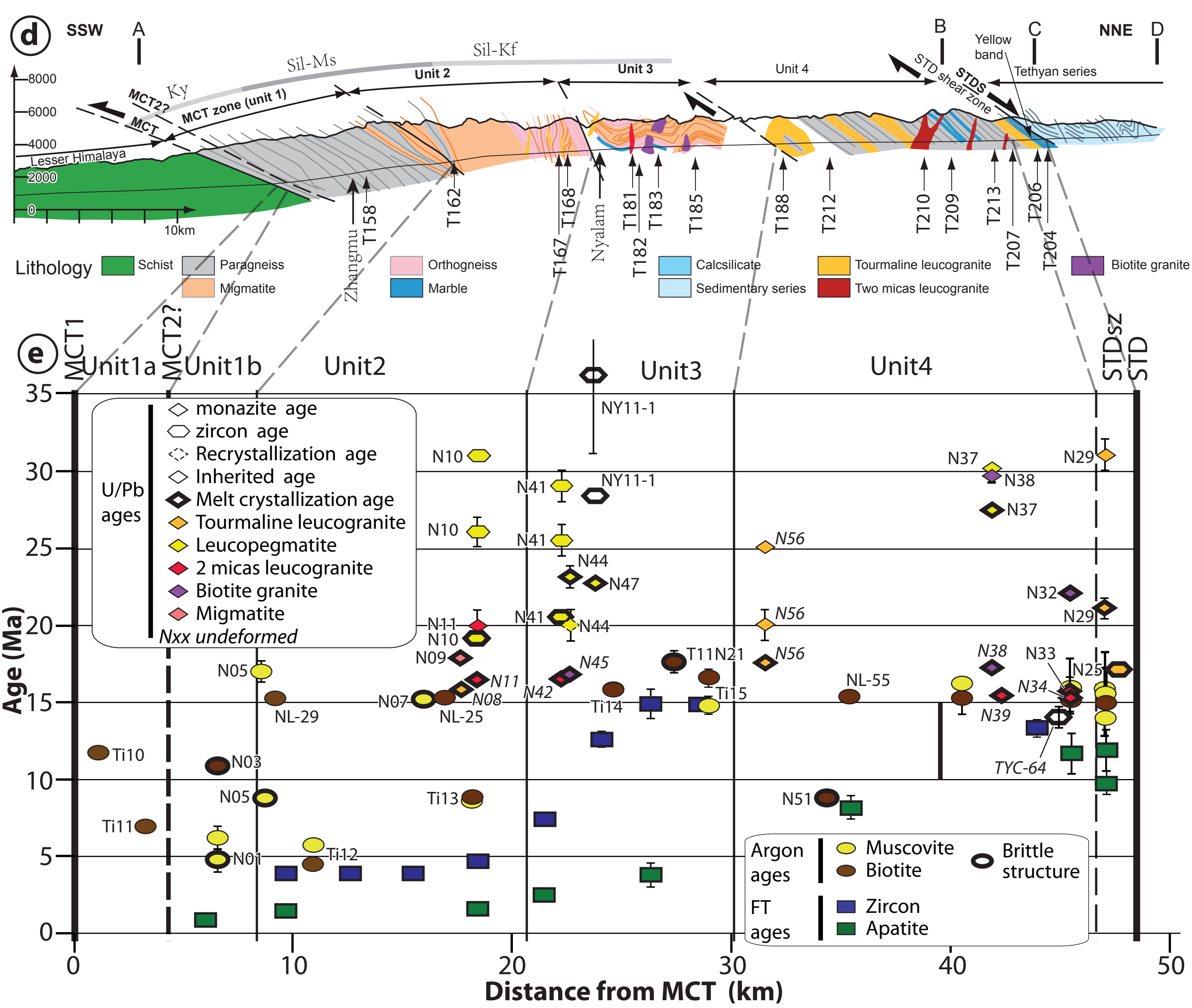
d
SSW
A
B
C
NNE
D
Sil-Ms
Sil-Kf
Ky
MCT2?
MCT
MCT zone (unit 1)
Unit 2
Unit 3
Unit 4
Lesser Himalaya
Yellow band
STD shear zone
STDS
Tethyan series
8000
6000
4000
2000
0
10km
Zhangmu
T158
T162
T167
T168
Nyalam
T181
T182
T183
T185
T188
T212
T210
T209
T213
T207
T206
T204
Lithology
Schist
Paragneiss
Migmatite
Orthogneiss
Marble
Calcsilicate
Sedimentary series
Tourmaline leucogranite
Two micas leucogranite
Biotite granite
e
MCT1
Unit1a
MCT2?
Unit1b
Unit2
Unit3
Unit4
STDsz
STD
U/Pb ages
monazite age
zircon age
Recrystallization age
Inherited age
Melt crystallization age
Tourmaline leucogranite
Leucopegmatite
2 micas leucogranite
Biotite granite
Migmatite
Nxx undeformed
Argon ages
Muscovite
Biotite
FT ages
Zircon
Apatite
Brittle structure
Age (Ma)
Distance from MCT (km)
NY11-1
N10
N41
N37
N38
N29
N44
N47
N56
N32
N11
N09
N45
N42
N08
N07
NL-25
NL-29
N05
Ti14
Ti15
T11N21
NL-55
N33
N34
N39
N25
TYC-64
Ti10
N03
Ti13
N51
Ti11
N01
Ti12

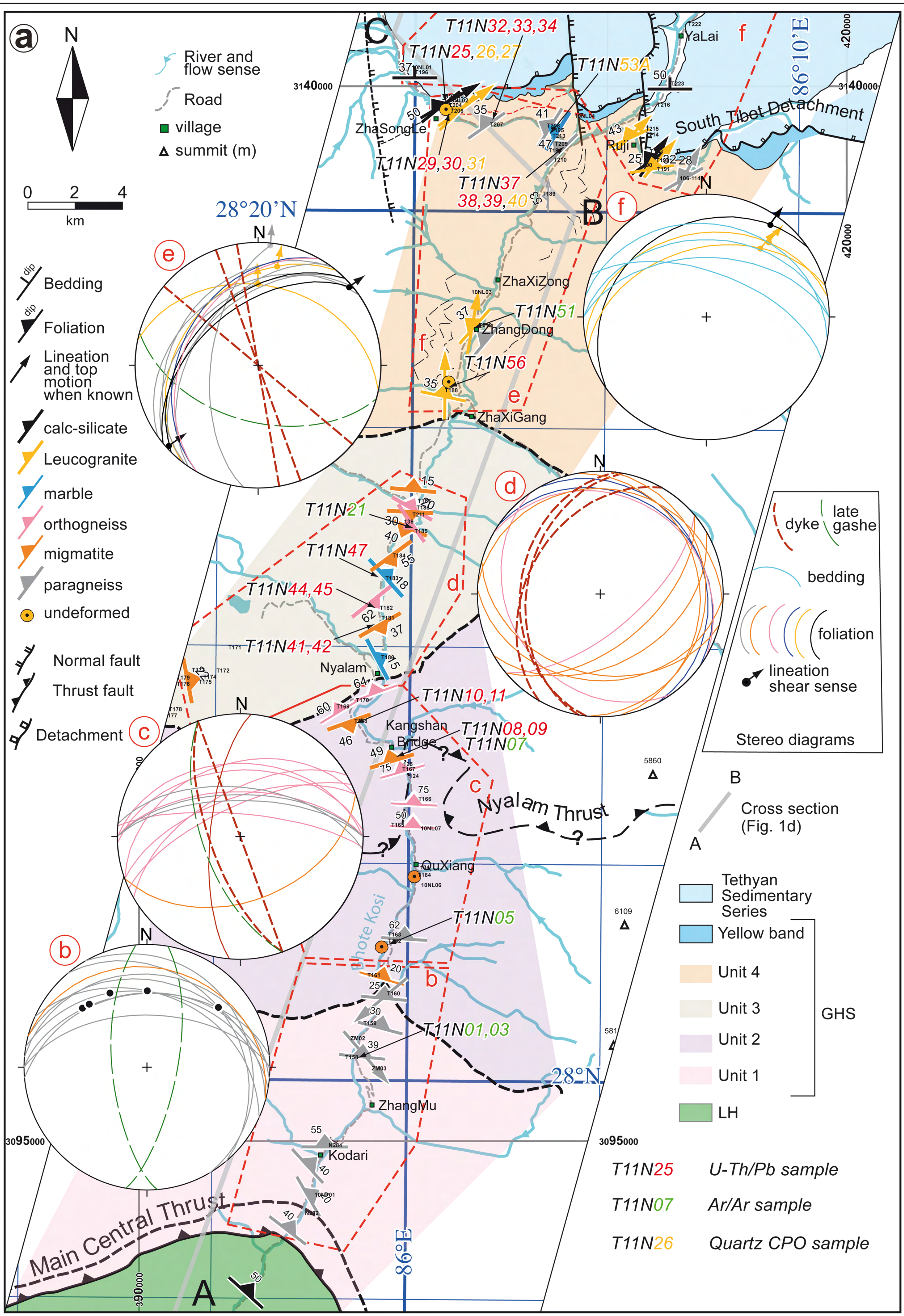
a
N
River and flow sense
Road
village
summit (m)
0 2 4
km
28°20'N
Bedding
Foliation
Lineation and top motion when known
calc-silicate
Leucogranite
marble
orthogneiss
migmatite
paragneiss
undeformed
Normal fault
Thrust fault
Detachment
T11N32,33,34
T11N25,26,27
T11N53A
T11N29,30,31
T11N37
38,39,40
ZhaSongLe
YaLai
Ruji
South Tibet Detachment
86°10'E
ZhaXiZong
ZhangDong
T11N51
T11N56
ZhaXiGang
T11N21
T11N47
T11N44,45
T11N41,42
Nyalam
T11N10,11
Kangshan Bridge
T11N08,09
T11N07
Nyalam Thrust
QuXiang
Bhote Kosi
T11N05
T11N01,03
ZhangMu
Kodari
28°N
86°E
Main Central Thrust
dyke
late gashe
bedding
foliation
lineation shear sense
Stereo diagrams
Cross section (Fig. 1d)
Tethyan Sedimentary Series
Yellow band
Unit 4
Unit 3
Unit 2
Unit 1
GHS
LH
T11N25 U-Th/Pb sample
T11N07 Ar/Ar sample
T11N26 Quartz CPO sample

Fig. 2

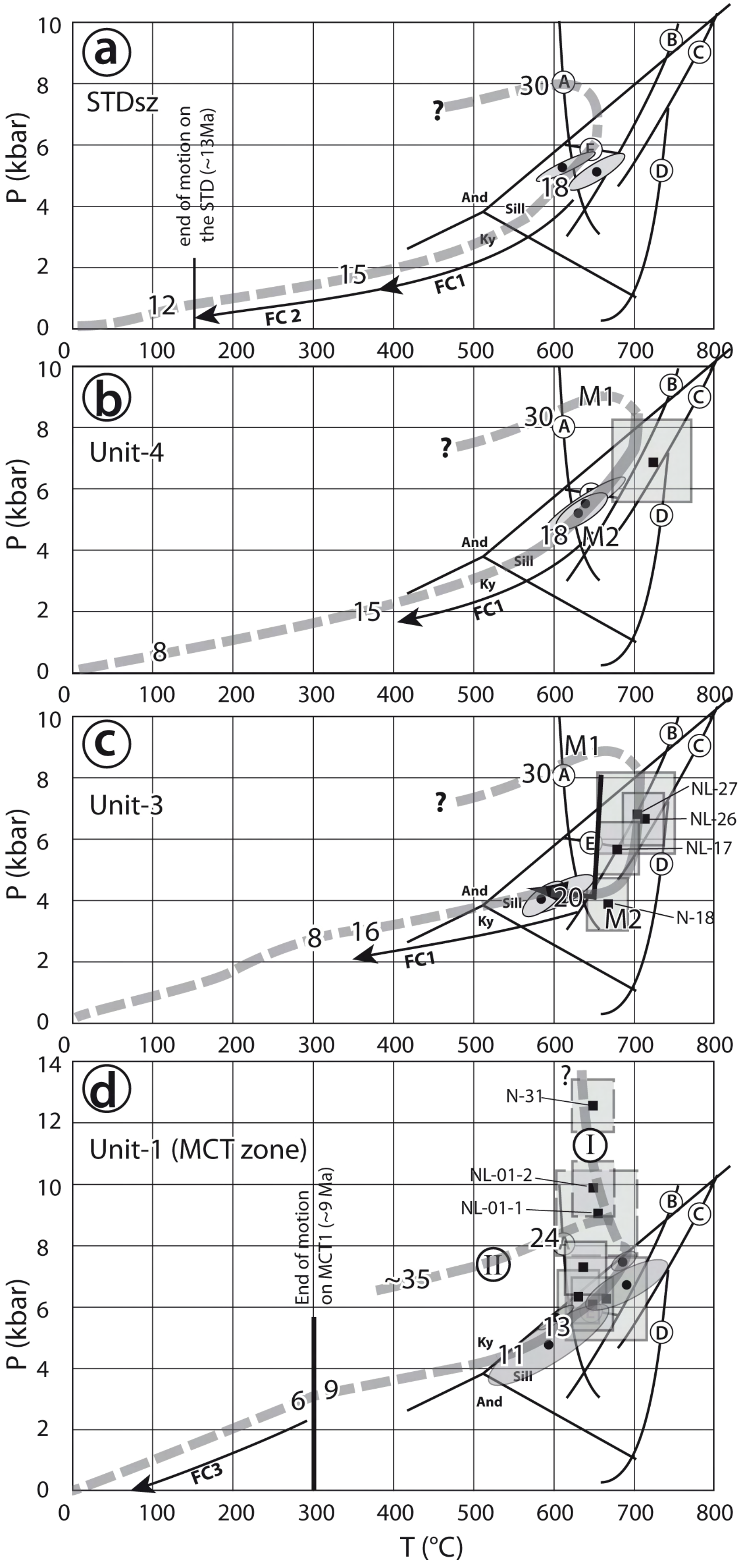
a
STDsz
end of motion on the STD (~13Ma)
b
Unit-4
M1
M2
c
Unit-3
NL-27
NL-26
NL-17
N-18
d
Unit-1 (MCT zone)
End of motion on MCT1 (~9 Ma)
N-31
NL-01-2
NL-01-1
FC1
FC 2
FC3
And
Sill
Ky
P (kbar)
T (°C)

Fig. 3

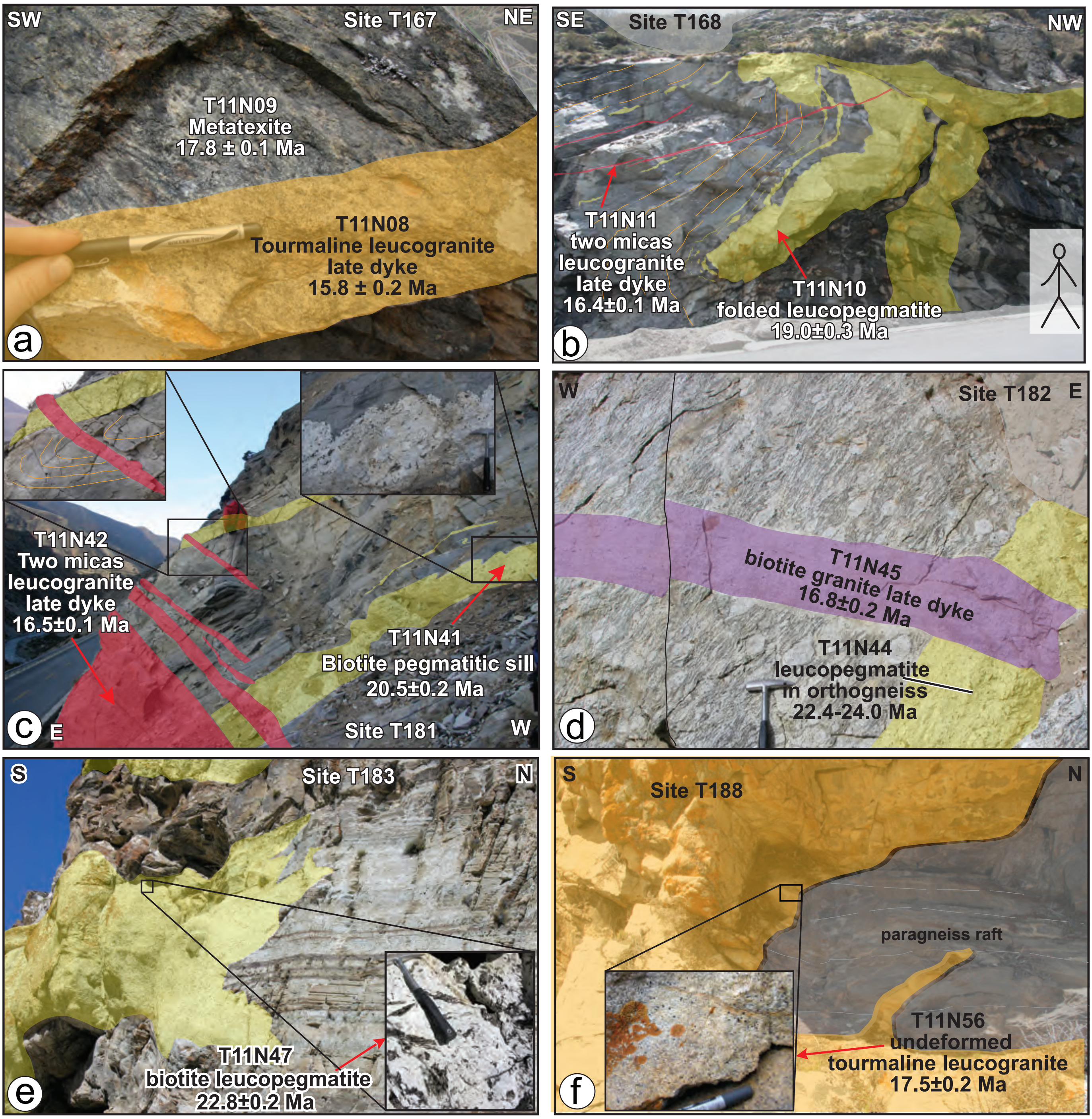
SW
Site T167
NE
T11N09
Metatexite
17.8 ± 0.1 Ma
T11N08
Tourmaline leucogranite
late dyke
15.8 ± 0.2 Ma
a
SE
Site T168
NW
T11N11
two micas
leucogranite
late dyke
16.4±0.1 Ma
T11N10
folded leucopegmatite
19.0±0.3 Ma
b
T11N42
Two micas
leucogranite
late dyke
16.5±0.1 Ma
T11N41
Biotite pegmatitic sill
20.5±0.2 Ma
c
E
Site T181
W
W
Site T182
E
T11N45
biotite granite late dyke
16.8±0.2 Ma
T11N44
leucopegmatite
in orthogneiss
22.4-24.0 Ma
d
S
Site T183
N
T11N47
biotite leucopegmatite
22.8±0.2 Ma
e
S
Site T188
N
paragneiss raft
T11N56
undeformed
tourmaline leucogranite
17.5±0.2 Ma
f

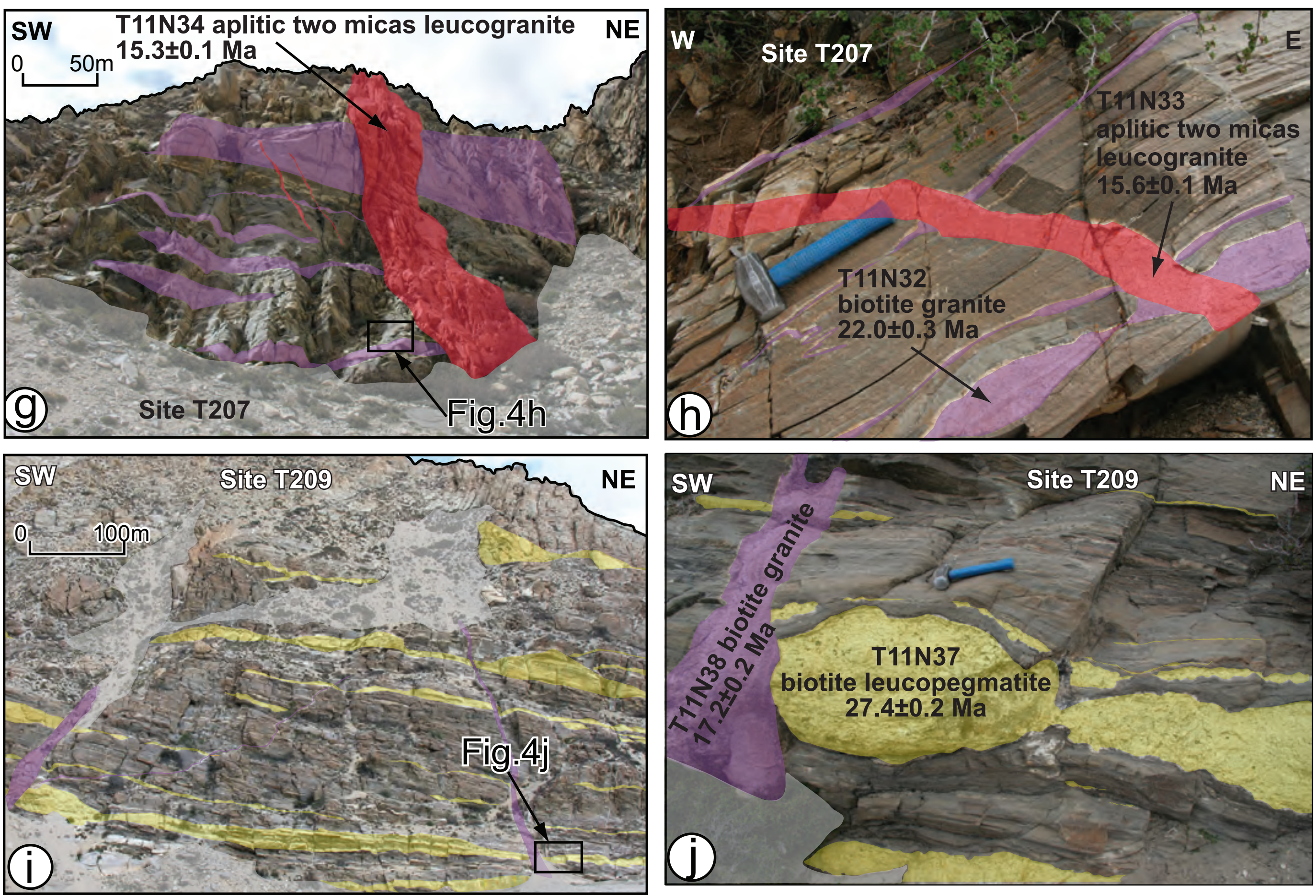
SW
T11N34 aplitic two micas leucogranite
15.3±0.1 Ma
NE
0 50m
Site T207
Fig.4h
g
W
Site T207
E
T11N33
aplitic two micas
leucogranite
15.6±0.1 Ma
T11N32
biotite granite
22.0±0.3 Ma
h
SW
Site T209
NE
0 100m
Fig.4j
i
SW
Site T209
NE
T11N38 biotite granite
17.2±0.2 Ma
T11N37
biotite leucopegmatite
27.4±0.2 Ma
j

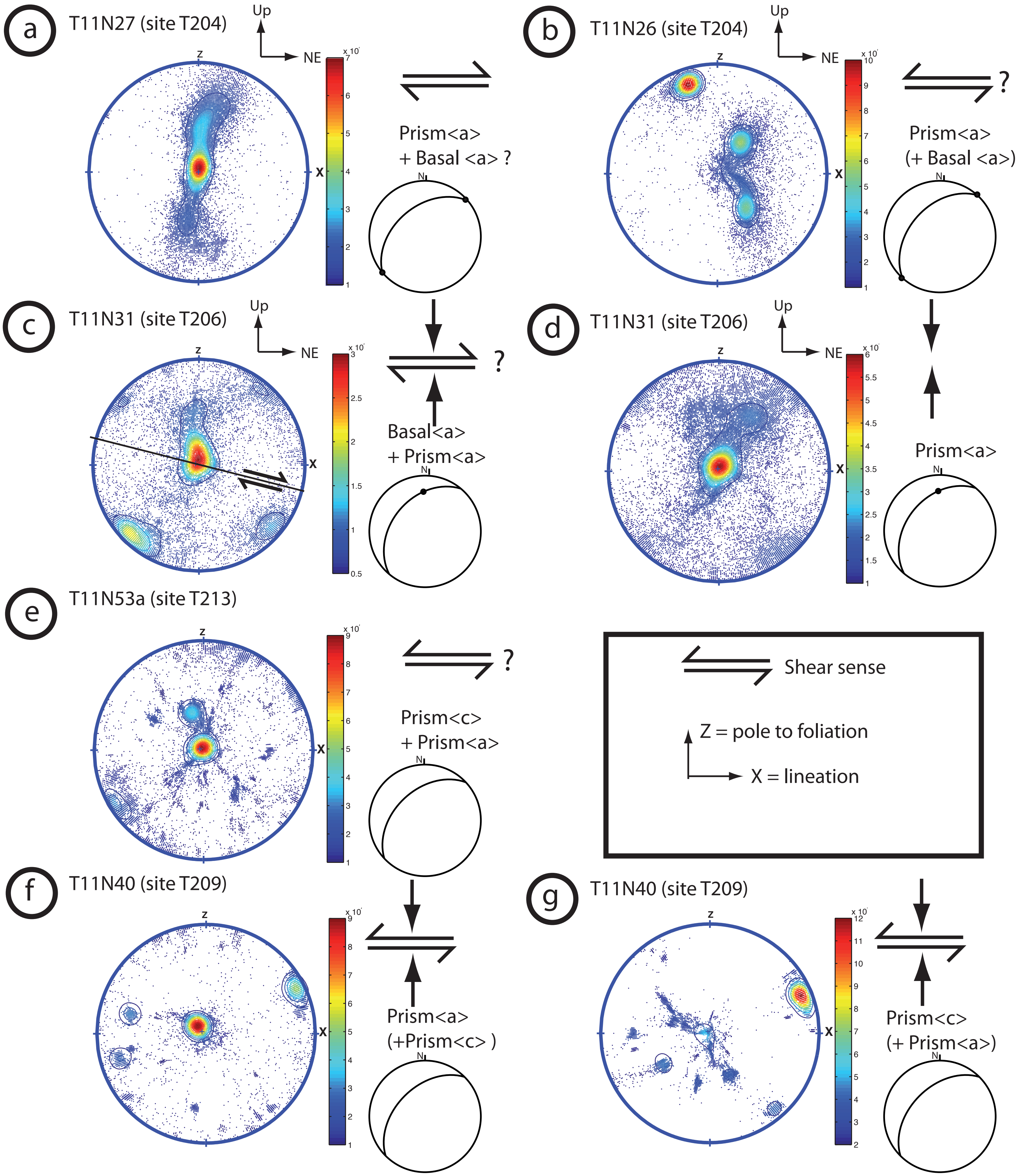
a
T11N27 (site T204)
Up
NE
Prism<a>
+ Basal <a> ?
b
T11N26 (site T204)
Prism<a>
(+ Basal <a>)
c
T11N31 (site T206)
Basal<a>
+ Prism<a>
d
T11N31 (site T206)
Prism<a>
e
T11N53a (site T213)
Prism<c>
+ Prism<a>
Shear sense
Z = pole to foliation
X = lineation
f
T11N40 (site T209)
Prism<a>
(+Prism<c>)
g
T11N40 (site T209)
Prism<c>
(+ Prism<a>)

Figure 5

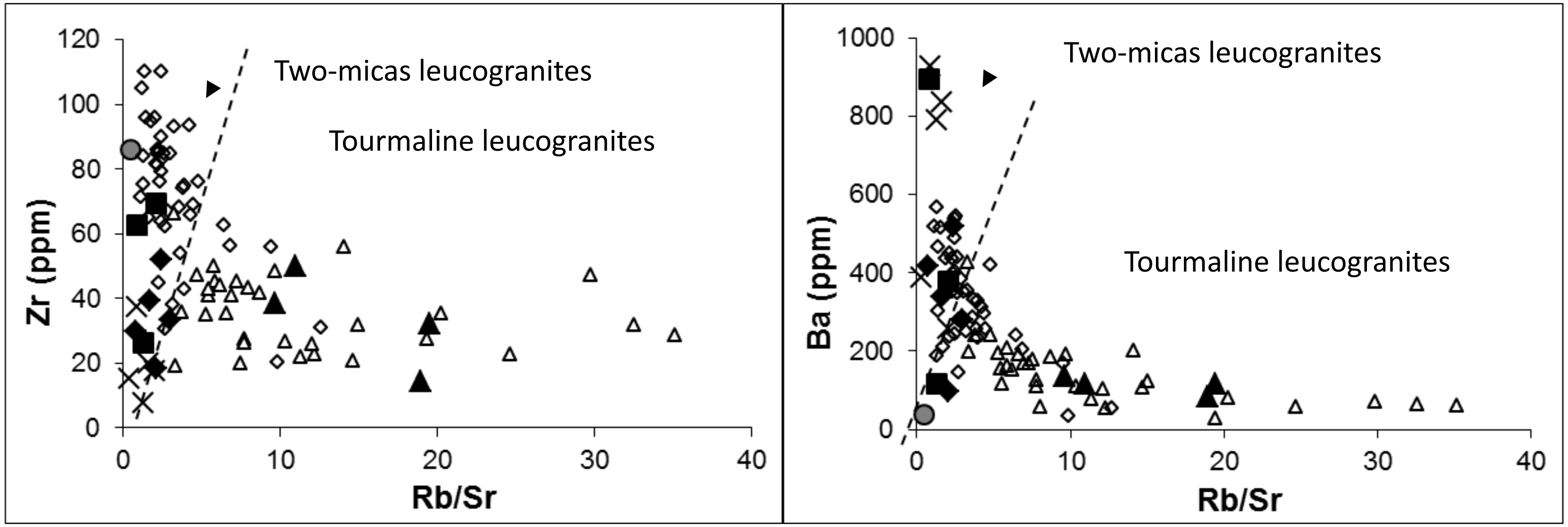

This study
- two-micas leucogranite
- biotite leucogranite
- tourmaline leucogranite
- leucopegmatite
- migmatite

Visona & Lombardo (2002); Guo & Wilson (2012)
- two-micas leucogranite
- tourmaline leucogranite

Figure 6

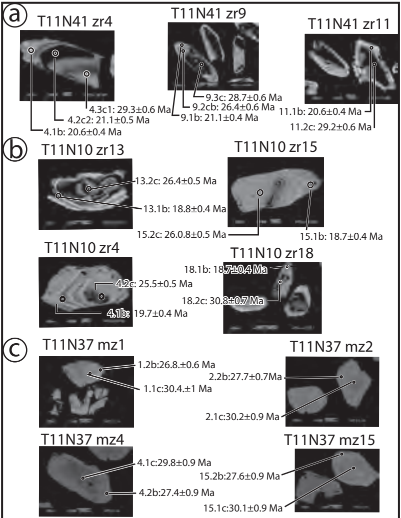
a
T11N41 zr4
4.3c1: 29.3±0.6 Ma
4.2c2: 21.1±0.5 Ma
4.1b: 20.6±0.4 Ma
T11N41 zr9
9.3c: 28.7±0.6 Ma
9.2cb: 26.4±0.6 Ma
9.1b: 21.1±0.4 Ma
T11N41 zr11
11.1b: 20.6±0.4 Ma
11.2c: 29.2±0.6 Ma
b
T11N10 zr13
13.2c: 26.4±0.5 Ma
13.1b: 18.8±0.4 Ma
T11N10 zr15
15.2c: 26.0.8±0.5 Ma
15.1b: 18.7±0.4 Ma
T11N10 zr4
4.2c: 25.5±0.5 Ma
4.1b: 19.7±0.4 Ma
T11N10 zr18
18.1b: 18.7±0.4 Ma
18.2c: 30.8±0.7 Ma
c
T11N37 mz1
1.2b:26.8.±0.6 Ma
1.1c:30.4.±1 Ma
T11N37 mz2
2.2b:27.7±0.7Ma
2.1c:30.2±0.9 Ma
T11N37 mz4
4.1c:29.8±0.9 Ma
4.2b:27.4±0.9 Ma
T11N37 mz15
15.2b:27.6±0.9 Ma
15.1c:30.1±0.9 Ma
d
T11N37 zr13
13.2c: 26.7±0.6 Ma
13.1b: 23.0±0.5 Ma
e
T11N41 mz21
21.1c:28.8±0.6 Ma
21.2b:19.4±0.5 Ma

Fig. 7

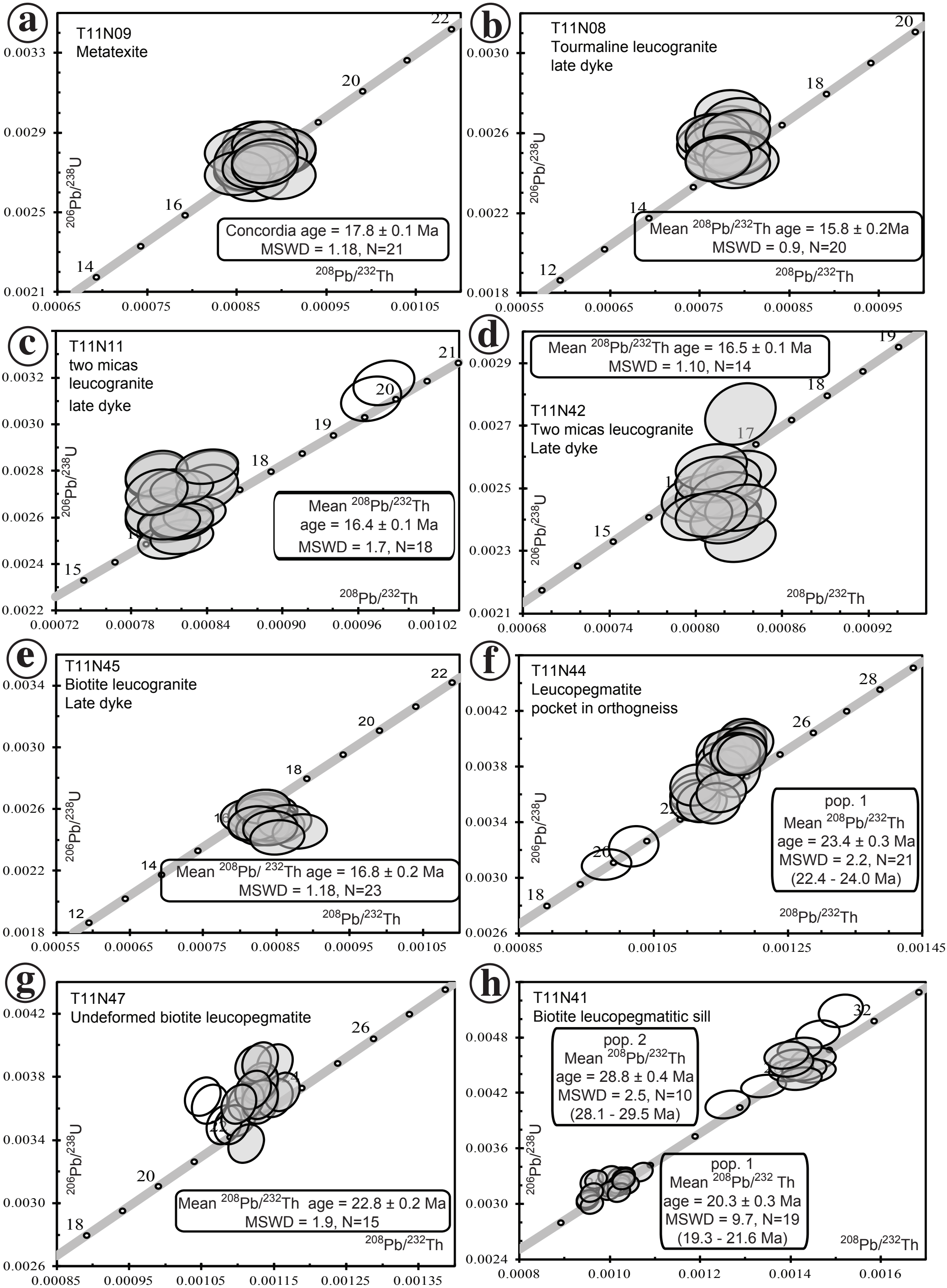

a
T11N09
Metatexite
Concordia age = 17.8 ± 0.1 Ma
MSWD = 1.18, N=21
b
T11N08
Tourmaline leucogranite
late dyke
Mean $^{208}Pb/^{232}Th$ age = 15.8 ± 0.2Ma
MSWD = 0.9, N=20
c
T11N11
two micas
leucogranite
late dyke
Mean $^{208}Pb/^{232}Th$
age = 16.4 ± 0.1 Ma
MSWD = 1.7, N=18
d
Mean $^{208}Pb/^{232}Th$ age = 16.5 ± 0.1 Ma
MSWD = 1.10, N=14
T11N42
Two micas leucogranite
Late dyke
e
T11N45
Biotite leucogranite
Late dyke
Mean $^{208}Pb/^{232}Th$ age = 16.8 ± 0.2 Ma
MSWD = 1.18, N=23
f
T11N44
Leucopegmatite
pocket in orthogneiss
pop. 1
Mean $^{208}Pb/^{232}Th$
age = 23.4 ± 0.3 Ma
MSWD = 2.2, N=21
(22.4 - 24.0 Ma)
g
T11N47
Undeformed biotite leucopegmatite
Mean $^{208}Pb/^{232}Th$ age = 22.8 ± 0.2 Ma
MSWD = 1.9, N=15
h
T11N41
Biotite leucopegmatitic sill
pop. 2
Mean $^{208}Pb/^{232}Th$
age = 28.8 ± 0.4 Ma
MSWD = 2.5, N=10
(28.1 - 29.5 Ma)
pop. 1
Mean $^{208}Pb/^{232}Th$
age = 20.3 ± 0.3 Ma
MSWD = 9.7, N=19
(19.3 - 21.6 Ma)
$^{206}Pb/^{238}U$
$^{208}Pb/^{232}Th$

Fig. 8

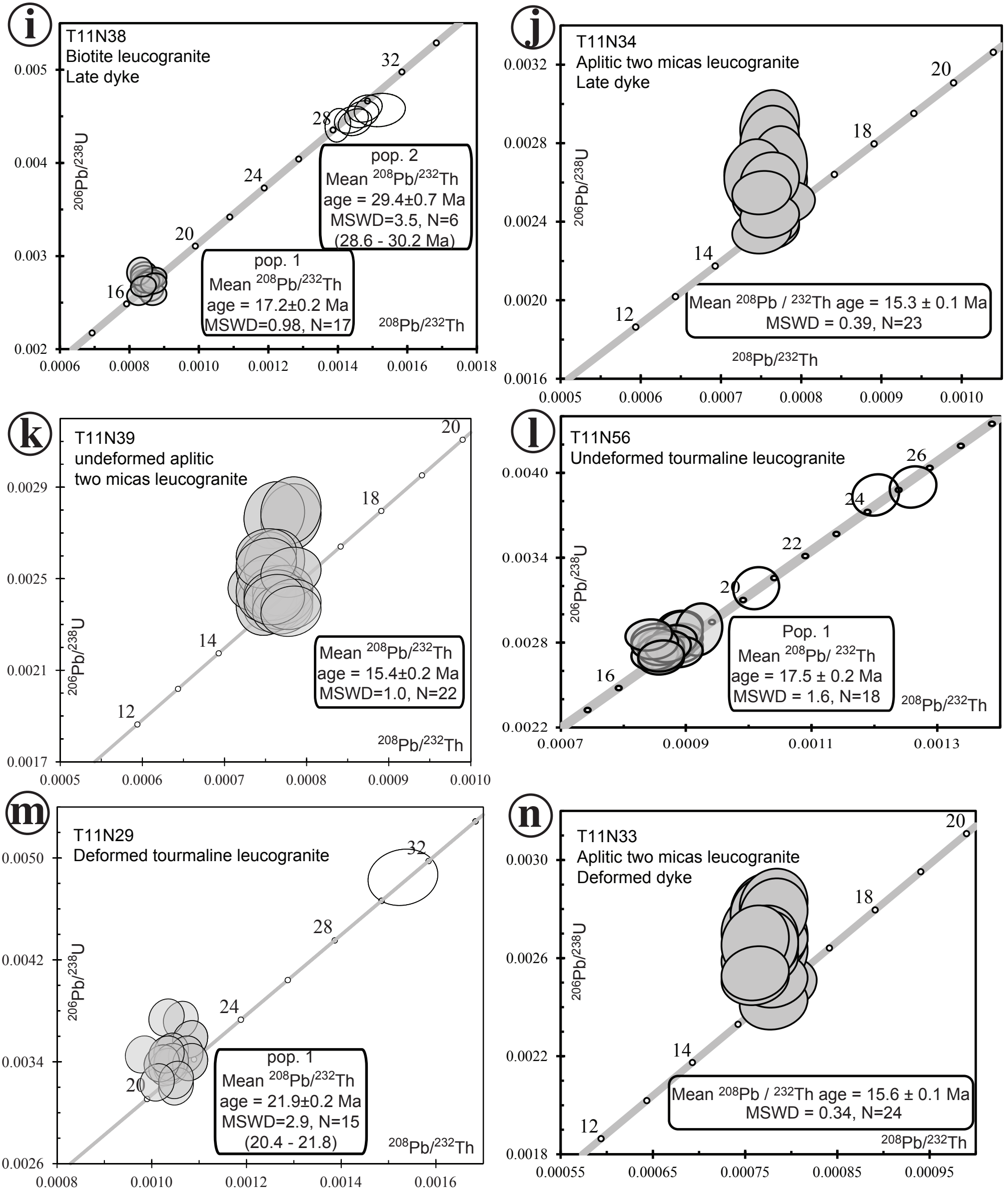
i
T11N38
Biotite leucogranite
Late dyke
pop. 2
Mean 208Pb/232Th
age = 29.4±0.7 Ma
MSWD=3.5, N=6
(28.6 - 30.2 Ma)
pop. 1
Mean 208Pb/232Th
age = 17.2±0.2 Ma
MSWD=0.98, N=17
206Pb/238U
208Pb/232Th
j
T11N34
Aplitic two micas leucogranite
Late dyke
Mean 208Pb / 232Th age = 15.3 ± 0.1 Ma
MSWD = 0.39, N=23
206Pb/238U
208Pb/232Th
k
T11N39
undeformed aplitic
two micas leucogranite
Mean 208Pb/232Th
age = 15.4±0.2 Ma
MSWD=1.0, N=22
206Pb/238U
208Pb/232Th
l
T11N56
Undeformed tourmaline leucogranite
Pop. 1
Mean 208Pb/ 232Th
age = 17.5 ± 0.2 Ma
MSWD = 1.6, N=18
206Pb/238U
208Pb/232Th
m
T11N29
Deformed tourmaline leucogranite
pop. 1
Mean 208Pb/232Th
age = 21.9±0.2 Ma
MSWD=2.9, N=15
(20.4 - 21.8)
206Pb/238U
208Pb/232Th
n
T11N33
Aplitic two micas leucogranite
Deformed dyke
Mean 208Pb / 232Th age = 15.6 ± 0.1 Ma
MSWD = 0.34, N=24
206Pb/238U
208Pb/232Th

Fig. 8

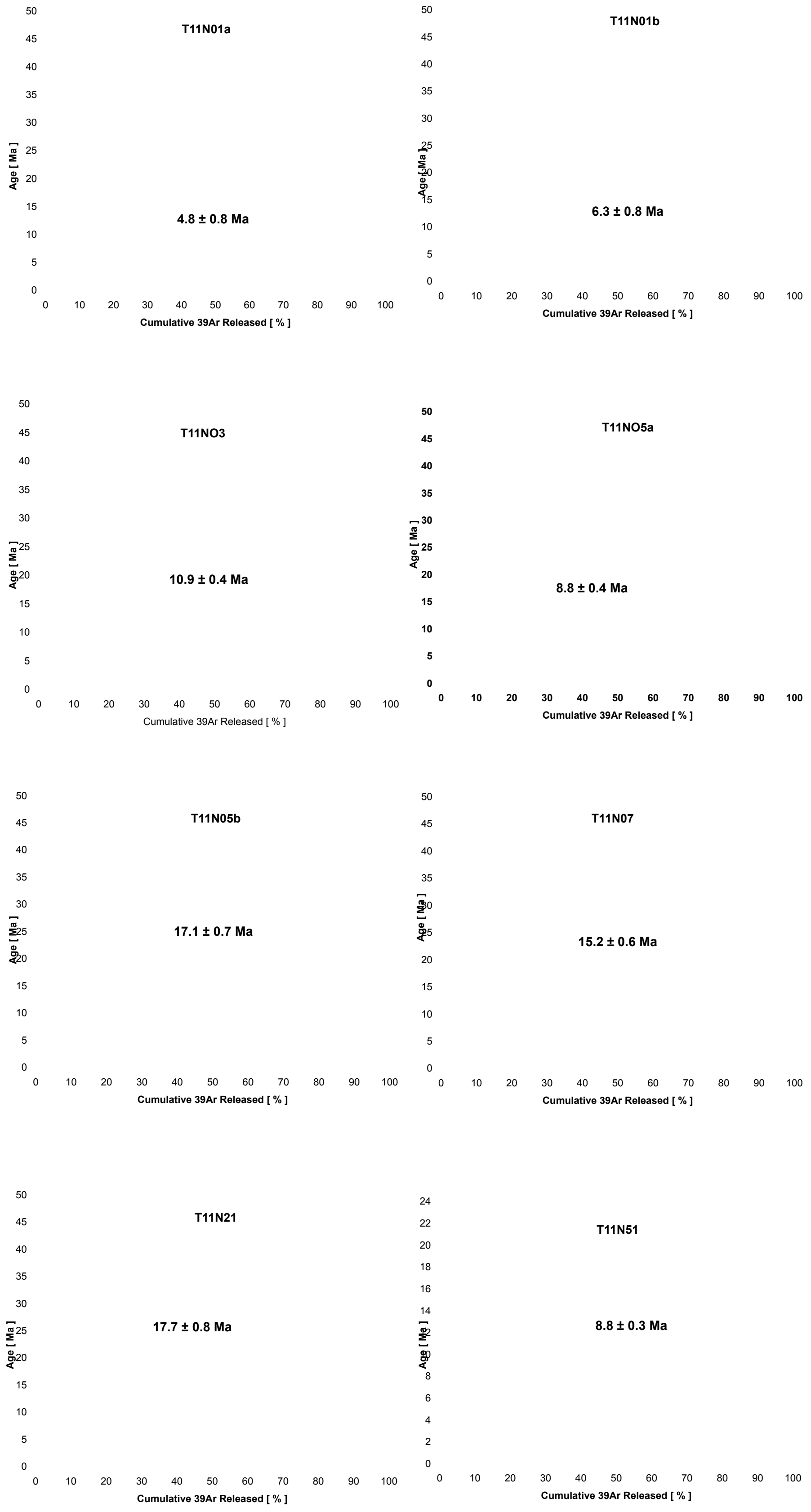
T11N01a
4.8 ± 0.8 Ma
T11N01b
6.3 ± 0.8 Ma
T11NO3
10.9 ± 0.4 Ma
T11NO5a
8.8 ± 0.4 Ma
T11N05b
17.1 ± 0.7 Ma
T11N07
15.2 ± 0.6 Ma
T11N21
17.7 ± 0.8 Ma
T11N51
8.8 ± 0.3 Ma
Age [Ma]
Cumulative 39Ar Released [%]

Fig. 10

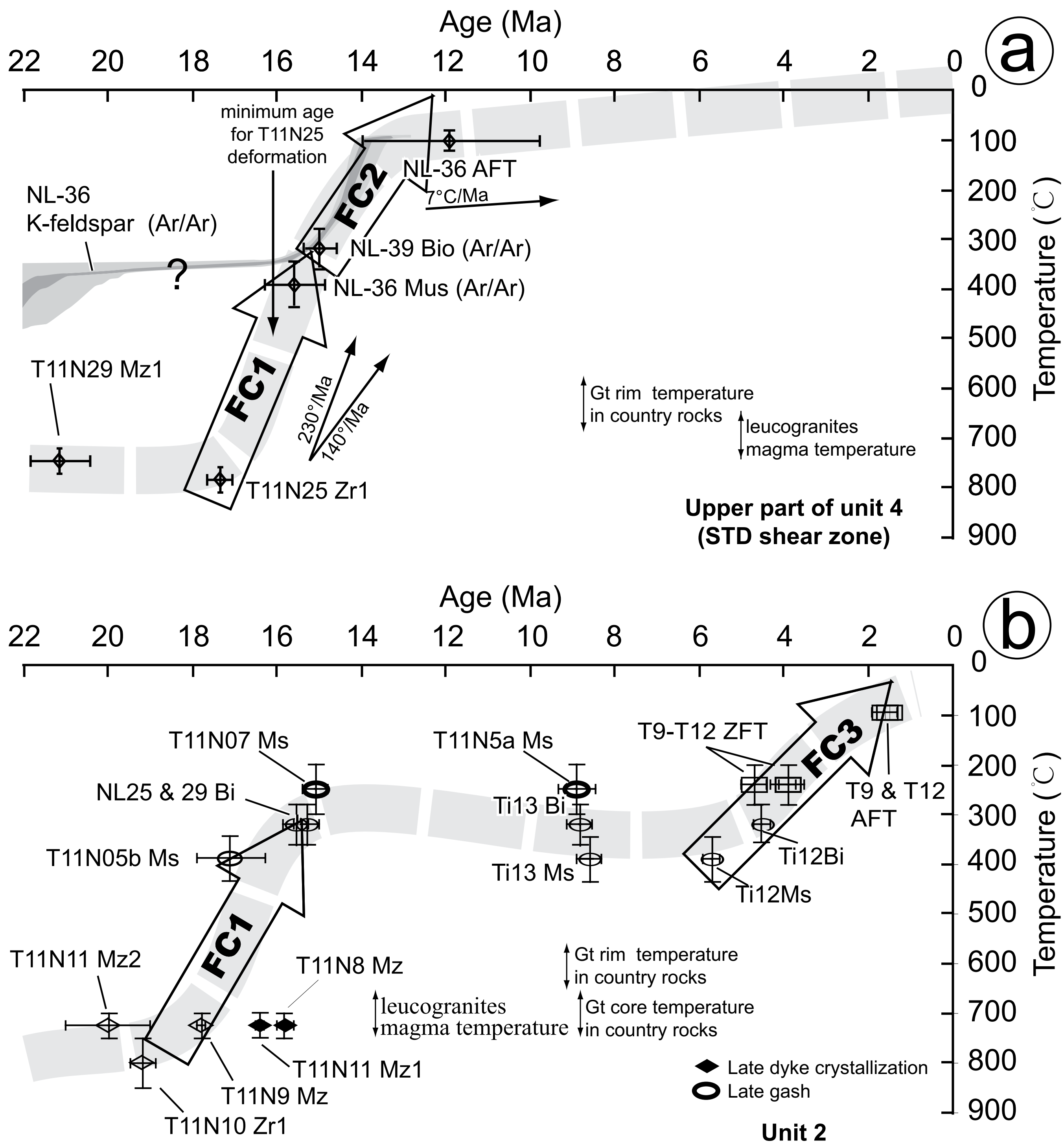
Age (Ma)
a
22 20 18 16 14 12 10 8 6 4 2 0
0 100 200 300 400 500 600 700 800 900
Temperature (˚C)
minimum age for T11N25 deformation
NL-36 K-feldspar (Ar/Ar)
?
NL-36 AFT
7°C/Ma
FC2
NL-39 Bio (Ar/Ar)
NL-36 Mus (Ar/Ar)
FC1
230°/Ma
140°/Ma
T11N29 Mz1
T11N25 Zr1
Gt rim temperature in country rocks
leucogranites magma temperature
Upper part of unit 4 (STD shear zone)
Age (Ma)
b
22 20 18 16 14 12 10 8 6 4 2 0
0 100 200 300 400 500 600 700 800 900
Temperature (˚C)
T11N07 Ms
NL25 & 29 Bi
T11N05b Ms
T11N5a Ms
Ti13 Bi
Ti13 Ms
T9-T12 ZFT
FC3
T9 & T12 AFT
Ti12Bi
Ti12Ms
FC1
T11N11 Mz2
T11N8 Mz
leucogranites magma temperature
Gt rim temperature in country rocks
Gt core temperature in country rocks
T11N11 Mz1
T11N9 Mz
T11N10 Zr1
Late dyke crystallization
Late gash
Unit 2

Fig. 11

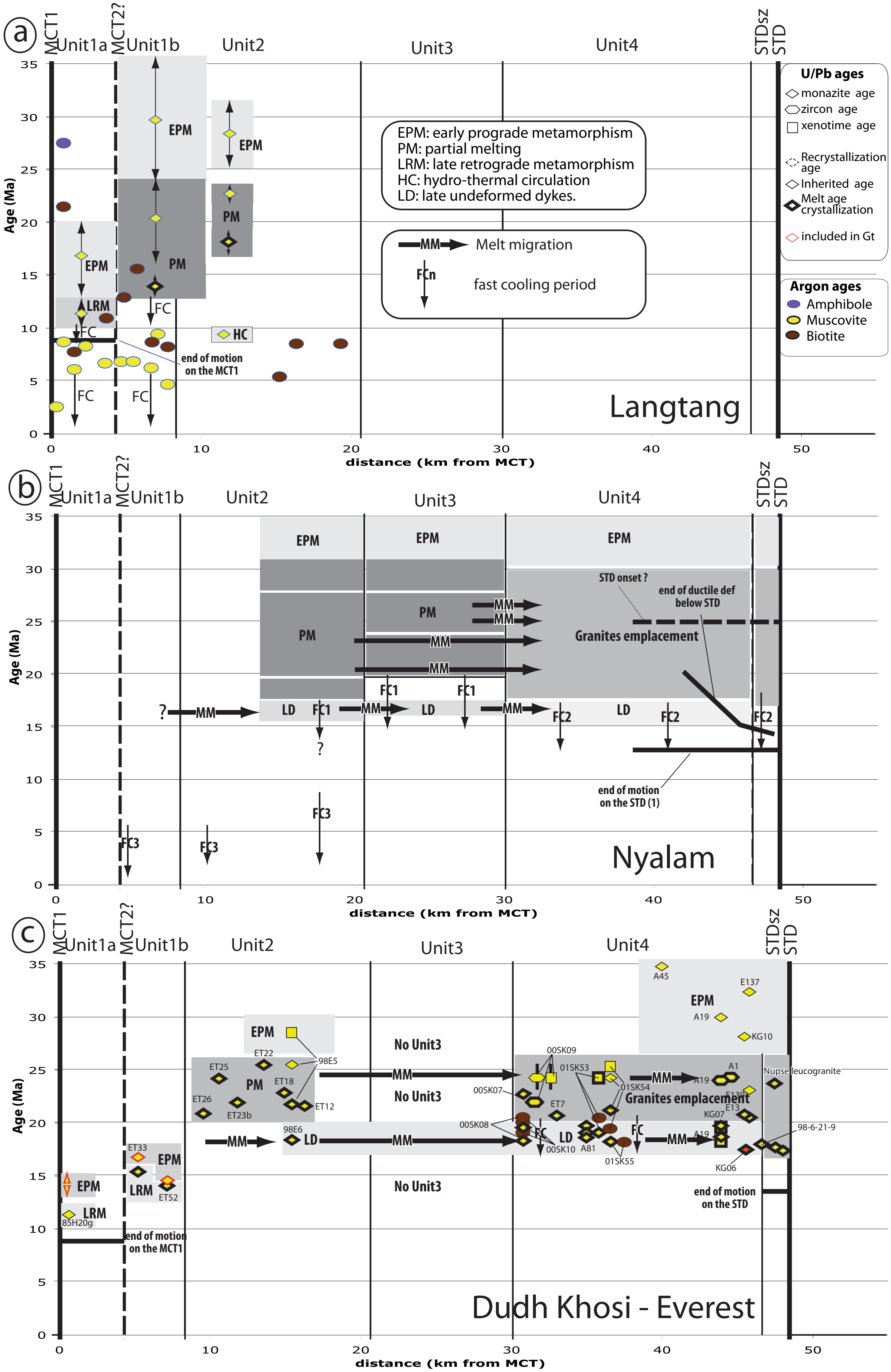

a
MCT1
MCT2?
Unit1a
Unit1b
Unit2
Unit3
Unit4
STDsz
STD
Age (Ma)
distance (km from MCT)
EPM: early prograde metamorphism
PM: partial melting
LRM: late retrograde metamorphism
HC: hydro-thermal circulation
LD: late undeformed dykes.
MM Melt migration
FCn fast cooling period
U/Pb ages
monazite age
zircon age
xenotime age
Recrystallization age
Inherited age
Melt age crystallization
included in Gt
Argon ages
Amphibole
Muscovite
Biotite
end of motion on the MCT1
Langtang
b
STD onset ?
end of ductile def below STD
Granites emplacement
end of motion on the STD (1)
Nyalam
c
No Unit3
Nupse leucogranite
end of motion on the STD
end of motion on the MCT1
Dudh Khosi - Everest

Fig. 12

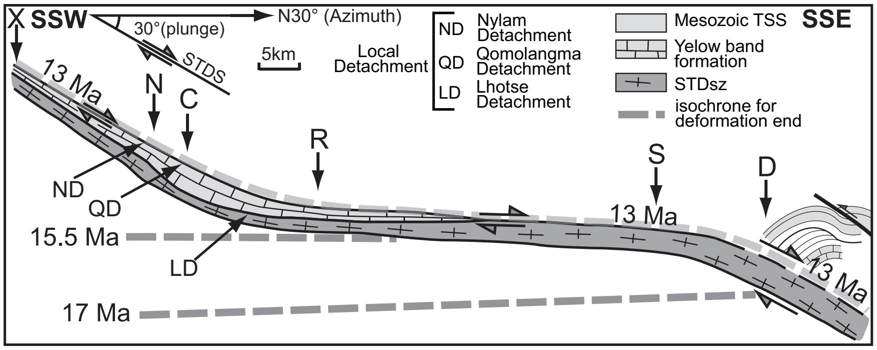

X
SSW
30°(plunge)
N30° (Azimuth)
STDS
5km
Local Detachment
ND Nylam Detachment
QD Qomolangma Detachment
LD Lhotse Detachment
Mesozoic TSS
Yelow band formation
STDsz
isochrone for deformation end
SSE
13 Ma
N
C
R
S
D
ND
QD
LD
15.5 Ma
13 Ma
13 Ma
17 Ma

Figure 13

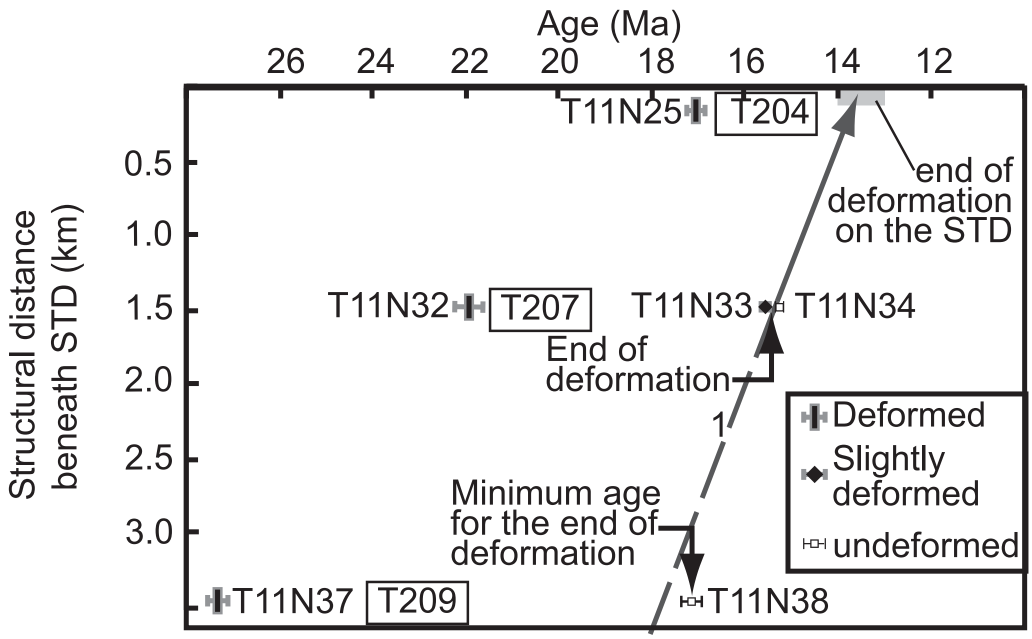
Age (Ma)
26
24
22
20
18
16
14
12
Structural distance beneath STD (km)
0.5
1.0
1.5
2.0
2.5
3.0
T11N25
T204
end of deformation on the STD
T11N32
T207
T11N33
T11N34
End of deformation
1
Minimum age for the end of deformation
T11N37
T209
T11N38
Deformed
Slightly deformed
undeformed

Figure 14

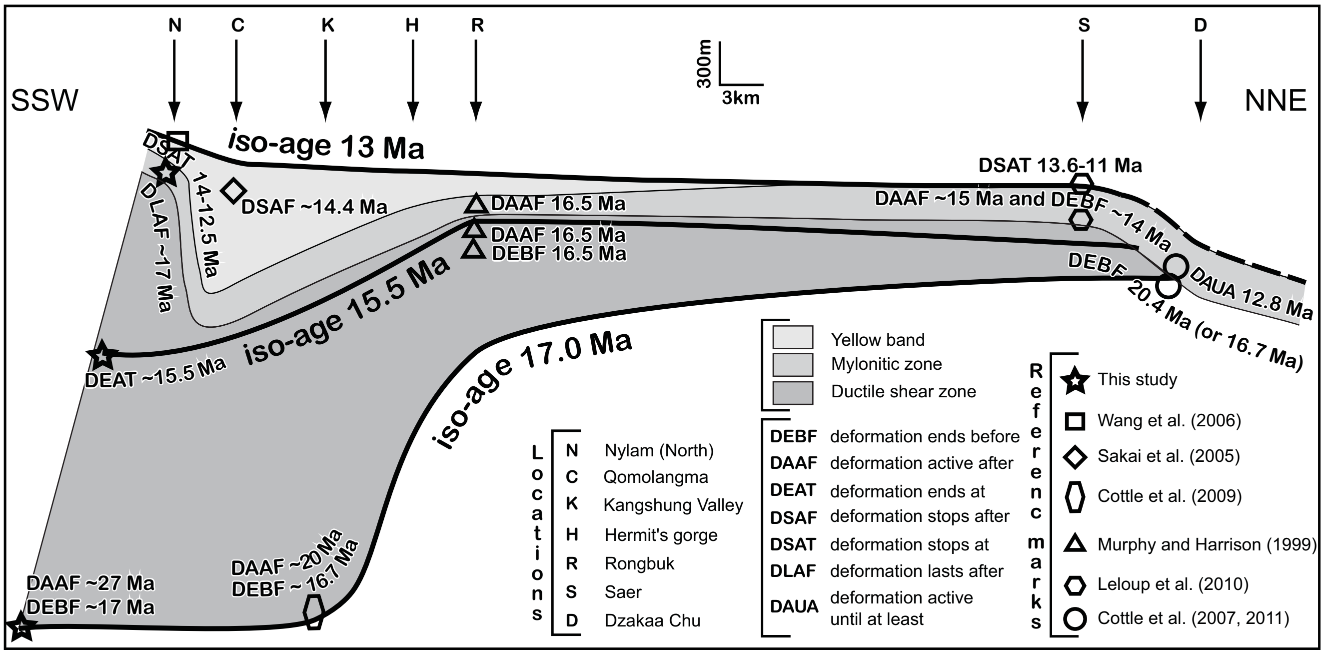
N
C
K
H
R
S
D
300m
3km
SSW
NNE
iso-age 13 Ma
DSAT
14-12.5 Ma
D LAF ~17 Ma
DSAF ~14.4 Ma
DAAF 16.5 Ma
DAAF 16.5 Ma
DEBF 16.5 Ma
DSAT 13.6-11 Ma
DAAF ~15 Ma and DEBF ~14 Ma
DEBF 20.4 Ma (or 16.7 Ma)
DAUA 12.8 Ma
iso-age 15.5 Ma
DEAT ~15.5 Ma
iso-age 17.0 Ma
DAAF ~27 Ma
DEBF ~17 Ma
DAAF ~20 Ma
DEBF ~ 16.7 Ma
Yellow band
Mylonitic zone
Ductile shear zone
Locations
N Nylam (North)
C Qomolangma
K Kangshung Valley
H Hermit's gorge
R Rongbuk
S Saer
D Dzakaa Chu
DEBF deformation ends before
DAAF deformation active after
DEAT deformation ends at
DSAF deformation stops after
DSAT deformation stops at
DLAF deformation lasts after
DAUA deformation active until at least
Reference marks
This study
Wang et al. (2006)
Sakai et al. (2005)
Cottle et al. (2009)
Murphy and Harrison (1999)
Leloup et al. (2010)
Cottle et al. (2007, 2011)

Figure 15

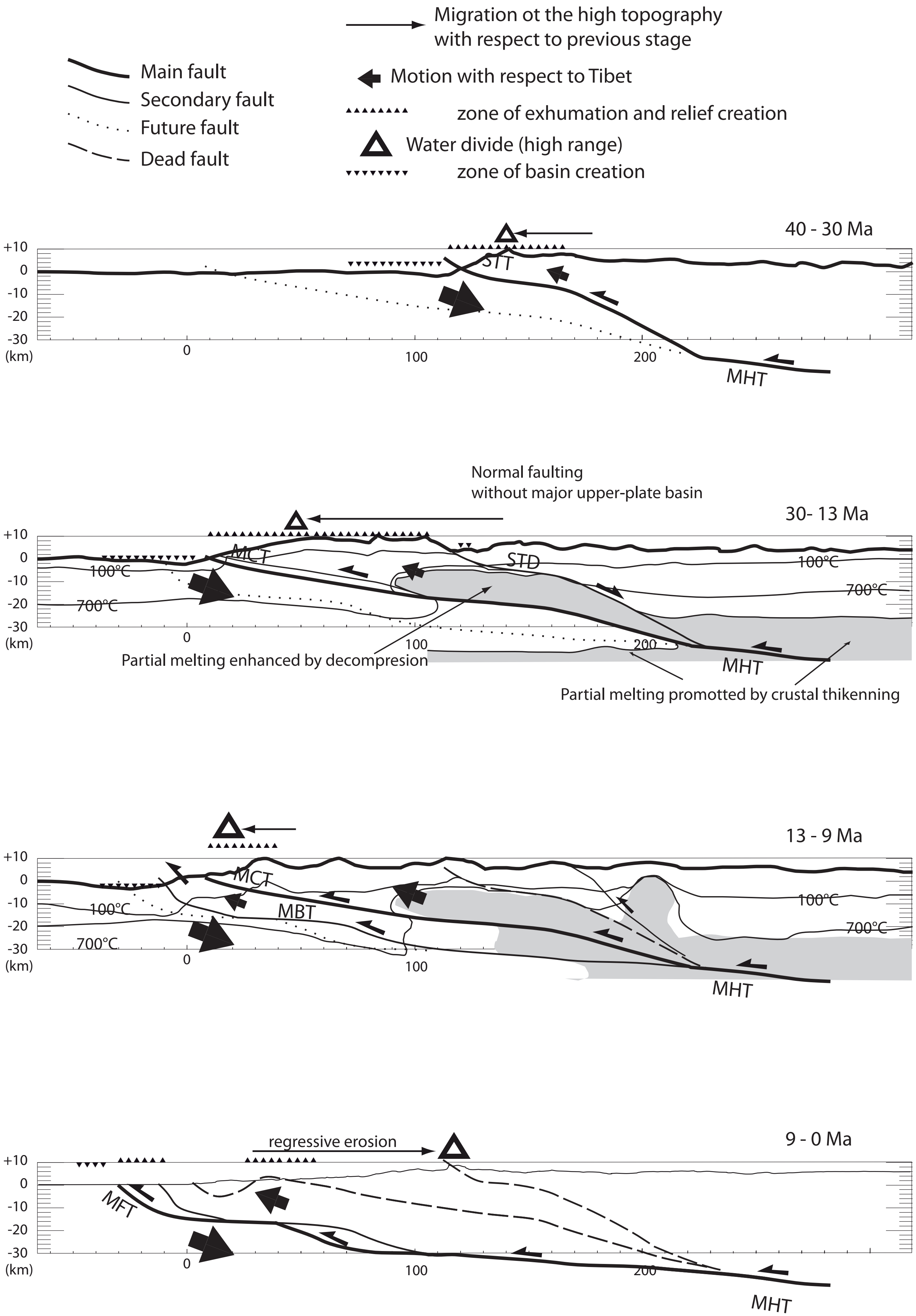
Migration ot the high topography
with respect to previous stage
Main fault
Secondary fault
Future fault
Dead fault
Motion with respect to Tibet
zone of exhumation and relief creation
Water divide (high range)
zone of basin creation
40 - 30 Ma
STT
MHT
Normal faulting
without major upper-plate basin
30- 13 Ma
MCT
STD
100°C
700°C
Partial melting enhanced by decompresion
Partial melting promotted by crustal thikenning
13 - 9 Ma
MBT
regressive erosion
9 - 0 Ma
MFT
+10
0
-10
-20
-30
(km)
100
200

Figure 16